NASA
Technical
Paper
3541

March 1996

Delay of Turbulent Boundary Layer Detachment by Mechanical Excitation: Application to Rearward-Facing Ramp

Daniel J. McKinzie, Jr.

National Aeronautics and
Space Administration

Page intentionally left blank

NASA Technical Paper 3541

1996

Delay of Turbulent Boundary Layer Detachment by Mechanical Excitation: Application to Rearward-Facing Ramp

Daniel J. McKinzie, Jr.
Lewis Research Center
Cleveland, Ohio

National Aeronautics and Space Administration

Office of Management

Scientific and Technical Information Program

Contents

Delay of Turbulent Boundary Layer Detachment by Mechanical Excitation: Application to Rearward-Facing Ramp

Daniel J. McKinzie, Jr.
National Aeronautics and Space Administration
Lewis Research Center
Cleveland, Ohio 44135

Summary

A vane oscillating about a fixed point at the inlet to a two-dimensional 20° rearward-facing ramp proved effective in delaying the detachment of a turbulent boundary layer. Flowfield, surface static pressure, and smoke-wire flow visualization measurements were made. Surface pressure coefficient distributions revealed that two different effects occurred with axial distance along the ramp surface. The surface pressure coefficient varied as a complex function of the vane oscillation frequency and its trailing edge displacement amplitude; that is, it varied as a function of the vane oscillation frequency throughout the entire range of frequencies covered during the test, but it varied over only a limited range of the trailing edge displacement amplitudes covered.

The complexity of these findings prompted a detailed investigation, the results of which revealed a combination of phenomena that explain qualitatively how the mechanically generated, periodic, sinusoidal perturbing signal produced by the oscillating vane reacts with the fluid flow to delay the detachment of a turbulent boundary layer experiencing transitory detachment.

Introduction

A rearward-facing ramp, like a rearward-facing step, is a common geometric element used in many flow devices. The rearward-facing ramp is particularly important because it is the fundamental element of diffuser designs. Diffusers, in turn, are components of turbopropulsion systems, wind tunnels, test facilities, etc. They are a relatively simple fluid-mechanical device, the basic characteristics of which are still not clearly understood (refs. 1 through 3). Diffusers frequently operate to provide maximum pressure recovery, shown experimentally to occur at conditions approaching transitory detachment (50 percent instantaneous backflow, ref. 4). Operating at conditions near transitory detachment becomes particularly critical with the occurrence of unsteady inlet flow conditions that may produce complete or partial detachment of turbulent boundary layers, thus impacting the design of the flow devices incorporating them and, in turn, their economics.

In recent years studies using active control techniques indicated that introducing small perturbing signals into laminar or turbulent unstable boundary layers experiencing transitory detachment delays detachment. Though the cause and effect demonstration of these techniques is and has been of current interest, little qualitative detail of the phenomena has been presented. Examples of pertinent studies include those of Neuburger and Wygnanski (ref. 5), Katz, Nishri, and Wygnanski, (ref 6), and McKinzie (ref. 7). The first two are not specifically studies of a rearward-facing ramp or diffuser flow, but the third is a study of a rearward-facing ramp. All three, however, are studies of a shear layer experiencing detachment. The purpose of each study was to delay detachment by introducing into the shear layer periodic, two-dimensional perturbing signals. There are principal differences in the studies of Neuburger and Wygnanski (ref. 5) and Katz, Nishri, and Wygnanski (ref. 6) and that of McKinzie (ref. 7). Reference 5 considered flow passing over an airfoil at a large angle of attack, and reference 6 studied turbulent flow passing over a divergent plate connected to an axially oriented splitter plate located on the centerline of a mixing layer facility. In each case, the delay in detachment was effected by a small ribbon or flap that was positioned upstream of the point of detachment, fastened to the surface along its upstream edge, and oscillated. Reference 7 is a progress report of research initiated to study the oscillating vane's effect on the delay in detachment of turbulent boundary layer flow experiencing the early stages of detachment while passing over a 20° rearward-facing ramp. This research is part of an experimental and numerical program at the NASA Lewis Research Center to study the effect of controlled perturbing signals on the natural flow instabilities of several types of turbulent shear layers with the objective of controlling them.

The purpose of the airfoil study of Neuburger and Wygnanski (ref. 5) was to prove the hypothesis that the detachment of a bounded shear layer may be delayed to a higher angle of attack by increasing the characteristic width or scale of the eddies generated by the Kelvin Helmholtz instability of a free, separated shear layer. This change in the scale of the eddies, then, is the mechanism by which entrained fluid comes from the limited reservoir bounded by the detached shear layer and the solid surface of the airfoil causing the pressure

to decrease and the detached shear layer to bend toward the surface in order to provide the required balance between the curvature of the flow and the pressure gradient in the direction perpendicular to the streamlines. The use of excitation was intended to enhance the production of very large-scale eddies. Flow visualization, surface pressure measurements, and wake surveys to determine the drag coefficients were made for two airfoils in this investigation. The study showed that the delay in detachment and the enhancement of the maximum lift coefficient Cl_{max} for both airfoils depended on the geometry of the airfoil, the Reynolds number, the location of the vibrating ribbon used to excite the Kelvin Helmholtz instabilities, and the frequency and amplitude of the imposed oscillation. Proof of the hypothesis was inferred by the pressure coefficient and flow visualization data presented.

Katz, Nishri, and Wygnanski (ref. 6) proposed the same mechanism as that of Neuburger and Wygnanski (ref. 5). The study was undertaken to further test the concept of this mechanism and the feasibility of using it to delay detachment of a bounded shear layer. A flat plate was positioned at a divergent angle of 18° to a splitter plate that was axially located in a mixing layer facility. The flat plate intersected the splitter plate a small distance upstream of the splitter plate trailing end. Attached to this overhanging segment was a small flap, which was hinged to the end of the splitter plate in a manner such that it could be oscillated. The displacement amplitude of the flap was small, on the order of ±1 mm, and produced a maximum divergence angle of approximately 6°. When the flap was not in motion, the local static pressure gradient required to maintain flow attachment was not attained and the boundary layer detached. The detached, unexcited shear layer flow was shown to be the same as that of a classical mixing layer. As such, it was reasoned, it should be possible to excite the shear layer as free mixing layers are excited. To test this hypothesis, the flap located at the end of the splitter plate was oscillated at frequencies corresponding to Strouhal numbers (based on momentum thickness) that were less than 0.01 and flap displacement amplitudes that produced local turbulence intensities of 0.25 percent. These conditions produced reattachment of the flow downstream of the flap, which effectively resulted in a delay in detachment with values of the maximum pressure coefficient approaching increases of 100 percent of the unexcited case. The study concluded that the introduction of harmonic, two-dimensional oscillations results in the delay in flow detachment and changes the proportions between the wake and wall function; it does not, however, alter their universal forms.

In summary, Neuberger and Wygnanski (ref. 5) and Katz, Nishri, and Wygnanski (ref. 6) studied phenomena produced by excitating the instability waves of a free shear layer with periodic signals that caused it to thicken, entrain fluid, effect the static pressure, and finally reattach downstream of the detached region. This produced, in effect, a delay in detachment. In both studies one is left with the impression that the boundary layer detached and reattached downstream to form what might be described as a bubblelike flow region between. This description is reminiscent of the bubble that forms when a laminar boundary layer separates in an adverse pressure gradient and reattaches as a turbulent boundary layer characteristic of flow passing over a thin airfoil operating at a moderate lift coefficient.

In the more recent study by McKinzie (ref. 7), a curved vane oscillating about a fixed point at the inlet to a two-dimensional 20° ramp was shown to be effective in delaying the detachment of a turbulent boundary layer. In reference 7 a limited amount of data obtained during the initial phase of this study was reported. The ramp was attached to an upstream flat plate positioned within the NASA Lewis 20- by 30-Inch Low-Speed Wind Tunnel. Based on preliminary data and a review of the literature, a qualitative explanation of the delay in detachment was presented in reference 7. The present study provides the flow-field structural detail and smoke-wire flow visualization data that more completely describe the delay in detachment.

In the McKinzie study (ref. 7), the mechanism producing a delay in detachment is believed to be different from that of references 5 and 6; that is, the periodic perturbing signal produced by the action of an oscillating vane is introduced into the inner layer of a turbulent boundary layer experiencing transitory detachment. Here the boundary layer does not detach and then reattach some distance downstream with a bubblelike region between. Rather, the action of the vane effects an increase in the growth of inviscid flow instabilities (studied by Michalke, ref. 8) downstream, which result in the increased production of turbulence in the inner wall region, with a consequent shift in the location of the boundary layer detachment further downstream, thereby delaying the boundary layer detachment.

This report has two objectives: first, to present experimental measurements, including flow visualization data, of the interaction of an oscillating vane located at the entrance to a rearward-facing 20° ramp with a boundary layer experiencing the early stages of detachment; second, to explain qualitatively how the mechanically generated periodic perturbing signal reacts with the fluid flow to ultimately effect a delay in the detachment of the turbulent boundary layer experiencing transitory detachment.

Symbols

a	factor of order of 1.0, eq. (A7)
B_1	constant, eq. (7)
C	constant, measure of change in dimensionless velocity across viscous sublayer

Cl_{max}	maximum lift coefficient $\mathcal{L}/[1\ 2(\rho U_\infty^2)]$
C_{ph}	phase velocity
E	corona anemometer output voltage (fig. 9)
e	small extra rate of strain
F	F-factor in eq. (A2), empirical extension of f^*
f	frequency
f^*	factor in eq. (A7), $1 + \{a[e/(\partial U)/(\partial y)]\}$
H	shape factor, δ^*/θ
h	peak-to-peak displacement measured at trailing edge of oscillating vane
Δh_{offset}	gap distance between ramp surface and lower limit of travel of vane trailing edge
k	Karmon's constant
k_e	effective surface roughness
L	surface distance from vane trailing edge
$\mathcal{L}$	lift
P	static pressure
q	dynamic pressure, $1/2(\rho U_\infty^2)$
R	radius of curvature
Re	Reynolds number
Re_θ	Reynolds number based on momentum thickness, $(\rho U_\infty \theta)/\mu$
r	radius
S	surface distance referenced to point 12.5 cm upstream of ramp inlet where local surface static pressure P_L is constant and equal to P_1 along flat plate; length scale
S_1	surface distance measured from tangent point at intersection of model upstream flat plate and cylindrical transition section leading to ramp
St_θ	Strouhal number based on momentum thickness, $f\theta/U$
T	time
U, V, W	mean velocity components in x-, y-, z-directions, respectively
U_e	typical velocity in direction of flow
U_1	ramp free-stream inlet velocity at $S = 0$
$(U_\infty)_L$	free-stream velocity at edge of boundary layer
u_τ	friction velocity, ky $(\partial U/\partial y)$
u^+, y^+	wall layer nomenclature in inner wall coordinates
u, v, w	fluctuating velocity components in x-, y-, z-directions, respectively
u', v', w'	fluctuating velocity components in x-, y-, z-directions, respectively
$\tilde{u}, \tilde{v}, \tilde{w}$	total velocity components in x-, y-, z-directions, respectively
$\overline{uv}$	Reynolds shearing stress
$W(y/\delta)$	wake function
x	axial coordinate axis (fig. 1)
y	vertical coordinate axis perpendicular to model surface (fig. 1)
y_m	model vertical coordinate axis perpendicular to wind tunnel floor (fig. 1)
z	spanwise coordinate axis with origin located on vertical plane passing through axial centerline of model and tunnel
Excited condition	oscillating vane on model and oscillating

Nonexcited condition	oscillating vane not on model
α	factor of order 10, eq. (A8)
$\alpha_r\Delta$	amplification rate wave number based on one-half of vorticity thickness, Δ
$\alpha_r\theta$	amplification rate wave number based on momentum thickness, θ
Δ	one-half the vorticity thickness
δ	boundary layer thickness
δ_l	viscous sublayer thickness (fig. 27)
δ_w	vorticity thickness
δ^*	displacement thickness
ε	turbulent kinetic energy dissipation rate
θ	momentum thickness
λ	wavelength
λ_x	wavelength of maximum unstable disturbance
μ	viscosity
ν	kinematic viscosity
Π	wake parameter
ρ	density
ϕ	phase angle difference; lag angle
ψ	stream function
$\Omega_x,\Omega_y,\Omega_z$	rectilinear coordinates of mean vorticity
$\omega_x,\omega_y,\omega_z$	rectilinear coordinates of mean vorticity

Subscripts:

L	local
max	maximum
P	hot-wire anemometer probe
r	rough wall
s	smooth wall
T	tangent
v	vane
∞	free stream; infinity
0	reference or initial value
1	ramp inlet external stream condition at $S = 0$

Superscripts:

+	inner wall coordinate
~	total quantity

Apparatus and Instrumentation

Figure 1 presents a schematic diagram of the 20° rearward-facing ramp attached to an upstream flat plate. The model is shown in the NASA Lewis 20- by 30-Inch Low-Speed Wind Tunnel (ref. 9). The wind tunnel test section is 76 cm wide by 50.8 cm high by 203 cm long. The tunnel is an open-loop design and has an inlet-to-test section contraction ratio of 16 to 1. At the inlet, the flow passes through five turbulence-conditioning screens, through the test section, and is exhausted to ambient conditions by an axial flow fan.

The model was fabricated from hardwood by using a lamination technique and has a smooth, nonlacquered surface. The design of the upstream flat plate included compensation for boundary layer growth assuming a ramp inlet velocity of 6.6 m/sec; thus, a zero axial pressure gradient was produced at the inlet to the ramp. The model x and y_m coordinates are presented in table I. A 3.8-cm-radius-of-curvature cylindrical transition section joined the flat plate to the 20° rearward-facing ramp. The model spanned the entire width of the tunnel; thus, the sidewall boundary layers affected the experimental results. It must be pointed out that the ratio of the model width to height was 10 and the sidewall boundary layer thicknesses at the inlet to the ramp were estimated to be approximately 3.5 cm; therefore, it is believed that the effects of the sidewall boundary layers were confined to this limited region on either side of the ramp. The surface of the cylindrical transition section was designed to match the radius of curvature of a vane having a 2.54-cm chord, a 0.025-cm thickness, and a 73.34-cm length. The vane was positioned in the spanwise (z-) direction (fig.1) at the crest of the ramp. It was attached to the surface along its upstream edge with tape

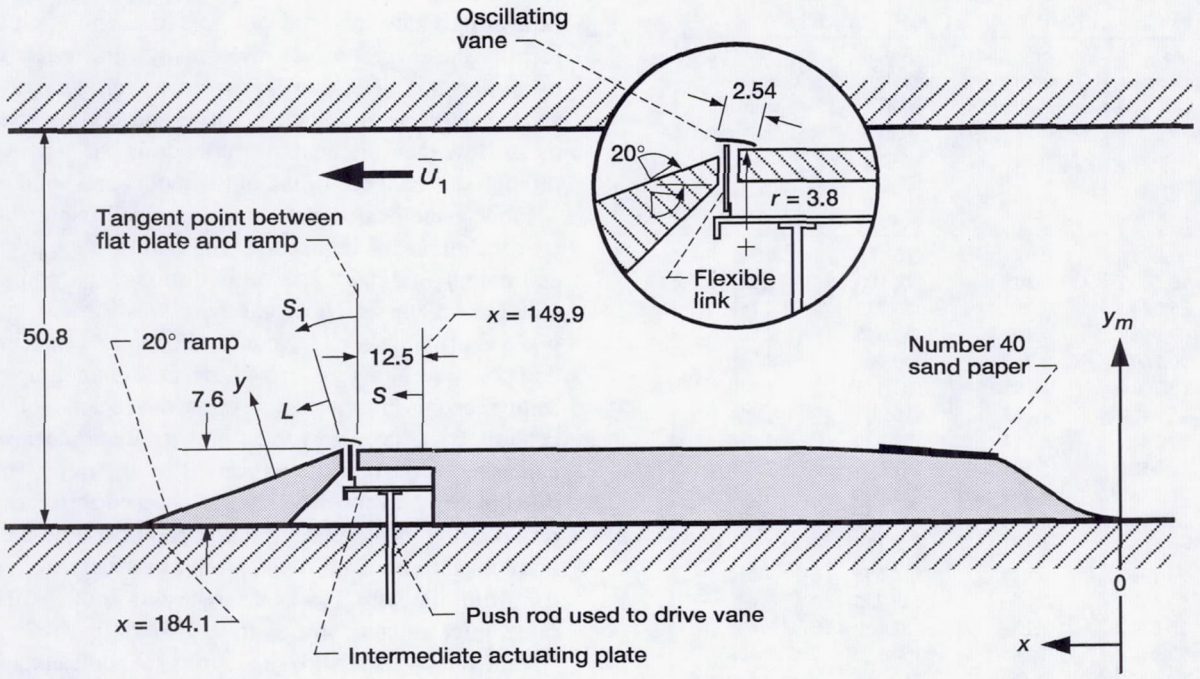

Figure 1.—Twenty-degree rearward-facing ramp model in 20- by 30-Inch Low-Speed Wind Tunnel (z-component axis perpendicular to plane of sketch). All dimensions are in centimeters.

and was sinusoidally oscillated throughout the study over a frequency range from 15 to 33 Hz and peak-to-peak displacement heights h from 0.089 to 0.536 cm. Several axial surface coordinates are presented in figure 1, including S, S_1, and L. The coordinate S was referenced to 12.5 cm upstream of the tangent point, at the inlet to the ramp; S_1 was referenced to the inlet tangent point; and L was referenced to the trailing edge of the oscillating vane when it was in contact with the model surface ($h = 0$). The upstream surface distance between the leading edge of the vane and the tangent point where the flat plate intersects the cylindrical transition section at the inlet to the ramp was S_1 of –0.83 cm. The location of the vane on the model surface was established from preliminary tests that qualified the vane as an effective control device in the present study.

The vane actuator mechanism, located in a hollowed out portion of the model, was driven by an oscillator and a precision vibrator located beneath the tunnel. A miniature accelerometer, positioned on the driver push-rod mechanism, was used to measure the displacement of the vane. The displacement output signal from the accelerometer signal conditioner was measured with a frequency counter and an oscilloscope to determine the vane trailing edge frequency and displacement waveform, which, for all test conditions, was a smooth, sinusoidal waveform. Three, small, flexible links were the final members in the drive train that transferred the periodic forcing function from the driver to the oscillating vane. These flexible links passed through small holes in the model surface well under the oscillating vane. The in-phase operation of the vane, its oscillation frequency, and displacement were cross-checked optically using strobe equipment.

To insure a turbulent boundary layer at the inlet to the rearward-facing ramp, a 23-cm-wide by 76-cm-long strip of number 40 sandpaper was positioned well upstream on the flat plate (shown schematically in fig. 1). The Reynolds number based on momentum thickness measured at the crest of the ramp was 1200 for a typical case in which the inlet velocity to the ramp was 6.6 m/sec.

The ramp/flat plate model was instrumented with 17 static pressure taps 5.08 cm off its centerline. These taps were distributed axially over the inlet and ramp as indicated by the sketch presented in figure 2(a). One spanwise row of five static pressure taps was located at an S of 8.50 cm. Two of these taps were located 2.54 cm from the opposite sidewalls of the wind tunnel, two were located 20.32 cm from opposite sidewalls, and one was located on the model centerline. The static pressures were determined using a computer program incorporating calibration data for a single 0- to 689.5-dynes/cm^2 differential pressure transducer. Each static pressure port on the model was sequentially read by manually actuating a switch that stepped a rotary valve from one port to the next.

Flow-field and turbulent boundary layer measurements were made using single- and cross-hot-wire anemometry. The single-wire anemometer was used in conjunction with an FFT analyzer, constant-temperature anemometry, and computer-aided data acquisition and data reduction instrumentation to obtain the probability density function, the power spectral density, and the turbulence intensity data. In addition, two-point, single-

TABLE I.—TWENTY-DEGREE REARWARD-FACING RAMP MODEL COORDINATES

Axial coordinate, x, cm	Model vertical coordinate perpendicular to wind tunnel floor, y_m, cm	Axial coordinate, x, cm	Model vertical coordinate perpendicular to wind tunnel floor, y_m, cm
0.000	0.074	70.485	8.301
2.540	.305	78.100	8.235
5.080	.752	85.725	8.169
7.620	1.412	93.345	8.103
10.160	2.250	100.965	8.036
12.700	3.195	108.585	7.970
15.240	4.163	116.205	7.904
17.780	5.082	123.825	7.838
19.050	5.507	131.445	7.772
20.320	5.893	139.065	7.706
21.590	6.248	141.605	7.686
22.860	6.558	144.145	7.663
24.130	6.828	146.685	7.640
25.400	7.056	149.225	7.630
26.670	7.234	151.689	7.625
27.940	7.386	154.711	7.620
28.575	7.437	157.251	7.620
29.210	7.488	159.791	7.620
29.688	7.516	162.331	7.620
29.845	7.526	162.585	7.612
30.480	7.564	162.839	7.587
33.020	7.716	163.093	7.544
35.560	7.869	163.347	7.483
38.100	8.021	163.601	7.402
40.640	8.174	163.634	7.391
43.180	8.326	164.871	6.939
43.815	8.364	167.411	6.015
44.450	8.410	169.954	5.090
46.990	8.471	172.491	4.166
48.260	8.471	173.031	3.241
50.880	8.461	177.571	2.316
53.340	8.448	180.111	1.392
55.880	8.428	182.651	0.467
58.420	8.405	183.307	0.231
60.960	8.382	183.561	0.147
62.865	8.367	183.815	0.084
		184.069	0.038

hot-wire anemometry was used to obtain phase angle difference and the coherence data. The cross-hot-wire anemometer was used in conjunction with a correlator ac voltmeter, true rms voltmeters, and computer-aided data acquisition and data reduction instrumentation to obtain Reynolds stress data.

A spacial version of a high-voltage corona anemometer (refs. 10 and 11) was used in the transitory detached flows studied here to measure the probability density function from which flow reversal rates were determined. A corona anemometer is a device that can measure the speed and direction of a gas by the displacement of an ion beam produced by a corona discharge. It is bidirectional and responds dynamically; therefore, it is especially suited to measure unsteady reversing flow. Data from this probe are presented as contours of averaged flow reversal per unit time and can be used to identify the several stages of unsteady detachment discussed by Simpson, Chew, and Shivaprasad (ref. 4). The hot-wire anemometer mean velocity profile and corona anemometer mean flow measurements were made in the y-plane passing through the axial centerline of the model and wind tunnel.

Flow visualization data were obtained using the smoke-wire technique in conjunction with portrait-type photographic equipment and high-speed motion picture equipment. A 0.002-cm-diameter Nichrome wire was located in the x, y-plane approximately 11.5 cm off the model centerline at several positions along its surface. Because photographic visualization records instantaneous events, this location off the model centerline was necessary to eliminate the remote possibility of capturing erroneous effects caused by the three, small, flexible links in the vane drive train, discussed above. Smoke was produced by using model train oil and operating the wire at a nominal current of 1.5 A. To produce a steady, smooth smoke trail from the wire, it was necessary to limit the free-stream ramp inlet velocity to 2.6 m/sec. Slightly above this free-stream velocity, the wire shed turbulent eddies that interfered with the effectiveness of the smoke. Thus, for the flow visualization part of this study, the free-stream inlet velocity to the ramp was 2.6 m/sec, whereas for the instrumented flow-field part, the inlet velocity was typically 6.6 m/sec. The corresponding Reynolds numbers based on momentum thickness and the shape factors measured at the inlet for the 6.6-m/sec case were 1200 and 1.38, respectively; for the 2.6-m/sec case they were 576 and 2.01, respectively. These data indicate that the flow entering the ramp for the 6.6- and 2.6-m/sec cases was turbulent and transitional, respectively. The question naturally arises as to whether the phenomena photographically observed and the phenomena deduced from hot-wire measurements in this study are similar. The following comments are offered in reply. Admittedly, there are differences between transitional and turbulent boundary layer flows, particularly in the case of attached flow passing over a flat plate; however, in the present study a condition imposed on the experiment required that the flow entering the model ramp experience the early stages of detachment from the ramp surface. The 20° angle of the rearward-facing ramp used in the experiment produced this condition. This requirement was imposed to permit the evaluation of an oscillating vane as an effective device for delaying the detachment of a turbulent boundary layer. As either the transitional or the turbulent flow approaches the entrance to a 20° rearward-facing ramp, the velocity profile develops an inflection point as the flow lifts up off the surface during the early stages of detachment. This velocity profile in an inviscid fluid is unstable to small disturbances. This condition exists for either the transitional or the turbulent boundary layer at the entrance to the 20° rearward-facing ramp. It is into these unstable velocity profiles that the two-dimensional spanwise disturbances produced by the os-

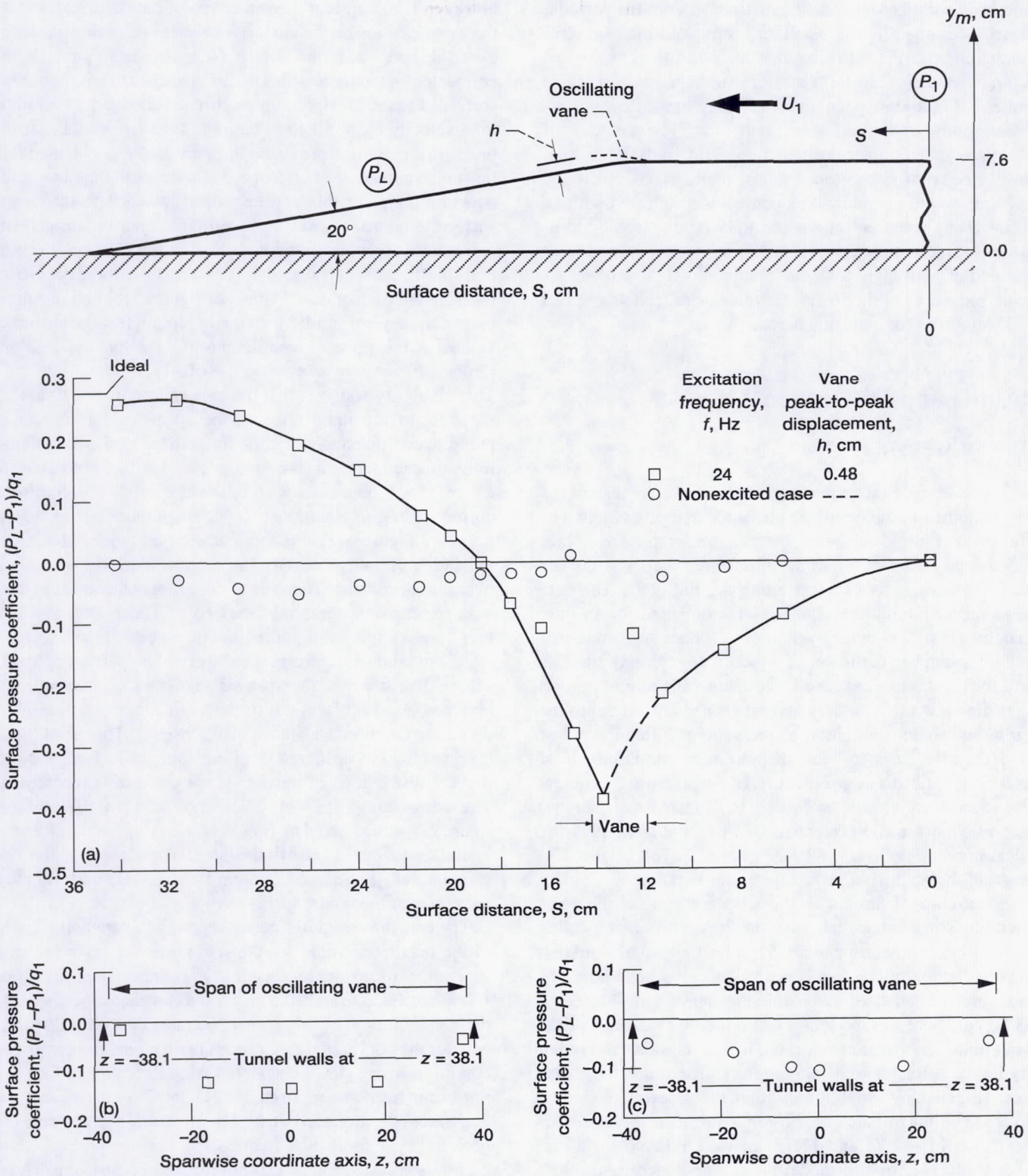

Figure 2.—Surface pressure coefficient distribution on model. (a) Axial distribution for excited and nonexcited cases; inlet velocity, U_1, 2.6 m/sec. (b) Spanwise distribution for excited case at surface distance S of 8.5 cm; inlet velocity, U_1, 2.6 m/sec; excitation frequency, f, 24 Hz; vane peak-to-peak displacement, h, 0.48 cm. (c) Spanwise distribution for nonexcited case at surface distance S of 8.5 cm; inlet velocity, U_1, 10.45 m/sec.

cillating vane are introduced. Therefore, the present study is concerned with the dynamic interaction between the periodic disturbances shed by the oscillating vane and their inviscid interaction with the inflectional velocity profiles of the detaching boundary layers. Therefore, in this sense there is similarity in the flow phenomena revealed in the flow visualization study conducted at a ramp inlet flow velocity of 2.6 m/sec and the instrumented flow-field study at an inlet flow velocity of 6.6 m/sec. Portrait photographs, 10.16 by 12.7 cm, were obtained with a camera instrumented with an electronically synchronized shutter/strobe light source. Sixteen-millimeter motion picture data at 400 frames per second were obtained using a high-powered, continuous light source. Selected sequences of motion picture data were rephotographed on 35-mm film for inclusion herein.

Results and Discussion

Pressure Recovery

Typical surface pressure coefficient data, referenced to the inlet condition to the ramp, are presented in figures 2 and 3 as a function of surface distance S, which is referenced to a point 12.5 cm upstream of the ramp inlet where the local surface static pressure P_L is constant along the flat plate. The data presented in figures 2(a) and (b) were obtained for an inlet velocity U_1 of 2.6 m/sec, which corresponds to a nominal Reynolds number per meter of 1.3×10^5. Figure 2(a) presents data for the nonexcited case (oscillating vane not on model) indicating that the boundary layer detached at the inlet to the ramp. Sinusoidal oscillation of the vane at a frequency f of 24 Hz and a peak-to-peak displacement amplitude h of 0.48 cm produced a large reduction of the pressure coefficient at the vane location, and an equally large increase at the ramp exit, to almost a 100-percent recovery of the static pressure (ideal pressure recovery, $(P_L - P_1)/q_1 = 0.278$). Figure 2(b) presents the spanwise surface pressure coefficient data obtained at an S of 8.5 cm in the y,z-plane and for the same operating condition as that of figure 2(a). This axial location was 3.2 cm upstream from the vane leading edge. Note that the distribution of the data is not uniform in magnitude. The static pressure taps, used to obtain the data at z of –35.56 and 35.56 cm, were located 2.54 cm from either sidewall of the wind tunnel and were also located within the sidewall boundary layers estimated to be 3.5 cm thick. Therefore, these data were affected by conditions within the sidewall boundary layers. The magnitudes of the remaining data obtained between a z of –17.78 and 17.78 cm were relatively uniform over the center of the model span. The specific spanwise distance from the wind tunnel sidewalls affected by the flow conditions within the sidewall boundary layers is unknown because sufficient additional data were not obtained. Thus, the significance of the nonuniformity in the magnitudes of the data is not known. Perhaps one way to address this result, however, is to consider the same type of data distribution (at the same location on the model) for a case where flow passing over the ramp does not detach from its surface, that is, a completely natural flow that is not detached from the ramp surface. Figure 2(c) presents such data obtained at a ramp inlet velocity U_1 of 10.45 m/sec. The spanwise surface static pressure distribution presented in figure 2(c) was obtained for this nonexcited case at an S of 8.5 cm. Because the flow field over the ramp for this case remained attached to the ramp surface, the surface pressure coefficient distribution shown represents a completely natural distribution (without excitation) for the present test model. A comparison of the spanwise pressure coefficient distributions of figures 2(b) and (c) indicates that they are similar with the exception that the absolute values of the pressure coefficients for the excited case in figure 2(b) are larger between a z of –17.76 and 17.76 cm. This similarity suggests that the sidewall boundary layers at the inlet to the ramp affected the spanwise surface static pressure coefficient distribution for both the excited and naturally attached cases in the same way. The data presented in figure 3 were obtained for an inlet velocity U_1 of 6.6 m/sec, corresponding to a nominal Reynolds number per meter of 3.5×10^5. Figure 3(a) presents data for the nonexcited case indicating that the boundary layer detachment did not occur over the entire ramp. This lack of complete detachment agrees with experimental criteria discussed by Chien (ref. 12) and therefore is expected. Exciting the flow at 29 Hz and an h of 0.536 cm produced a pressure recovery of 88 percent of ideal. Figure 3(b) presents the spanwise pressure coefficient data obtained at an S of 8.5 cm in the y,z-plane and at the same operating conditions as those of figure 3(a). This axial location was 3.2 cm upstream from the vane leading edge. Note that the distribution of the data is not uniform in magnitude. The data obtained at z's of –35.56 and 35.56 cm, like those in figure 2(b), are affected by flow conditions within the sidewall boundary layers of the wind tunnel. The data obtained between a z of –17.78 and 17.78 cm are relatively uniform over the center of the model span.

The data presented in figure 4 represent a parametric study of the maximum values of the static pressure recovery as a function of the excitation frequency f for ramp inlet velocities U_1 of 2.6, 4.6, 6.6, and 10.5 m/sec at a constant vane displacement amplitude h of 0.318 cm. The intercepts with the ordinate for the nonexcited case (vane not on model) represent the condition where flow detachment from the ramp surface did not occur over the entire ramp. For the 2.6-m/sec case, the peak recovery occurred at 24 Hz; note the rolloff from the peak at larger oscillation frequencies. For the 4.6-, 6.6-, and 10.5-m/sec cases, a peak was not reached because the driver-vibrator used in the experiment was not capable of maintaining the displacement amplitude at higher frequencies. However, these results show that the optimum excitation frequency increases in some proportional relationship with increases in

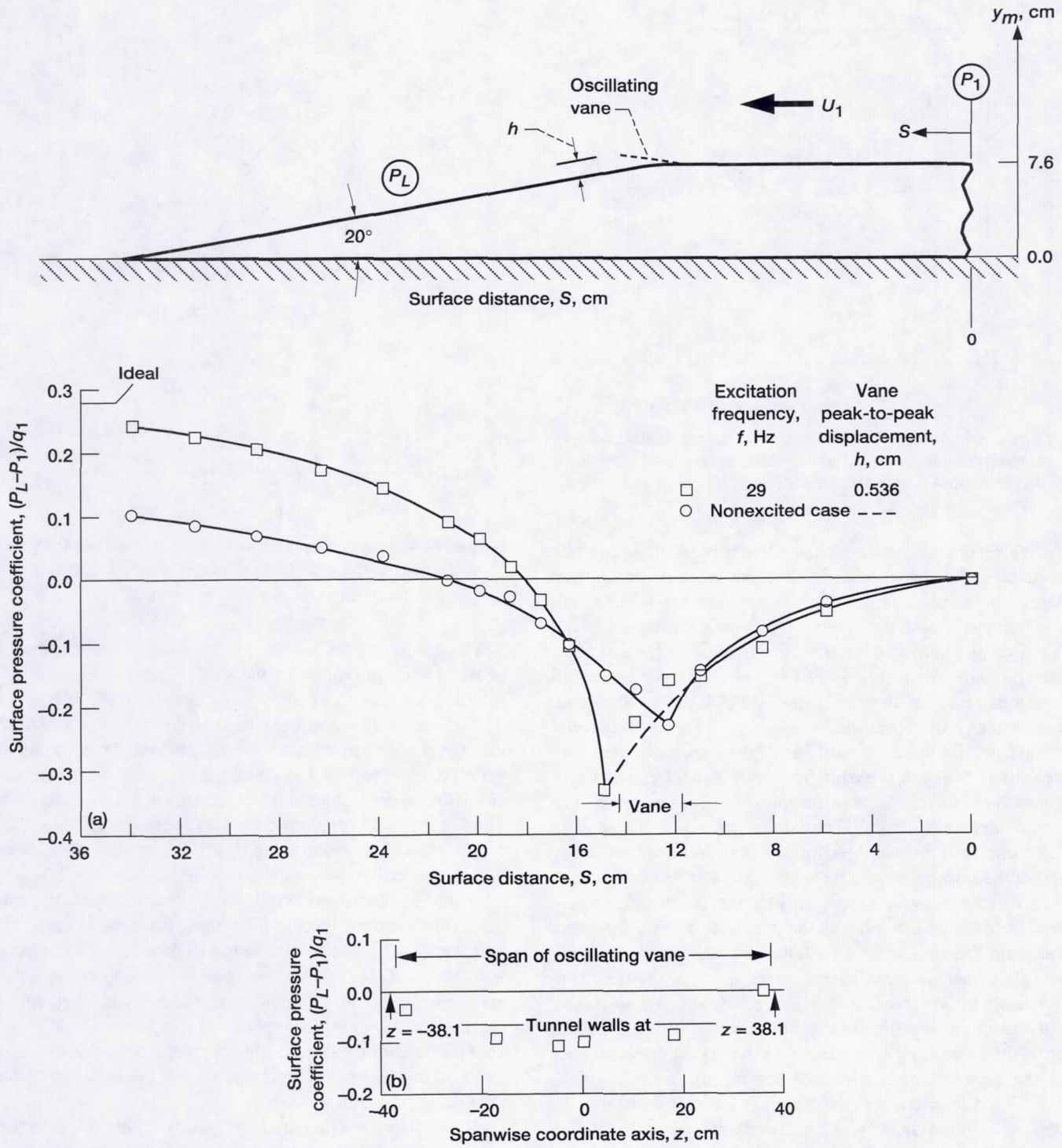

Figure 3.—Surface pressure coefficient distribution on model. (a) Axial distribution for excited and nonexcited cases; inlet velocity, U_1, 6.6 m/sec. (b) Spanwise distribution for excited case at surface distance S of 8.5 cm; inlet velocity, U_1, 6.6 m/sec; excitation frequency, f, 29 Hz; vane peak-to-peak displacement, h, 0.536 cm.

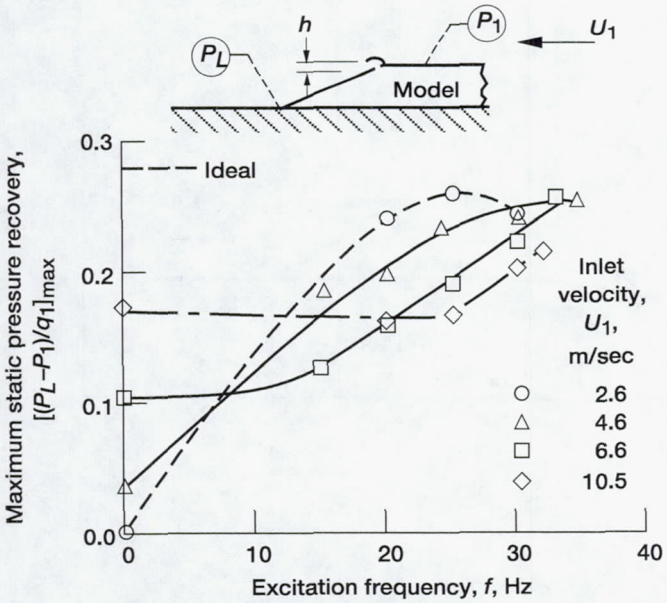

Figure 4.—Maximum static pressure recovery as function of excitation frequency f at constant vane peak-to-peak displacement h of 0.318 cm for four inlet velocities.

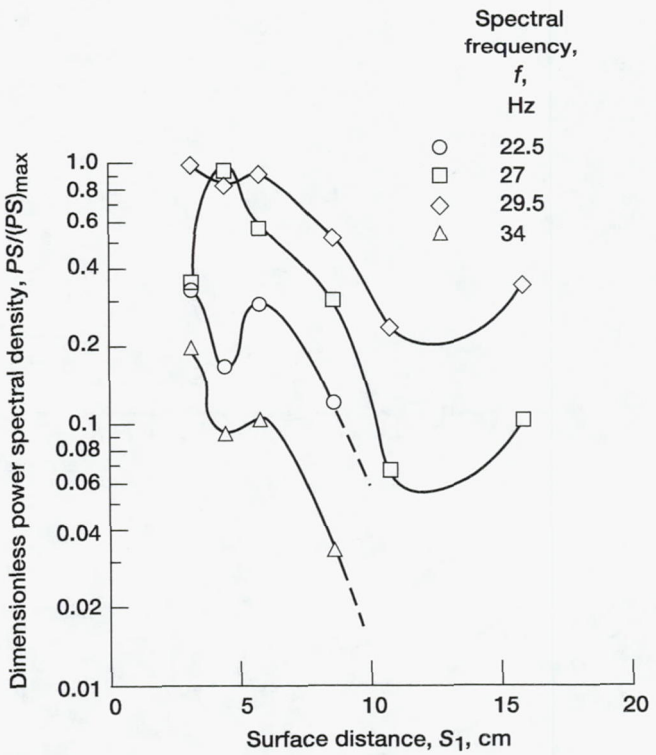

Figure 5.—Dimensionless power spectral density decay as function of surface distance S_1 for nonexcited case: Inlet velocity, U_1, 6.6 m/sec.

U_1, which implies that the phenomenon producing the optimum delay in detachment is Strouhal number dependent. Based on the observation that the data are approaching the ideal recovery limit, the optimum frequency for the 6.6-m/sec case is estimated to be 33 Hz. This is close to the so-called most probable frequency of 29.5 Hz measured just inside the perturbing edge of the nonexcited shear layer for the same inlet velocity of 6.6 m/sec (see fig. 5). The most probable frequencies for the 2.6-, 4.6-, and 10.5-m/sec cases were not measured. The most probable frequency is that frequency that corresponds to the peak in the power spectrum of the unforced, detached mixing layer over the ramp. These data represent, in dimensionless form, the power spectral decay determined from hot-wire measurements as a function of surface distance S_1, which represents the surface distance measured from the tangent point at the intersection of the upstream flat plate and the ramp at its inlet. An estimate of the most probable frequency can be calculated using Michalke's spatial theory of unstable disturbances (ref. 8) which predicts that the maximum amplification rate occurs at a Strouhal number of 0.017. Assuming that the maximum unstable disturbance of the nonexcited free shear layer for the test conditions considered here occurs at a Strouhal number of 0.017, the corresponding frequency of the disturbance was calculated to be 27.4 Hz. This calculation was based on the local momentum thickness measured at the same axial location along the model as the peak dimensionless power spectral density $PS/(PS)_{max}$ appearing in figure 5. This calculated value of the most probable frequency is close to the measured most probable frequency of 29.5 Hz.

The data presented in figure 6 represent a parametric study of the maximum values of the static pressure recovery as a function of h for the inlet velocities U_1 of 2.6, 6.6, and 10.5 m/sec at a constant excitation frequency of 24 Hz. The intercepts with the ordinate for the nonexcited case (vane not on model) represent the condition where flow detachment from the ramp surface did not occur over the entire ramp. Note that the maximum pressure recovery for all three cases increases with increasing values of h, reaching maxima between nominally 0.40 and 0.48 cm. Excluding the 2.6-m/sec case, the displacement amplitude h of about 0.40 cm represents the maxima for the 6.6- and 10.5-m/sec cases. This effect might be due to a saturation phenomenon (characterized by a decreasing effect with an increasing driver amplitude) that has to do with nonlinear instability mechanisms. In the case of jet mixing, references 13 and 14 presented experimental measurements and a theory predicting the saturation of jet mixing by single-frequency, plane-wave excitation, which may have some relevance here.

Figure 7 presents a parametric study for the U_1 of 6.6-m/sec case. Measurements of the surface pressure coefficient are presented as a function of surface distance S for five values of peak-to-peak displacement h at a constant excitation frequency f (fig. 7(a)) and for five values of f at a constant h (fig. 7(b)). At a surface location S of 15 cm, the magnitudes of the pressure coefficients progressively decrease, first, with

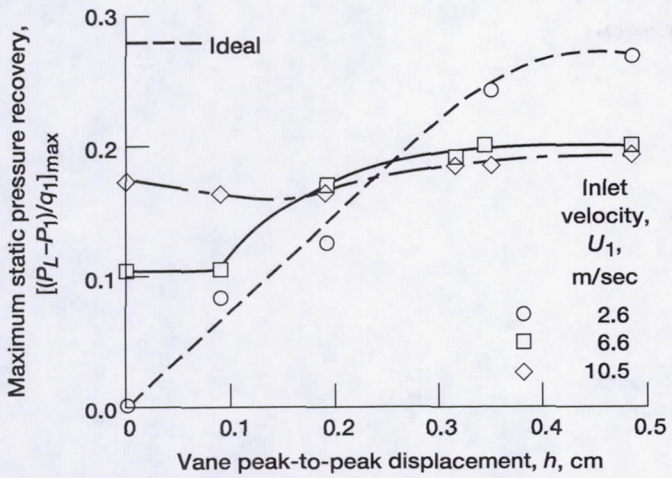

Figure 6.—Maximum static pressure recovery as function of vane peak-to-peak displacement h at constant excitation frequency f of 24 Hz for three inlet velocities.

increases in h at a constant f (fig. 7(a)) and second, with an increasing f at a constant h (fig. 7(b)). Thus, the pressure coefficient at this location is clearly dependent on the motion of the vane trailing edge. Because the vane oscillates in harmonic motion according to the relationship

$$y_v = \frac{h}{2}\sin(2\pi fT) \tag{1}$$

where T represents time, the fluctuating velocity of the vane trailing edge is expressed as

$$v_v = \frac{\partial y_v}{\partial T} = \pi fh\cos(2\pi fT) \tag{2}$$

The vane trailing edge rms velocity is given by

$$\left(v_{\text{rms}}\right)_v = \frac{\pi fh}{\sqrt{2}} \tag{3}$$

Thus, the vane trailing edge rms velocity $(v_{\text{rms}})_v$ theoretically varies as a direct function of the product of the vane oscillation frequency and its peak-to-peak displacement amplitude. Therefore, it can be concluded that the pressure coefficient in the vicinity of the vane varies as a negative function of the vane trailing edge rms velocity. At the location of maximum recovery (S = 34 cm), the static pressure recovery varies as a more complex positive function of the two independent variables, f and h; that is, it varies as a positive function of the vane oscillation frequency throughout the entire range of frequencies tested but over only a limited range of the trailing edge displacement amplitudes covered. More specifically, from a point nominally 2 cm downstream of the vane trailing edge to the exit of the ramp, the value of the pressure coefficient is independent of increases in the vane displacement amplitude above approximately 0.318 cm, which corresponds to 70 in inner wall boundary layer units y^+. Below this limiting amplitude, it varies as a function of both the frequency of the vane oscillation and its displacement. These observations suggest that two different responses to the operation of the vane are occurring.

At this point it must be mentioned that the effective operation of the oscillating vane was strongly dependent on the trailing edge closing completely down on the ramp surface. For example, as noted in figure 8, maintaining a constant gap height Δh_{offset} of 0.058 cm between the ramp surface and the lower limit of travel of the vane trailing edge and operating at a U_1 of 6.6 m/sec produced a 14-percent reduction in the maximum static pressure recovery in comparison with the case in which the vane completely closed down on the surface.

From this point on, the majority of the measured flow-field data presented were obtained at a ramp inlet velocity U_1 of 6.6 m/sec.

Flow Reversal Contours

The corona anemometer probe is an instrument capable of measuring the local flow reversal rate. In the present tests, the local flow reversal rate was determined from plots of the probability density function versus velocity. The velocity was determined from a calibration of the probe output voltage. Figure 9 presents two separate test conditions, with and without oscillation of the vane. The excited test condition was forced to occur to demonstrate the variation of the probability function versus output voltage for two different degrees of flow attachment to the ramp surface. They are presented for the purpose of demonstration only and are not examples of typical data presented in any other figures of this study. The data were obtained at a location halfway down the length of the ramp in the x, y-plane passing through the tunnel centerline (z = 0) and at a height of 0.127 cm above the model surface. This signal, in plus or minus dc volts, represents an averaged measure of the difference in ion current between the two low-voltage (target) electrodes of the probe (see fig.2 of ref.7). The area under the curve can be measured to determine the average flow reversal rate. The intercepts along the abscissa represent a measurement of the range of the unsteady gas velocity. For the nonexcited case, backflow (up the ramp) occurs nearly 80 percent of the time. In the event that the backflow occurred 100 percent of the time, the entire curve would lie in the negative range of the probe output voltage. Thus, the unsteady component of the output signal, although fluctuating, would always have a negative value. For the excited case, backflow occurs at this location for about 35 percent of the time. Thus, the data in figure 9 show that the oscillating vane delayed the flow detachment and improved the degree of flow attachment at the location of the probe.

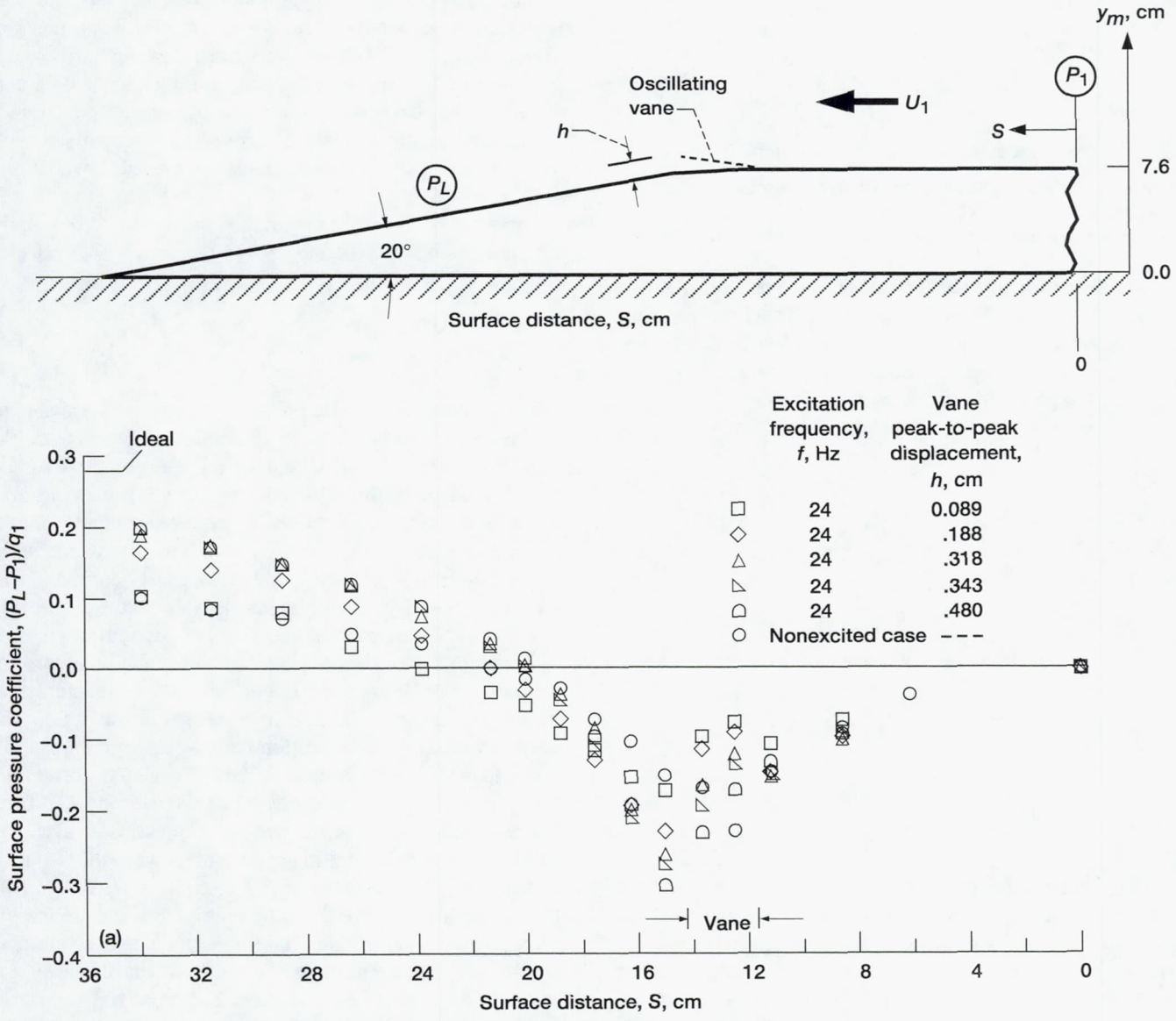

Figure 7.—Surface pressure coefficient distribution over ramp; inlet velocity, U_1, 6.6 m/sec. (a) Ramp surface pressure coefficient as function of vane peak-to-peak displacement h at constant excitation frequency f of 24 Hz. (b) Ramp surface pressure coefficient as function of excitation frequency f at constant vane peak-to-peak displacement h of 0.318 cm.

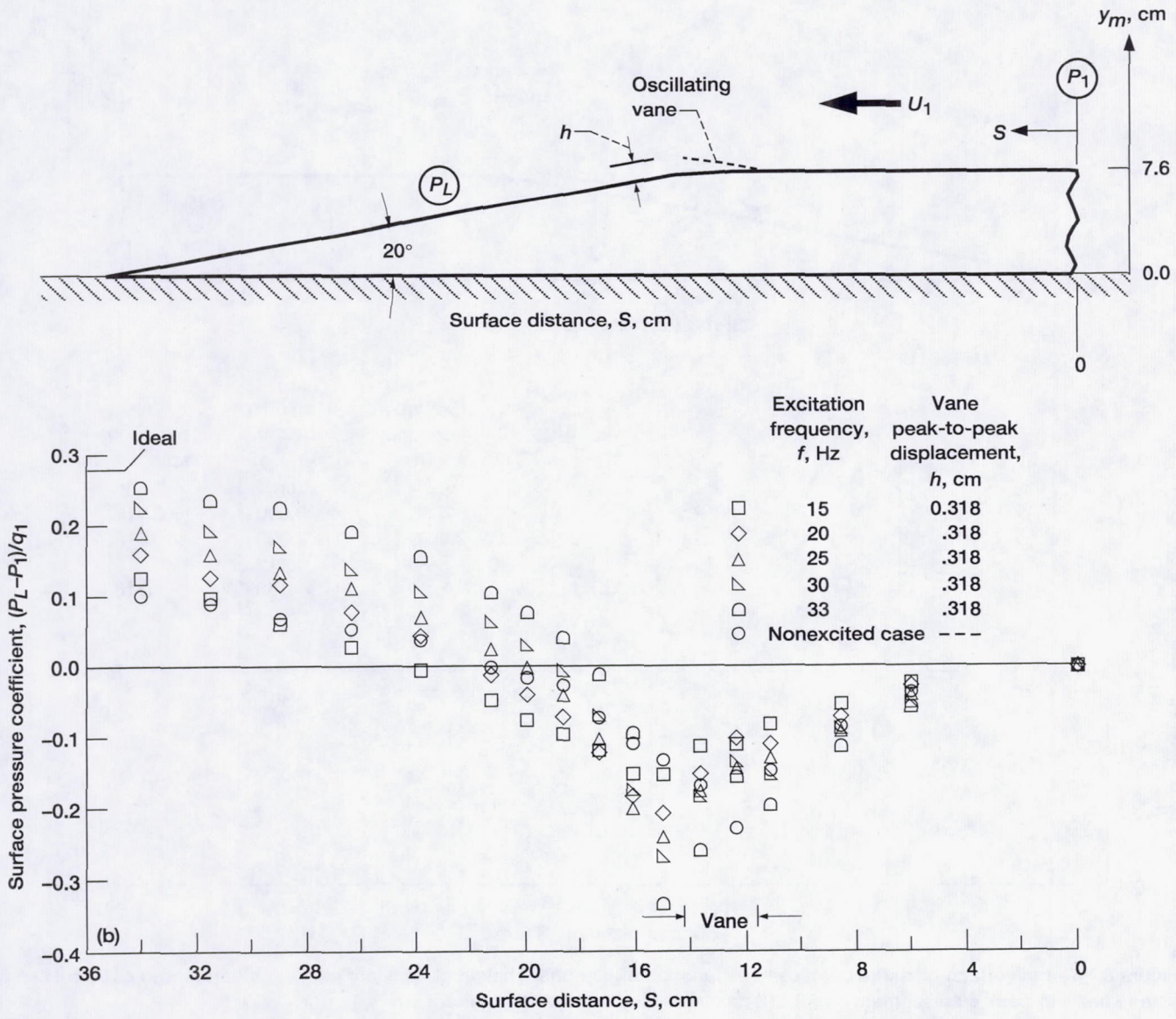

Figure 7.—Concluded. (b) Ramp surface pressure coefficient as function of excitation frequency f at constant vane peak-to-peak displacement h of 0.318 cm.

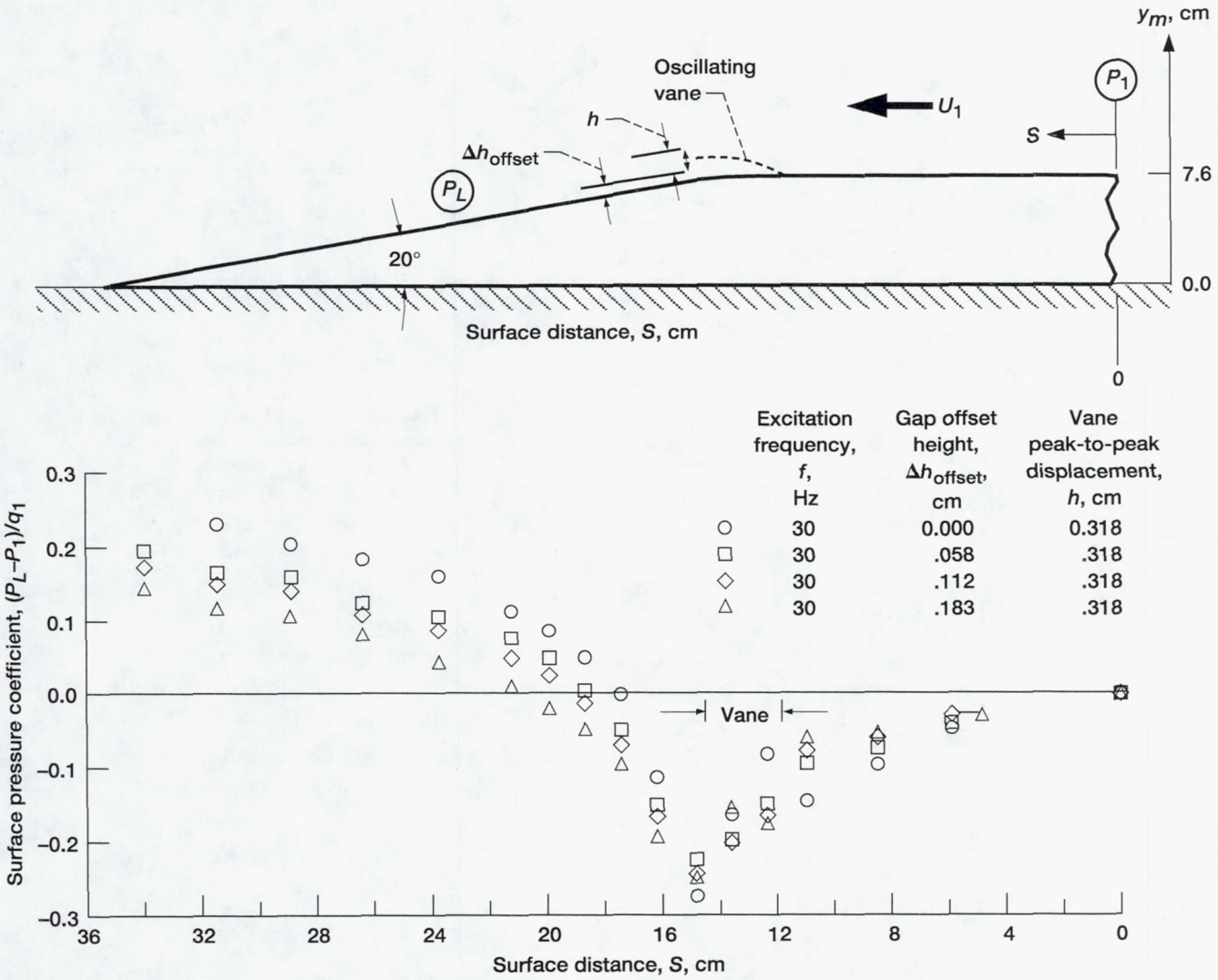

Figure 8.—Ramp surface pressure coefficient as function of gap offset height at constant excitation frequency f of 30 Hz and vane peak-to-peak displacement h of 0.318 cm; inlet velocity, U_1, 6.6 m/sec.

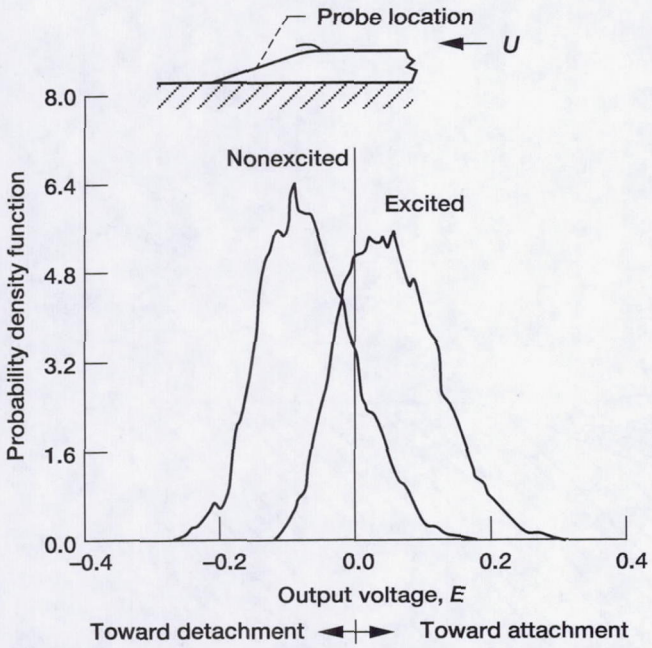

Figure 9.—Corona anemometer probe probability density function versus output voltage for excited and nonexcited cases. (Examples are for demonstration only and are not typical test data.)

Figure 10 presents contours of flow reversal rate over the ramp for the nonexcited and excited cases. The inner boundary of these measurements was 0.152 cm above the ramp surface, well within the inner wall region of the boundary layer. Figure 10(a) presents the nonexcited measurements showing that a 100-percent reversal rate contour was measured over a small portion of the ramp surface at a point nominally 2.2 cm downstream from the ramp inlet. The 50-percent-reversal-rate contour represents a boundary where the mean flow velocity is considered to be zero. Therefore, for contours greater than 50 percent, the mean flow is considered to be reversed. Note that most of the flow near the ramp surface is reversed. Thus, from a point nominally 2 cm downstream from the ramp inlet to its exit, the mean flow may be considered to be in a detached state. Figure 10(b) presents the excited case showing that in the inner wall region the flow is attached with a maximum reversal rate of only 6 percent near the ramp exit. These data indicate that although the flow within the inner region of the boundary layer has an unsteady component of velocity, it is attached to the ramp surface at all times; thus, detachment, if it exists at all, has been delayed to a point downstream from the ramp exit. In summary, figure 10(b) clearly shows that detachment was delayed and also the degree and extent of the attachment. In addition, the dynamic nature of the oscillating vane makes it possible to vary the degree of attachment. For example, in a particular application, it may be desirable to locally create conditions of only limited attachment requiring that the average flow reversal rate be controlled. Such a requirement is relatively simple to satisfy using this device. From an investigational point, the ability to control the degree of attachment and maintain it not only permits a rare opportunity to investigate the global cause-and-effect aspects of such a device as determined by variations in the axial surface static pressure distribution but also provides the opportunity to investigate the more fundamental question of how such a particular mechanically generated perturbing signal reacts with the hydrodynamic flow field to eventually excite instability waves and generate turbulence in an unstable boundary layer.

All the data discussed thus far demonstrate a cause-and-effect relationship between the operation of the vane and a delay in the detachment of the nonexcited flow passing over the 20° rearward-facing ramp. In addition, they indicate that two different responses to the operation of the vane occurred.

To investigate these two responses in greater detail, we will begin with a discussion of the flow field. In an attempt to orient the reader to the discussion of the flow field, a sketch in cartoon form is presented in figure 11(a). Based on smoke-wire flow visualization data, the sketch portrays the formation of a series of complex, time-dependent structures observed to develop periodically, but not simultaneously, in the flow. These structures develop by the action of the oscillating vane as the flow passes over the ramp. In the sketch, the surface length of the ramp is separated into sections showing five prominent events, each of which appeared periodically only in that section of the ramp. For example, event 1 occurring at time T_1 is the formation of two large-scale structures by the action of the vane during each cycle of its operation. One remains attached to the surface while the second one remains detached. Event 2 at T_2 is the dynamic interaction between the two formed structures. Event 3 at T_3 is the interaction of the detached structures with the mean flow velocity gradient producing a large mushroom-shaped structure. Event 4 at T_4 is the appearance of an axially rotating structure in the outer region of the boundary layer. Event 5 at T_5 is the formation of smaller omega-shaped structures in the near wall region of the boundary layer. In total, these events present a very complex picture of the flow field. Figure 11(b) presents several of the smoke-wire photographs from which the individual depictions in figure 11(a) were drawn. The following discussion of the flow field will consider first the phenomena originating in the immediate vicinity of the vane and continuing along the ramp surface in the buffer layer and linear sublayer of the excited boundary layer. Second are the phenomena occurring downstream of the vane and above the ramp surface in the logarithmic-law region and outer layer of the excited boundary layer.

Results in Vicinity of Vane and in Buffer Layer and Linear Sublayer of Boundary Layer

Before discussing the details of the flow field in the vicinity of the vane and along the ramp surface in the buffer layer and linear sublayer of the excited boundary layer, the type of

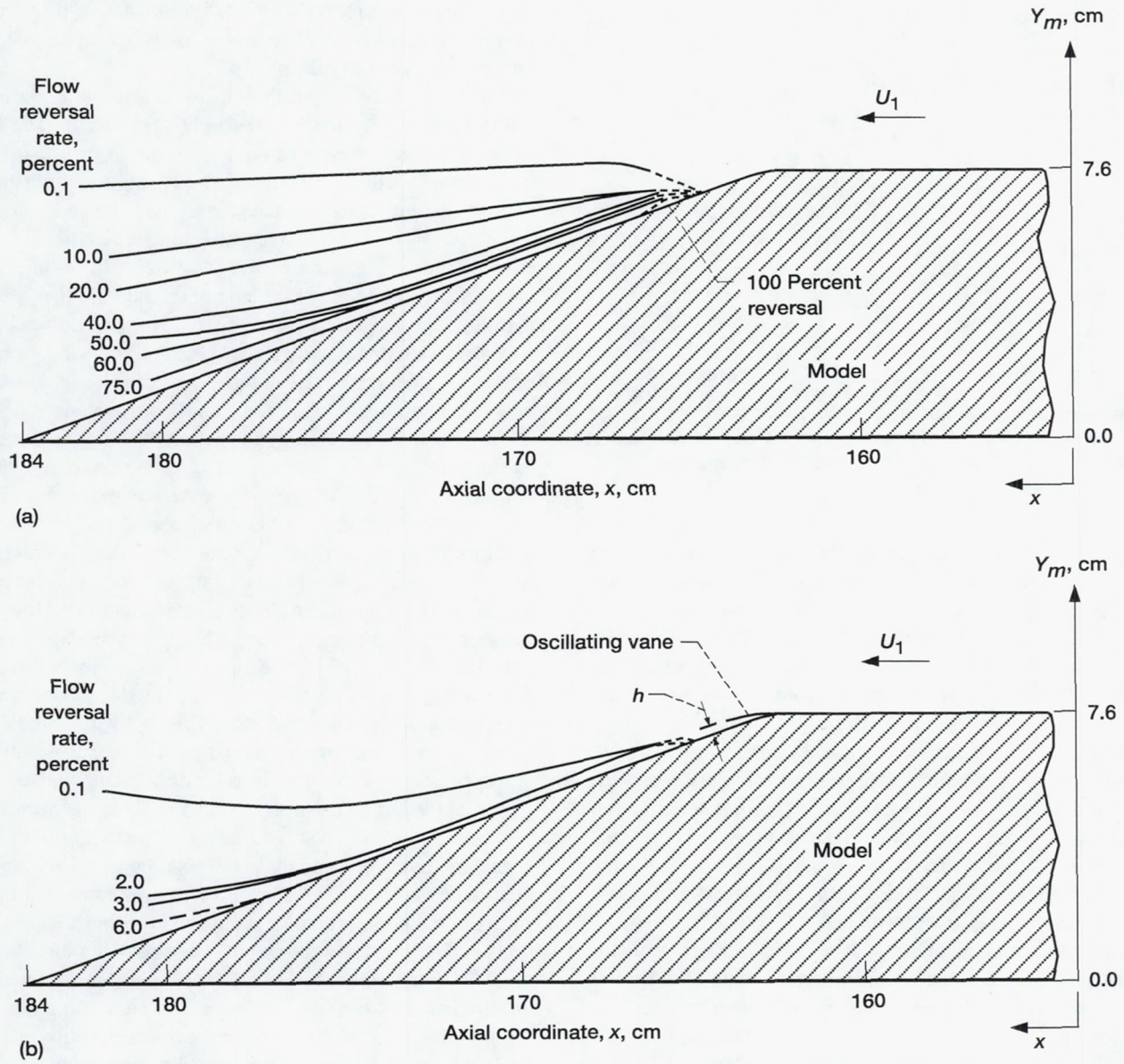

Figure 10.—Contours of flow reversal rate for nonexcited and excited cases; inlet velocity, U_1, 6.6 m/sec. (a) Nonexcited case. (b) Excited case; excitation frequency, f, 30 Hz; vane peak-to-peak displacement, h, 0.318 cm.

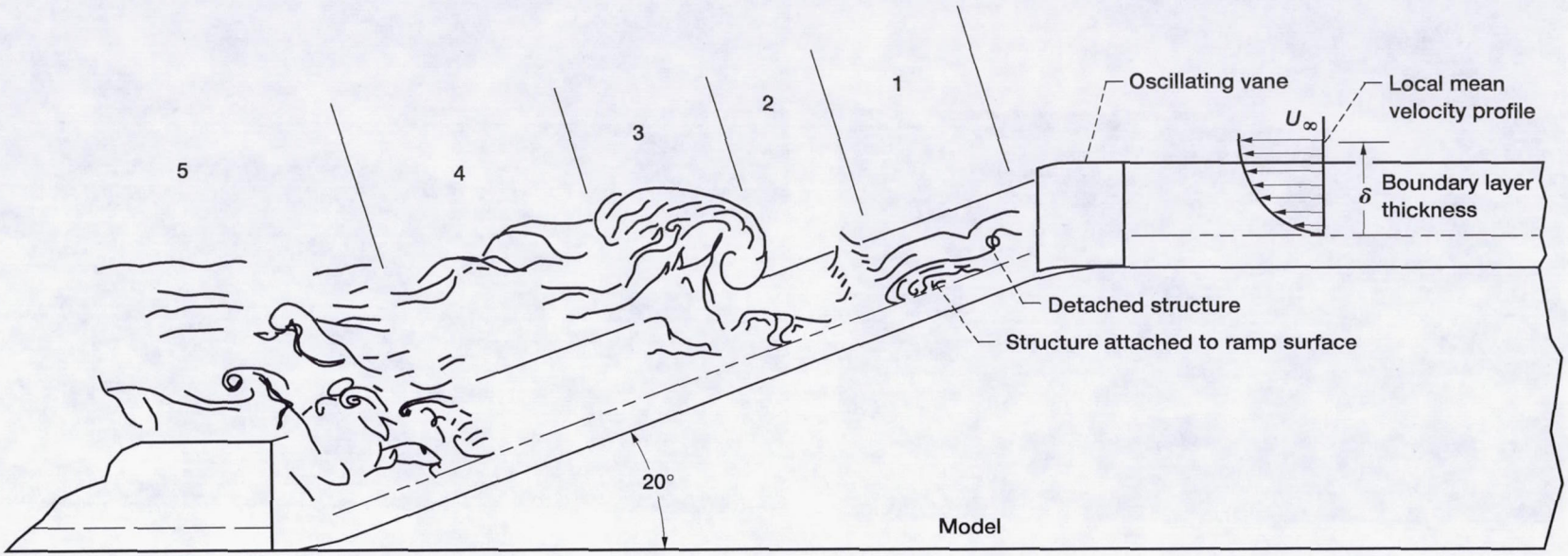

Periodic event	Description
1	Two spanwise, large-scale structures formed by vane
2	Dynamic interaction between spanwise structures
3	Periodic formation of mushroom-shaped structures
4	Axially rotating structure
5	Formation of omega-shaped structures

(a)

Figure 11.—Periodic events produced by action of oscillating vane that delays detachment of flow passing over 20° rearward-facing ramp. (a) Oblique side view of five periodic events. (b) Smoke-wire photographs represented in sketches of figure 11(a).

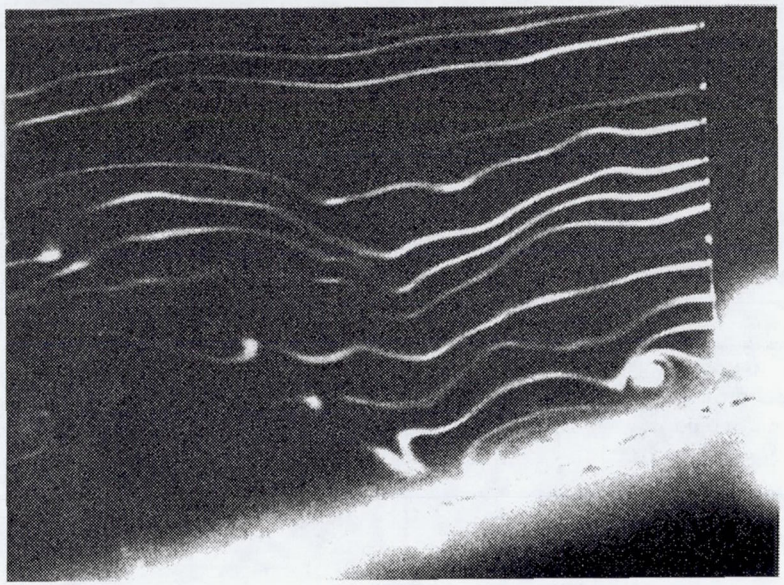

Event 1

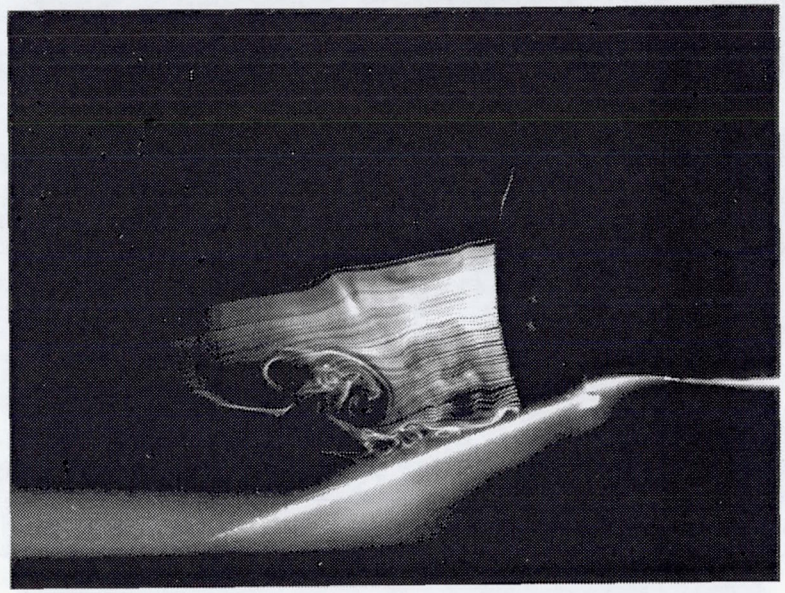

Event 3

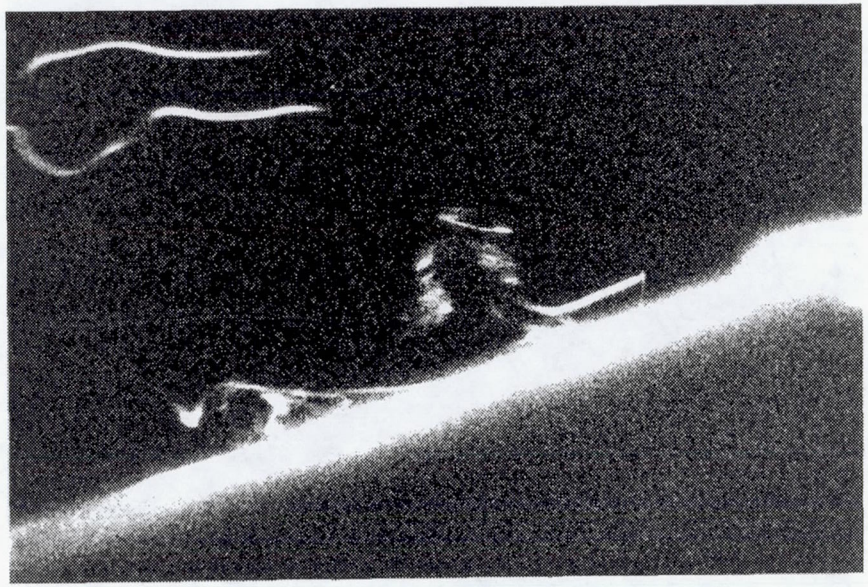

Event 2

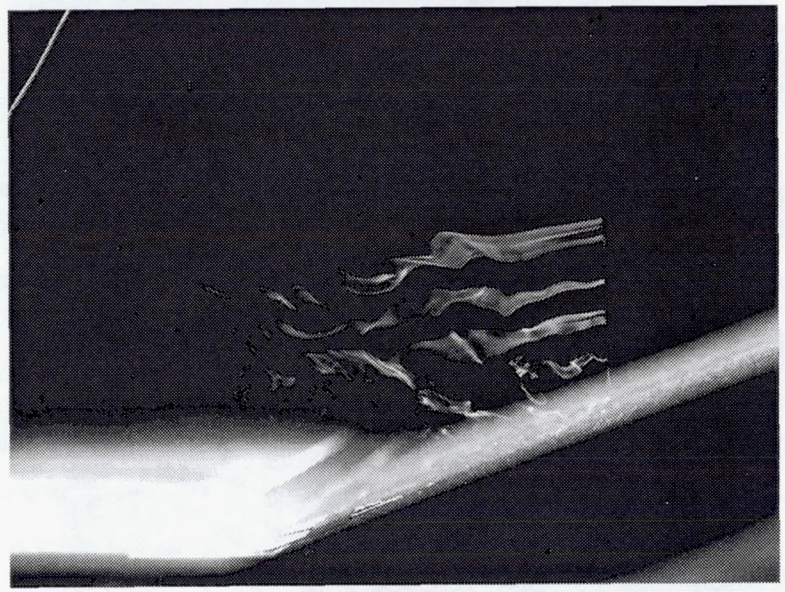

Event 4

Figure 11.—Concluded. (b) Smoke-wire photographs represented in sketches of figure 11(a).

boundary layer upstream of the ramp will be discussed. Figure 12 presents the shape factor H, the momentum thickness θ, and the Reynolds number based on momentum thickness Re_θ as a function of the model surface distance S_1 (referenced to the ramp inlet tangent point to the cylindrical transition section at the crest of the ramp). The boundary layer thickness δ at an S_1 of –0.95 cm was 3.05 cm. In the case of a flat plate, the shape factor is known to decrease from 2.6 in the laminar regime to 1.4 in the turbulent regime and to rise to 1.8 at detachment. In addition, the Reynolds number based on momentum thickness for a turbulent boundary layer should be greater than 1000. The data presented in figure 12, measured well upstream of the ramp inlet at an S_1 of –48 cm, indicate that the shape factor for the nonexcited case was 1.38, while just upstream of where detachment occurred at an S_1 of 2.39 cm, it rose to 1.79. These data and the measured value of Re_θ greater than 1000 indicate that the boundary layer upstream of the ramp inlet was turbulent. For the excited case, note that the shape factor rose from a nominal value of 1.35 at an S_1 of –0.94 cm to 2.66 at an S_1 of 18.9 cm near the ramp exit. For an attached turbulent boundary layer, the latter value of the shape factor is very high and suggests that some extraordinary phenomena are occurring at this location near the ramp surface.

Hot-wire data.—Figures 13 and 14 present single-hot-wire mean flow boundary layer velocity profiles in the x,y-plane passing through the model spanwise centerline ($z = 0$) at two axial locations for both nonexcited and excited conditions. Figures 13 and 14 present data 0.16 cm upstream of the vane leading edge (S of 11.52 cm) and at L of 0.48 cm downstream of the vane trailing edge, respectively. A comparison of the curves in each figure indicates that an increase in the mean velocity occurred with excitation and a decrease in the nonexcited case, implying in the excited case that the flow is being accelerated as it changes direction along the curved surface of the ramp inlet. The velocity profiles presented in figure 14 are of particular interest because they were obtained just upstream of the point where the natural nonexcited boundary layer detached. The comparison indicates that for the excited case a change, in the form of a wall jet, occurred in the mean flow velocity profile. This represents a change in the spanwise component z of the vorticity and suggests the possibility that two two-dimensional vortices may be present near the wall. The possible presence of these two vortices is important for a qualitative explanation of the phenomena producing the delay in detachment on the rearward-facing ramp considered herein. It must be remembered that the initial condition of the flow field is one in which the flow is not excited and the boundary layer is detached from the ramp surface at a point 2.2 cm downstream from the ramp inlet. It is this condition that the oscillating vane initially affects; that is, the vane is periodically forming a volume of fluid containing accumulated vorticity that may or may not roll up to form a vortex. In either case, the periodically formed volume leaves the vicinity

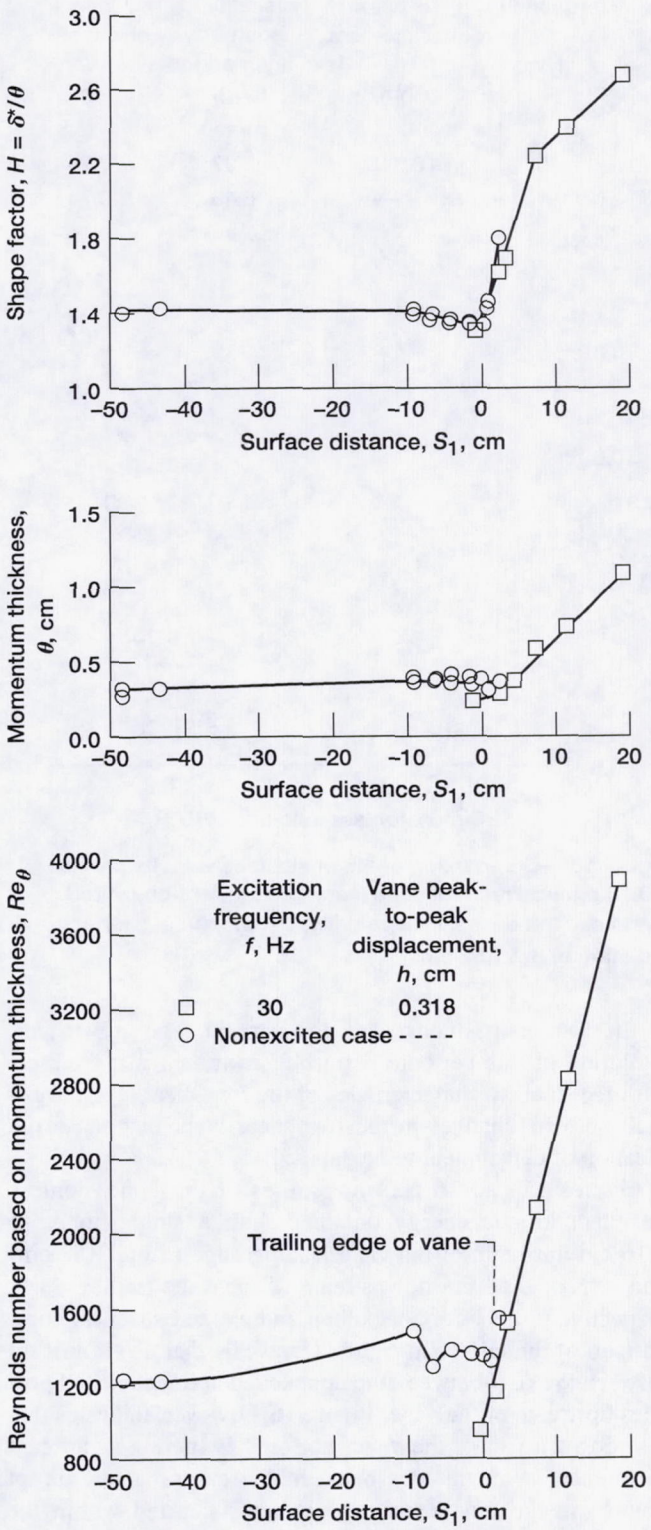

Figure 12.—Shape factor, momentum thickness, and Reynolds number versus surface distance for nonexcited and excited cases: inlet velocity, U_1, 6.6 m/sec.

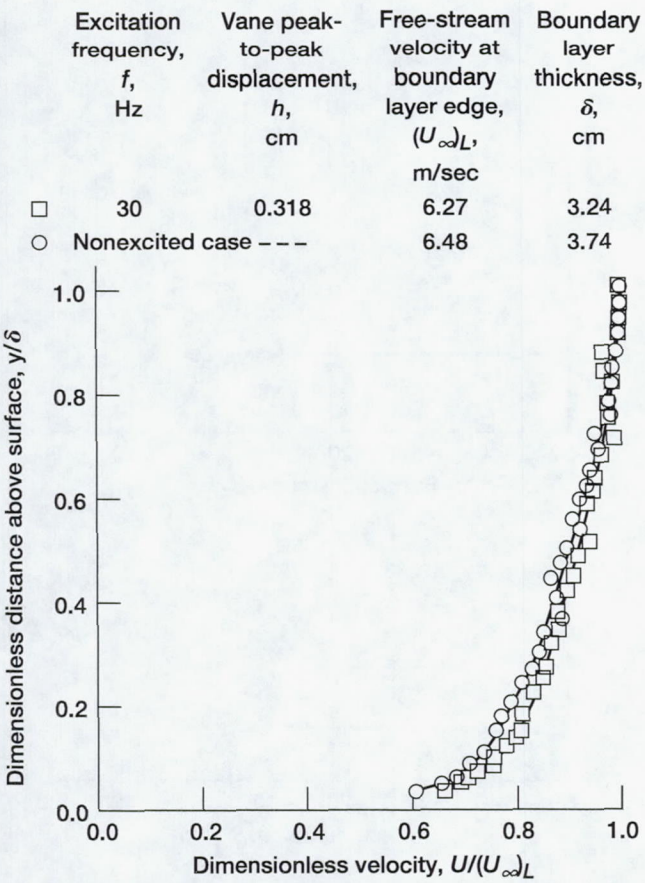

Figure 13.—Comparison of dimensionless velocity profiles 0.16 cm upstream of vane leading edge for nonexcited and excited cases; inlet velocity, U_1, 6.6 m/sec; surface distance, S, 11.52 cm.

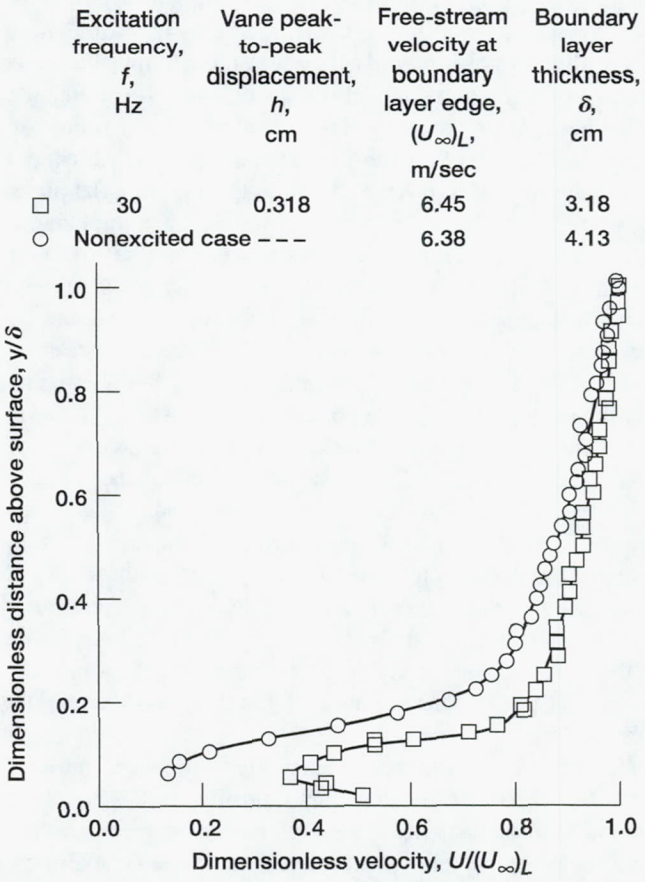

Figure 14.—Comparison of dimensionless velocity profiles at L of 0.48 cm downstream of vane trailing edge for nonexcited and excited cases; inlet velocity, U_1, 6.6 m/sec.

of the vane and is convected downstream. The growth and evolution of this periodic perturbing volume, as it interacts with the stability characteristics of the free shear layer, eventually effects changes in the free shear layer that cause the location of detachment to be delayed.

Figures 15 and 16 present profiles of the dimensionless turbulent kinetic energy obtained with a single hot wire 0.16 cm upstream of the vane leading edge (S of 11.52 cm) and at L of 0.48 cm downstream of the vane trailing edge, respectively, for both nonexcited and excited cases. A comparison of the curves in figure 15 reveals that no significant difference exists between the nonexcited and the excited profiles upstream of the vane. Figure 16, however, indicates that just downstream of the vane, not only is there a significant difference in magnitudes between the cases but an abrupt change in the kinetic energy gradient occurred within the lower 10 percent of the boundary layer for the excited case. This change and the corresponding change in the gradient of the turbulence intensity support the contention that vortices may be present at this location. The measured peak turbulence intensities, based on the local free-stream velocity for the excited case, had nominal values of 24 percent. When referenced to the local mean velocity in the boundary layer, this value rises to nominally 46 percent, which is very high. In comparison, the calculated value of the vane trailing edge rms fluctuating velocity was 3.2 percent of the local free-stream velocity. Thus, between the vane trailing edge and a point 0.48 cm downstream from it, the turbulence intensity, based on the local free-stream velocity, increased approximately sevenfold. This significant growth is a consequence of the nonexcited turbulent boundary layer (experiencing detachment) responding to the small amplitude of a periodic perturbing signal produced by the oscillating vane. It should be kept in mind that for the excited case presented in figures 13 through 16, the vane was oscillated at 30 Hz, which is also the most probable frequency of the nonexcited case.

Figures 17(a) and (b) present the mean flow boundary layer and turbulent kinetic energy profiles, respectively, for the excited condition at L of 1.90 cm downstream of the vane trailing edge. In figure 17(a) in the near wall region of the boundary layer, note the nearly linear variation of the velocity with the distance above the surface y/δ. Figure 17(b) indicates

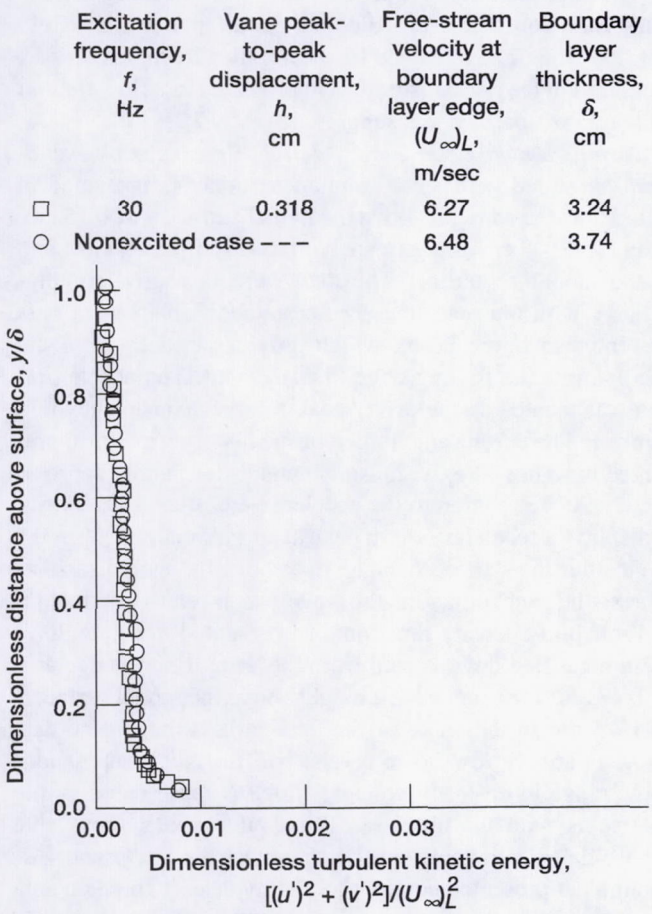

Figure 15.—Comparison of dimensionless turbulent kinetic energy profiles 0.16 cm upstream of vane leading edge for nonexcited and excited cases; inlet velocity, U_1, 6.6 m/sec; surface distance, S, 11.52 cm.

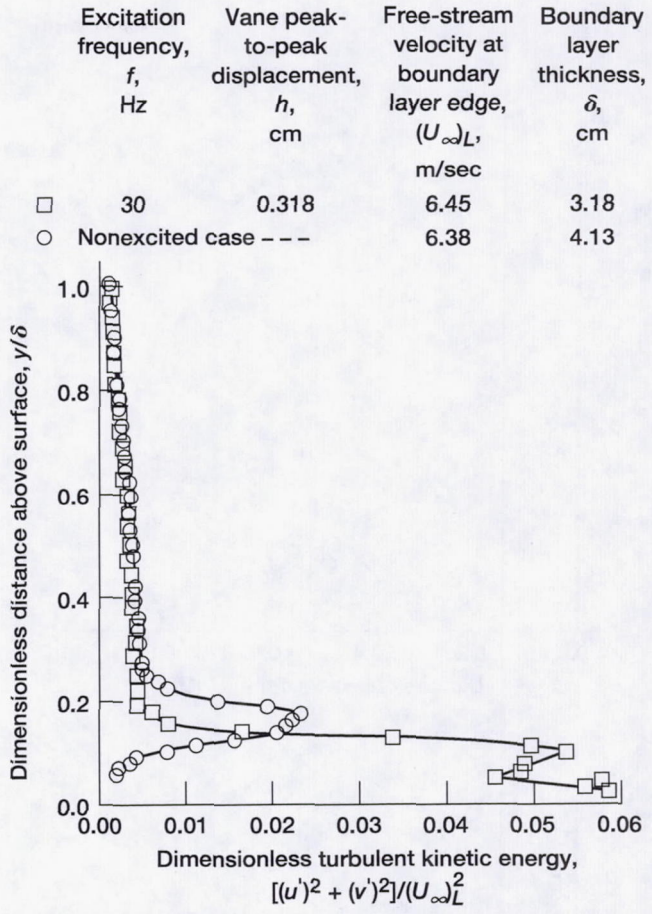

Figure 16.—Comparison of dimensionless turbulent kinetic energy profiles at L of 0.48 cm downstream of vane trailing edge for nonexcited and excited cases; inlet velocity, U_1, 6.6 m/sec.

that within the near wall region up to a y/δ of approximately 0.17, erratic changes in the turbulent kinetic energy are occurring in the downstream wake from the vane. Power spectral data presented in figure 18 measured at distances L of 0.48 and 1.9 cm downstream of the vane trailing edge and at a height y of 0.152 cm above the ramp surface indicate that a strong, fundamental narrow-bandwidth, 30-Hz fluctuating signal and its harmonics were present. Therefore, the turbulent kinetic energy profile data include periodic (but varying in amplitude), narrow-bandwidth fluctuations superimposed on an otherwise broadband spectrum.

Figure 19 is a presentation of the Reynolds shearing stress profile for the excited condition at L of 1.90 cm downstream of the vane. These nonsmooth data may be revealing the presence of the thin layers which Bradshaw (ref. 15) proposed to contain high-Reynolds-stress gradients and are discussed in appendix A. The smallest Reynolds shearing stress level is –0.006 in the inner wall region. The negative sign and level of this stress are unusual and will be discussed further. The absolute magnitude is considered high; however, Oster and Wygnanski (ref. 16) present experimental measurements of the forced excitation of two parallel streams in which shearing stresses approached 0.004; they consider this value high if it were measured in an unexcited flow. Thus, the magnitude of the Reynolds stresses presented in figure 19 appear to be reasonable. Considering the negative sign of the Reynolds stresses measured in the present study, reference 16 indicates that negative Reynolds stresses were produced in the region of a free shear layer flow field in which vortex pairing was suppressed. Reference 16 also noted that negative Reynolds stresses may be associated with the inclination of the large structures. Power spectral measurements presented in figure 18 show a dominant narrow-bandwidth fluctuating signal at the vane oscillation frequency of 30 Hz. This disturbance signal remained dominant and persisted in the near wall region of the flow field between the trailing edge of the vane and the ramp exit. At an L of 0.48 cm in figure 18(b), a broad distribution of turbulent kinetic energy is noted in the narrow-bandwidth spikes below and above 30 Hz. At an L of 1.9 cm, however, a distinct 15-Hz, narrow-bandwidth subharmonic is

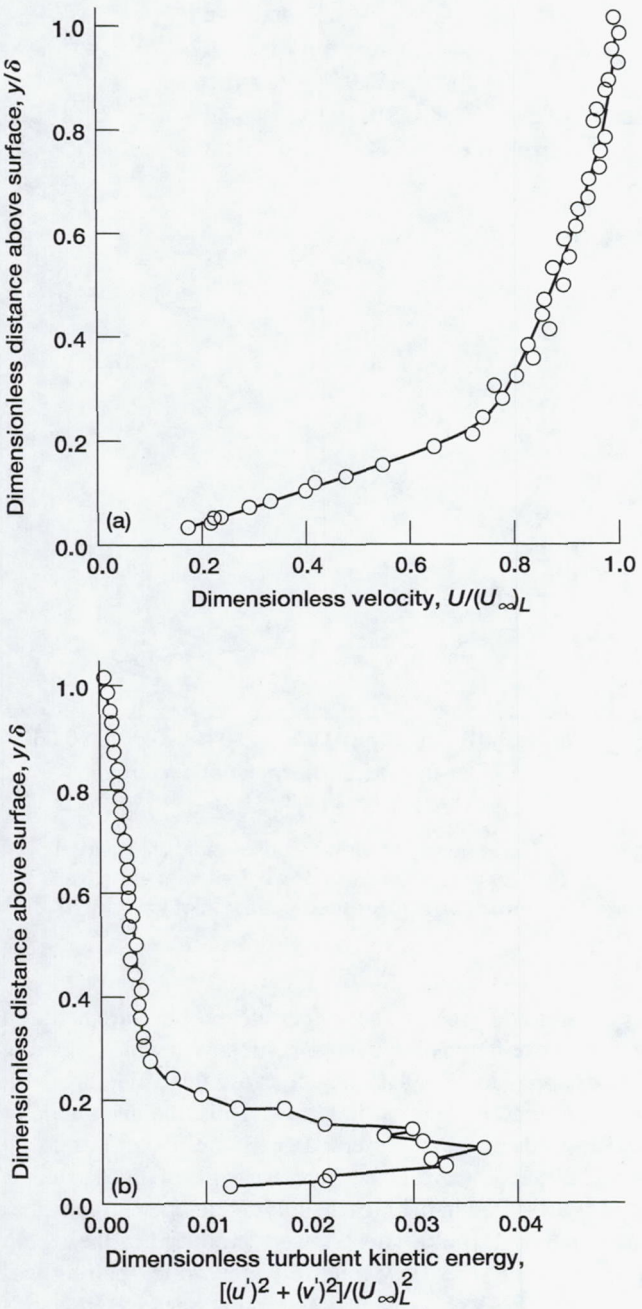

Figure 17.—Dimensionless velocity and turbulent kinetic energy profiles at L of 1.90 cm downstream of vane trailing edge for excited case; inlet velocity, U_1, 6.6 m/sec; excitation frequency, f, 30 Hz; vane peak-to-peak displacement; h, 0.318 cm; free-stream velocity at boundary layer edge, $(U_\infty)_L$, 6.54 m/sec; boundary layer thickness, δ, 3.57 cm. (a) Dimensionless velocity profile. (b) Dimensionless turbulent kinetic energy profile.

not present, the lack of which is significant because it indicates that vortex pairing did not occur in the flow field (ref. 17). Thus, like reference 16, the negative Reynolds stresses measured in the present study were produced in a flow field in which vortex pairing was suppressed (ref. 17).

Corona anemometer data.—A real-time velocity waveform measured with the corona anemometer is presented in figure 20(a) at a height above the model surface y of 0.15 cm, at an L of 0.48 cm downstream from the oscillating vane, and at the model centerline. The data were measured simultaneously with the real-time accelerometer displacement data presented in figure 20(b), which provides a measure of the oscillating vane trailing edge displacement. The accelerometer was located on the driver push-rod mechanism shown in figure 1. The corona anemometer time history waveform presented in figure 20(a) is sinusoidal and is delayed by approximately 90° in relation to the accelerometer trace (fig. 20(b)). It displays a secondary sharp peak at approximately 90° in the cycle after the start of the vane rise above the model surface. During the vane retraction, the waveform is relatively smooth.

Probability density function data presented in figure 20(c) were measured downstream from the vane trailing edge at L of 0.48 and 1.90 cm and at a height above the model surface y of 0.15 cm in the wake of the oscillating vane. These data show relatively low noise levels, two distinct peaks, and a large range in unsteady voltage, which is represented by the intercepts with the abscissa. The double peaks imply that sinusoidal disturbances are being sensed by the probe. Although not presented herein, probability density function data were measured for the nonexcited case, and they display only single peaks. The voltage ranges of the data presented in figure 20(c) represent maximum fluctuating flow speeds of approximately 53 and 62 percent of the free-stream velocity at locations L from the vane of 0.48 and 1.90 cm, respectively. Although the flow contains large fluctuations at an L of 0.48 cm, it is moving downstream at all times. At an L of 1.90 cm, it again contains large fluctuations but has a reversal rate of approximately 4 percent. This rate means that although the mean motion is moving downstream at all times (zero reversal rate), the fluctuating component in the upstream direction is larger than the mean velocity downstream for approximately 4 percent of the time; thus the flow appears to reverse 4 percent of the time.

Figure 21 presents data measured at a single point in space in the wake of the oscillating vane at a location L of 0.48 cm downstream from the vane trailing edge and at a height y 0.15 cm above the model surface for ramp inlet velocities U_1 of 0 and 6.6 m/sec. Figure 21(a) presents the measured angle of lag between the real-time displacement waveform of an accelerometer displacement signal located on the vane actuation mechanism linkage and the waveform of the real-time air velocity measured using the corona anemometer. Figures 21(b) and (c) present single-point local mean and fluctuating velocities, respectively, measured using the corona anemometer

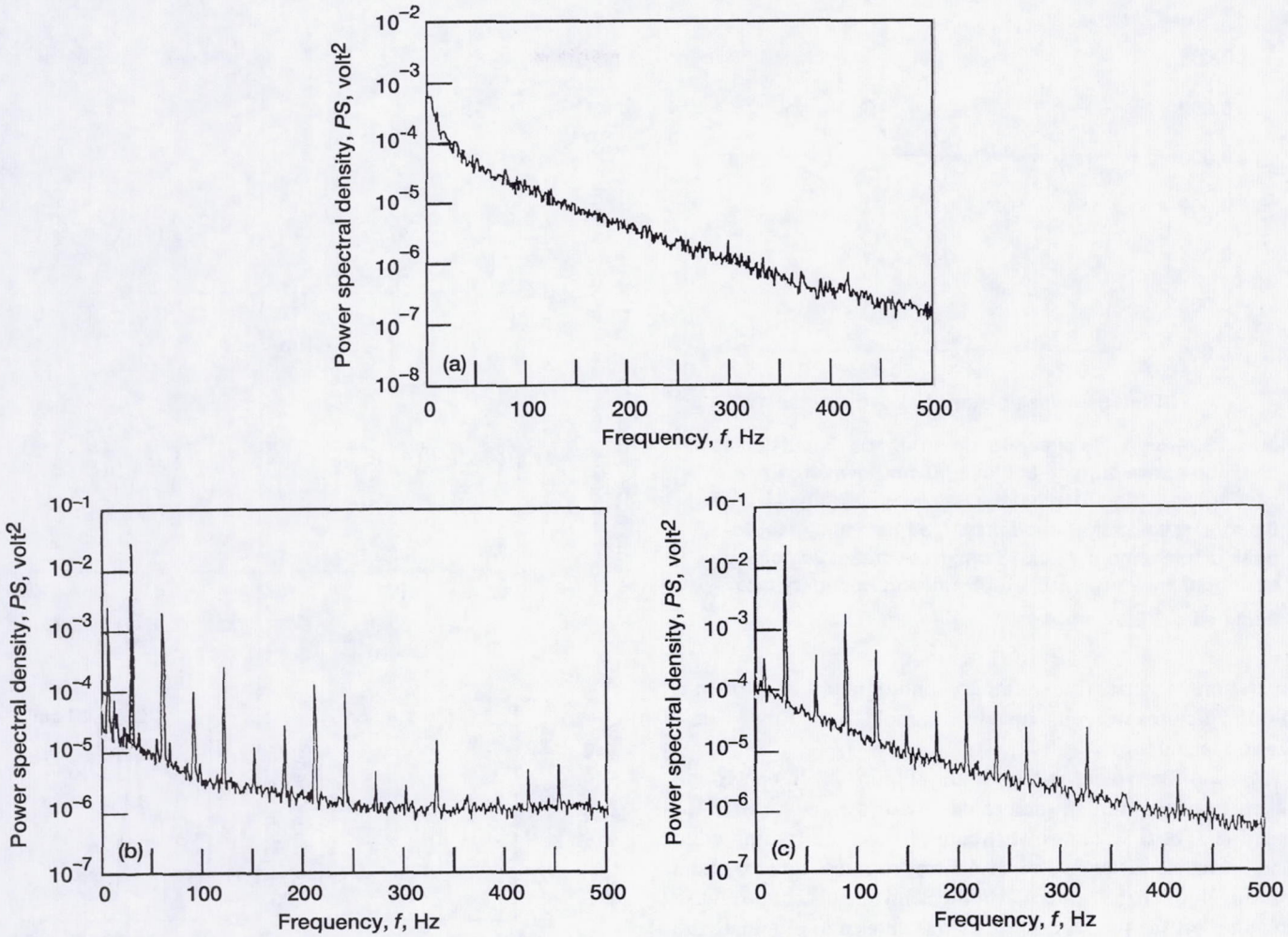

Figure 18.—Power spectra measured at two locations downstream of vane trailing edge and at y_P of 0.152 cm above ramp surface; inlet velocity U_1, 6.6 m/sec. (a) Nonexcited case (vane down on surface); distance downstream of vane trailing edge, L, 0.48 cm; power spectral density, PS, 0.089×10^{-3} volt^2 at 30 Hz. (b) Excited case; distance downstream of vane trailing edge, L, 0.48 cm; power spectral density, PS, 30.5×10^{-3} volt^2 at 30 Hz; vane peak-to-peak displacement, h, 0.318 cm. (c) Excited case; distance downstream of vane trailing edge, L, 1.9 cm; power spectral density, PS, 24.9×10^{-3} volt^2 at 30 Hz; vane peak-to-peak displacement, h, 0.318 cm.

located at L of 0.48 cm downstream from the vane trailing edge and a height y of 0.15 cm above the model surface. For no mean inlet flow ($U_1 = 0$), the vane induced local mean velocities between nominally 0.5 and 1.0 m/sec over a range of oscillating frequencies from 18 to 33 Hz. For the case in which the ramp inlet velocity was 6.6 m/sec, the mean velocity increased to nominally 2.0 m/sec at 18 Hz and 3.0 m/sec for a range of frequencies from 20 to 33 Hz. The fluctuating component u' was 0.4 m/sec for the case of no mean inlet flow. For the case in which the ramp inlet velocity was 6.6 m/sec, u' increased to nominally 0.8 m/sec between vane oscillating frequencies of 20 and 30 Hz. The lag angle decreased, as expected, with increasing oscillation frequency for both cases; however, it showed a slower rate of decrease for the case in which the inlet velocity was 6.6 m/sec.

The data presented in figures 14 and 16 through 20 indicate that the flow in the vicinity of the vane is very complex and suggest that the oscillating vane is producing two spanwise vortices per cycle of its operation. Specifically, these data indicate that large unsteady flow speeds approaching 60 percent of the local free-stream value occurred at the height of the vane wake in the near wall region of the boundary layer. Power spectral data (fig. 18) measured in this same region show the presence of a strong, fundamental narrow-bandwidth, 30-Hz fluctuating signal and its harmonics. These measurements suggest the existence of inflection points in the instantaneous velocity profiles, which could act to initiate secondary instabilities producing turbulence in the near wall region. To investigate in greater detail the possibility that the oscillating vane is producing two vortices per cycle of its

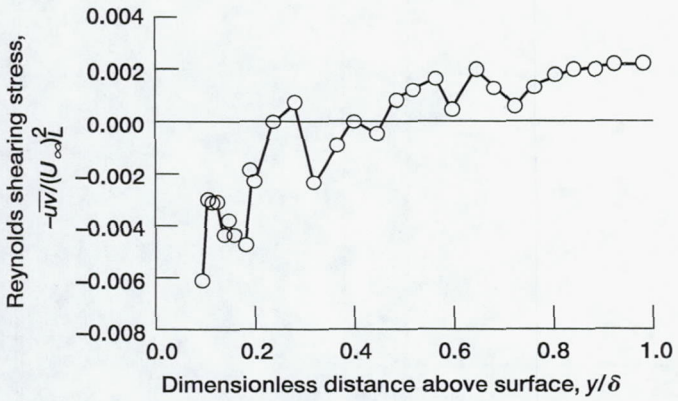

Figure 19.—Reynolds shearing stress versus dimensionless distance above surface at L of 1.90 cm downstream of vane trailing edge for excited case; inlet velocity, U_1, 6.6 m/sec; excitation frequency, f, 30 Hz; vane peak-to-peak displacement, h, 0.318 cm; free-stream velocity at boundary layer edge,$(U_\infty)_L$, 6.54 m/sec; boundary layer thickness, δ, 3.57 cm.

operation, a series of stationary photographs and 16-mm motion pictures were obtained using smoke-wire flow visualization techniques.

Smoke-wire visualization data.—Figure 22 is one frame taken from the motion picture data with the smoke wire located at L of 0.32 cm downstream of the vane trailing edge and spanwise distance z of 11.43 cm from the vertical plane passing through the centerline of the wind tunnel. The spanwise location off the model centerline was chosen to eliminate the remote possibility of capturing erroneous effects caused by the three, small, final flexible links in the vane drive train, as discussed earlier in the Apparatus and Instrumentation section. These data were obtained at a free-stream inlet velocity to the ramp of 2.6 m/sec with the vane oscillating at 25 Hz and for a vane displacement height h of 0.318 cm. The flow is passing from right to left, and the ramp surface is shown with the vane (out of focus) located at its crest. The vane has just reached its maximum displacement height and has started to retract. Notice that there are two spanwise (z-coordinate) vortices present. One lies on the surface, is larger, and is centered approximately 2.5 cm downstream from the vane trailing edge. The other is located approximately 0.32 cm above the surface and 0.5 cm downstream from the vane. The vortex attached to the surface may induce a secondary vortex because of its proximity to the surface. The detached vortex appears to be a regular rotating "spun-up" type, where $\partial V/\partial x$ roughly equals $\partial U/\partial y$; this vortex was released from the vane as it started to retract. The two vortices appear to be connected by braided vortices. The spanwise vortices were caused by the impulsive action of the external force applied to the vane by the actuator mechanism. If this impulsive force is assumed to uniformly affect the finite volume of gas over its surface, the

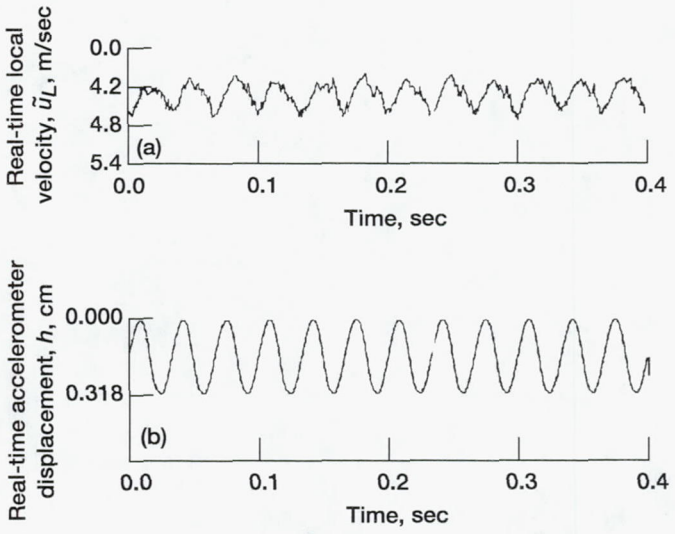

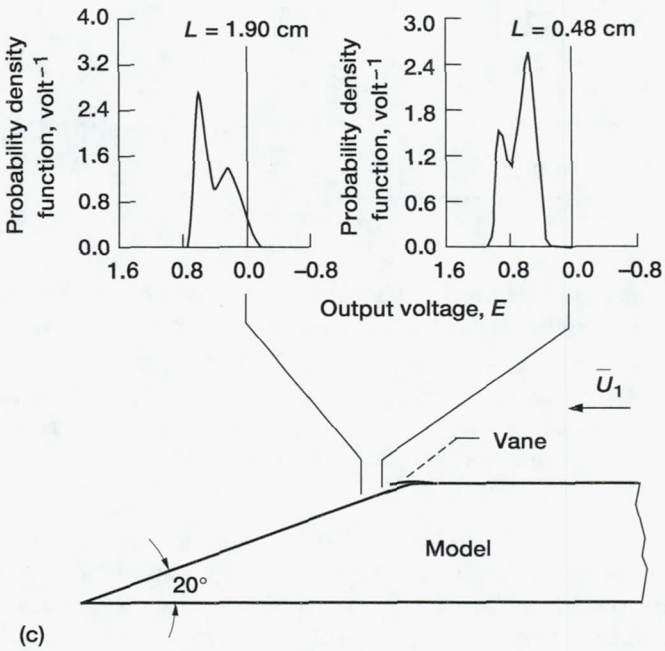

Figure 20.—Data measured for excited case; inlet velocity, U_1, 6.6 m/sec; vane peak-to-peak displacement, h, 0.318 cm; excitation frequency, f, 30 Hz. (a) Corona anemometer real-time velocity waveform at L of 0.48 cm downstream of vane trailing edge at height of 0.15 cm. (b) Accelerometer located on vane driver mechanism; real-time displacement. (c) Corona anemometer probability density function versus output voltage measured at L of 0.48 and 1.90 cm down-stream of vane trailing edge; height, 0.15 cm.

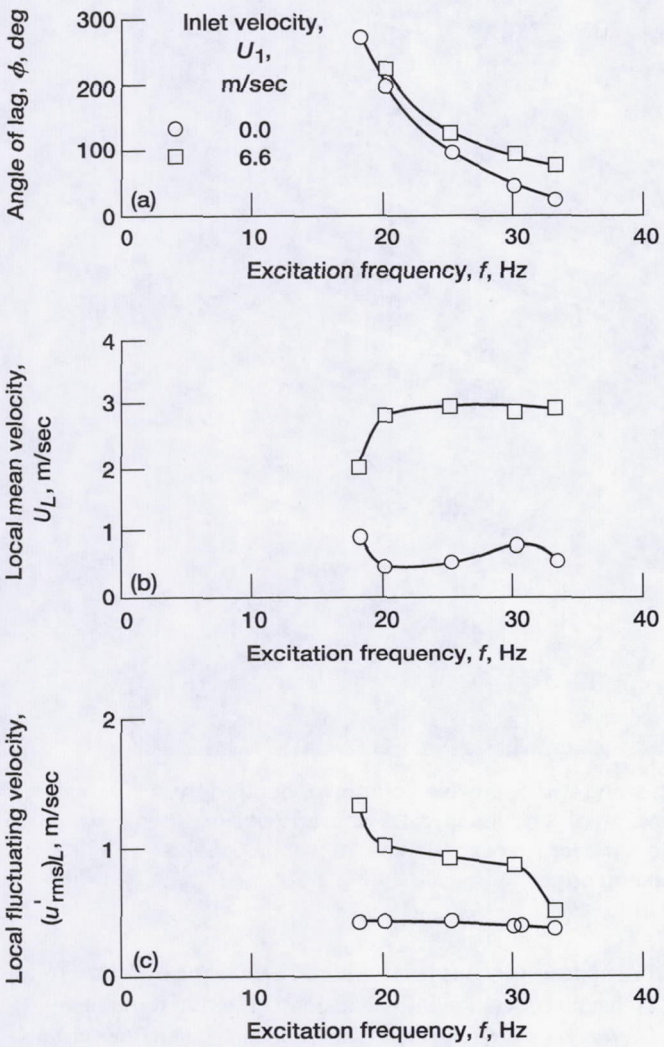

Figure 21.—Angle of lag, mean velocity, and fluctuating velocity as functions of excitation frequency measured at *L* of 0.48 cm downstream from vane trailing edge and 0.15 cm above model surface; inlet velocity, U_1, 0.0 and 6.6 m/sec; vane peak-to-peak displacement, *h*, 0.318 cm. (a) Angle of lag between displacement waveforms of oscillating vane trailing edge and local gas velocity U_L. (b) Local mean velocity. (c) Local fluctuating velocity.

force per unit volume at the vane edges will decrease rapidly to zero, creating vorticity (ref. 18). Thus, as the load on the vane changed sign during its oscillation, the vane acted as an oscillating airfoil with the steady release of the counter-rotating spanwise starting and lifting line vortices. The presence of these counter-rotating spanwise vortices was inferred by the abrupt change in the sign of the velocity gradient of the mean flow velocity profile presented in figure 14 and measured at an *L* of 0.48 cm downstream of the vane. A typical sequence of events is shown by the motion picture frames presented in figure 23 and begins with the starting vortex appearing on the ramp surface as the vane begins to open to its full displacement height. The starting vortex attaches itself and remains attached to the wall layer as it is convected downstream. When the vane reaches its maximum displacement height and begins to retract, the lifting line vortex is released and remains detached from the surface.

Turbulent boundary layer velocity profiles: wall-wake equation.—An analysis of the turbulent boundary layer velocity profiles shown in figures 14 and 17(a) was performed to learn more about the flow field. The profiles were measured at *L* of 0.48 and 1.90 cm, respectively, downstream from the oscillating vane trailing edge where the flow field was affected by streamline curvature and the vortices introduced by the oscillating vane. Initially, it was assumed herein that the standard form of the law of the wall-wake equation applied. This form represents a simple shear layer in which the local-equilibrium approximation is assumed to apply in the inner layer but outside the viscous sublayer. The following brief discussion is based on the presentation by Zierke and Deutsch (ref. 19) and on a figure taken from Bradshaw (ref. 20). Figure 24 presents the wall layer nomenclature in inner wall coordinates u^+ and y^+, which are slightly modified from reference 20. As shown, the boundary layer is composed of a series of regions. The region of the viscous sublayer is dominated by viscous shear and is self-similar for all turbulent boundary layers. It is described mathematically as

$$u^+ = y^+ \tag{4}$$

where u^+ and y^+ are functions of u_τ, the friction velocity. Outside the sublayer, but still close to the wall, the velocity is logarithmic and described by

$$u^+ = \frac{1}{k}\ln y^+ + C \tag{5}$$

where k is Karmon's constant and C is a constant that is a measure of the change in the dimensionless velocity across the viscous sublayer. Both constants were assumed here to be 0.41 and 5, respectively. These equations represent the viscous sublayer and the log-law region (fig. 24) and collectively are called the law of the wall. Streamwise pressure gradients have only a small influence on this inner layer region. Outward from the inner layer, the streamwise pressure gradients are important and the velocity profile exhibits a wavelike form. An equation for the wake region, the law of the wake (ref. 21), includes a wavelike function and when added to the log-law, equation (5), is called the wall-wake equation:

$$u^+ = \frac{1}{k}\ln y^+ + C + \frac{\Pi}{k} W\left(\frac{y}{\delta}\right) \tag{6}$$

where Π is the wake parameter and $W(y/\delta)$ is the wake function, equal to $2\sin^2[\pi(y/2\delta)]$. Thus, the third term on the right-

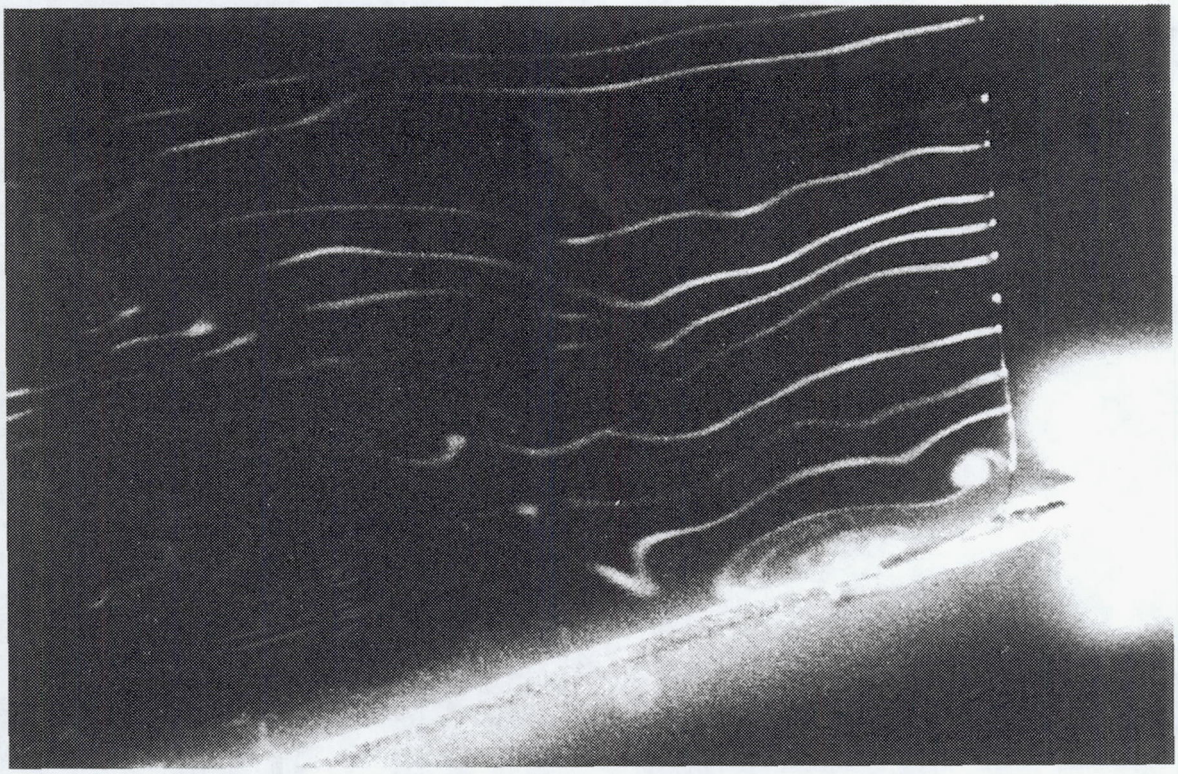

Figure 22.—Single frame from motion picture sequence showing two spanwise vortices generated by action of oscillating vane. Inlet velocity, U_1, 2.6 m/sec; excitation frequency, f, 25 Hz; vane peak-to-peak displacement, h, 0.318 cm. Flow direction is from right to left over rearward-facing 20° ramp. Smoke wire is located at L of 0.32 cm downstream from vane trailing edge.

hand side of equation (6) incorporates the effect of the streamwise pressure gradient.

The analysis of the turbulent boundary layers presented in figures 25 and 26 includes a fit of the measured velocity profile data to the wall-wake equation using the procedure of Zierke and Deutsch (ref. 19). These figures present velocity profile data in inner wall coordinates measured at L of 0.48 and 1.90 cm, respectively, from the oscillating vane trailing edge. A least-squares fit of the raw data to the equation was made with u_τ and Π as the variables to be determined and δ as a known quantity. To optimize the fit of the measured data to the wall-wake equation, it is necessary to establish lower and upper bounds of the measured data to be used in the fit. For example, with reference to figure 24, the measured data that the analyst determines to represent the viscous sublayer is eliminated from the fitting procedure so that only data representing the defect-law region of the boundary layer are used to make the fit. As can be noted from figures 25 and 26, this procedure has resulted in what appears to be a very good fit in the upper portion of the measured profiles, with the remainder of the data appearing to make a transition to the sublayer at abnormally large values of y^+. In addition, note that each set of data include two logarithmic regions separated by a transition region. An explanation for this is related to the work appearing in the text entitled *Turbulence* by Hinze (ref. 22) that considers the influence of an effective roughness.

Effect on buffer layer.—The boundary layer flow visualization photographs presented in figures 22 and 23 show that two spanwise vortices are produced by the oscillating vane during each cycle of its operation. One of these vortices remains attached to the ramp surface as it moves downstream. Therefore, this attached vortex acts as an obstacle or an effective roughness to the remaining nonvortical fluid in the near wall region as it passes downstream along the surface. The resulting mean flow velocity profiles presented in figures 25 and 26 include the effects of this phenomenon and are analyzed with the aid of reference 22. The observation is made in reference 22 that a logarithmic velocity variation is attained at much higher values of y^+ in the case of an extremely rough wall where the height of the roughness element k_e is not very small compared with that of δ. In the case of the velocity profile data presented in figure 25, if it is assumed that the roughness element is equal to the diameter of the vortex attached to the ramp surface (shown in fig. 22), the ratio of the roughness element (k_e = 0.32 cm) to the boundary layer height (δ = 3.2 cm) is 0.1. Therefore this ratio is not very small and satisfies the condition of an extremely rough wall. A second observation (ref. 22) indicates that an

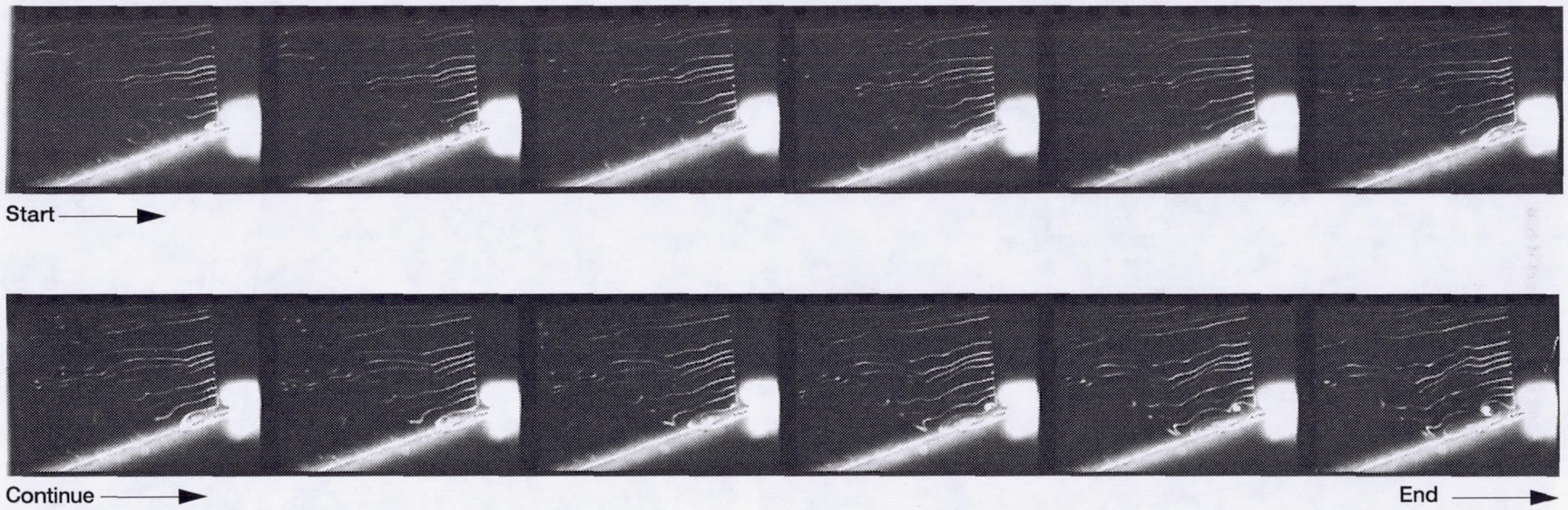

Figure 23.—Typical smoke-wire motion picture sequence of vane oscillating at 25 Hz; vane peak-to-peak displacement, h, 0.318 cm. Flow is passing from right to left at inlet velocity U_1 of 2.6 m/sec. Smoke wire is located at L of 0.32 cm downstream from vane trailing edge. Each frame represents a 0.0025-sec step in time.

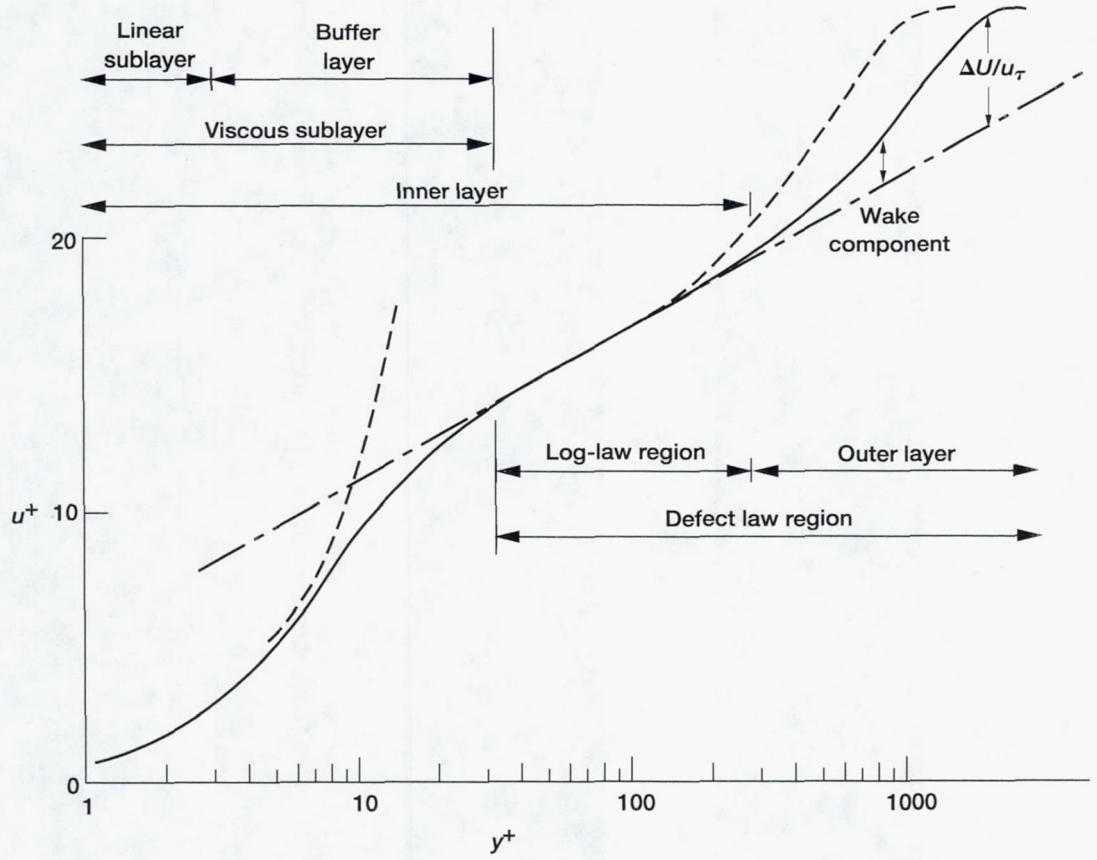

Figure 24.—Wall layer nomenclature in inner wall coordinates (fig. modified from ref. 20).

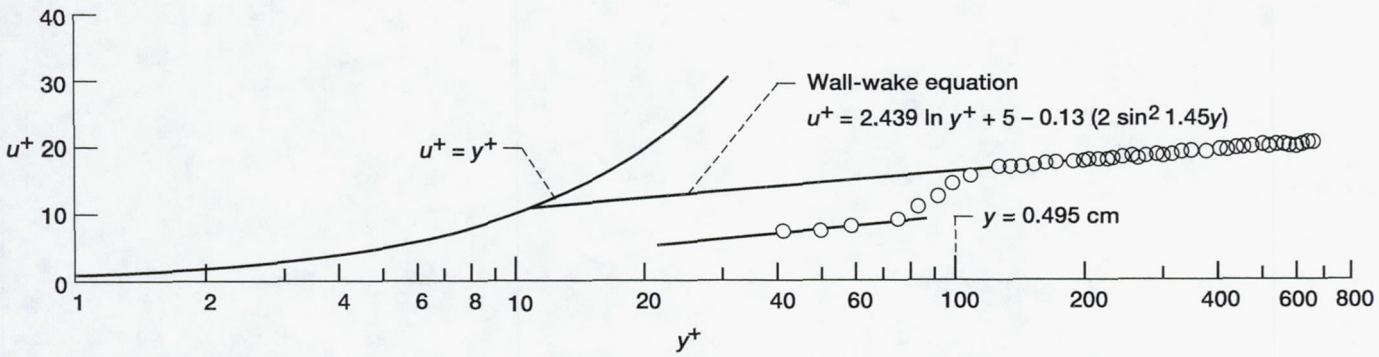

Figure 25.—Velocity profile in inner wall coordinates at L of 0.48 cm downstream from vane trailing edge; inlet velocity, U_1, 6.6 m/sec; excitation frequency, f, 30 Hz; vane peak-to-peak displacement, h, 0.318 cm.

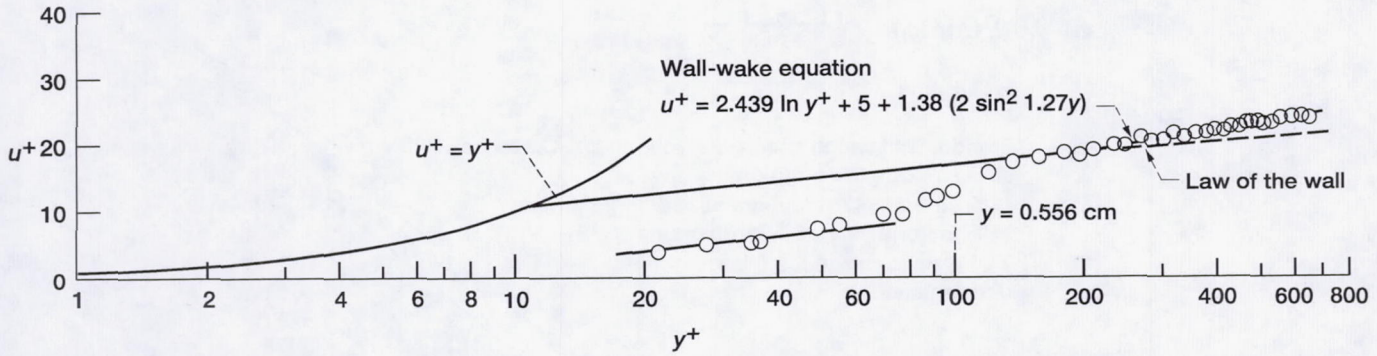

Figure 26.—Velocity profile in inner wall coordinates at L of 1.90 cm downstream from vane trailing edge; inlet velocity, U_1, 6.6 m/sec; excitation frequency, f, 30 Hz; vane peak-to-peak displacement, h, 0.318 cm.

increase in the roughness produces a decrease in the height of the viscous sublayer δ_l. This decrease occurs because roughness causes disturbances in the flow that extend the lower limit of the buffer layer toward the surface. Based on experimental measurements of flow through circular pipes with walls of uniform sand grain roughness, Rotta (ref. 23) derived a graphical relationship between δ_l and k_e that is presented in figure 27. From this figure it may be concluded that for small values of the effective roughness parameter $(u_\tau k_e)/\nu$, the effect on the viscous sublayer parameter $(u_\tau \delta_l)/\nu$, is small but that for $(u_\tau k_e)/\nu > 55$, a fully rough-wall condition exists with no effective viscous sublayer. The relationship in figure 27 refers to a unique set of measurements that may differ for other types of roughness, but they indicate that there will be a lower value of $(u_\tau k_e)/\nu$ below which the wall is fluid dynamically smooth and represents the perfectly smooth-wall condition.

Reference 22 indicates that the results led Hama (ref. 24) to derive the following equation for a rough wall:

$$\left(\frac{U}{u_\tau}\right)_r = \frac{1}{k}\ln\frac{u_\tau y}{\nu} + C - \left(\frac{1}{k}\ln\frac{u_\tau k_e}{\nu} + C - B_1\right) \qquad (7)$$

or expressed in inner wall coordinates

$$u_r^+ = \frac{1}{k}\ln y^+ + C - \left(\frac{1}{k}\ln y_{k_e}^+ + C - B_1\right) \qquad (8)$$

where B_1 is a constant.

This equation indicates that the effect of the wall roughness is to vertically shift the velocity distribution for a smooth wall by the value

$$u_s^+ - u_r^+ = \left(\frac{1}{k}\ln y_{k_e}^+ + C - B_1\right) \qquad (9)$$

where $u_s^+ = \frac{1}{k}\ln y^+ + C$. Equation (9) may be expressed in expanded notation as

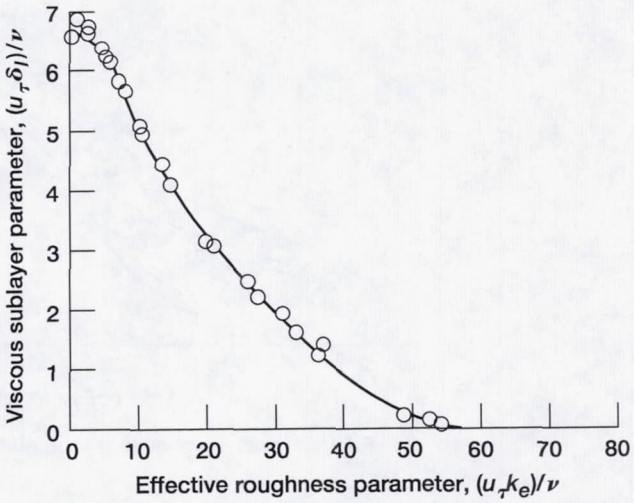

Figure 27.—Effect of wall roughness on viscous sublayer thickness according to experiments with uniform sand grain roughness (from ref. 23).

$$\left(\frac{U}{u_\tau}\right)_s - \left(\frac{U}{u_\tau}\right)_r = \frac{\Delta U}{u_\tau} = \frac{1}{k}\ln\frac{u_\tau k_e}{\nu} + C - B_1 \qquad (10)$$

Figure 28 from reference 22, presents data over a significant range of $(u_\tau k_e)/\nu$ for several types of roughness (ref. 25). The data distribution indicates that $\Delta U/u_\tau$ is not a universal function of $(u_\tau k_e)/\nu$ and that for large values of $(u_\tau k_e)/\nu$ the slope of the straight lines is equal to $1/k$, where k is 0.41. However, the value of $C - B_1$ may still differ for the various types of roughness.

Figures 29 and 30 present the data initially presented in figures 25 and 26, respectively, in addition to curves calculated using equation (8). Equation (8) fits these data by assuming the value of the constant B_1 to be 8.5 and the effective

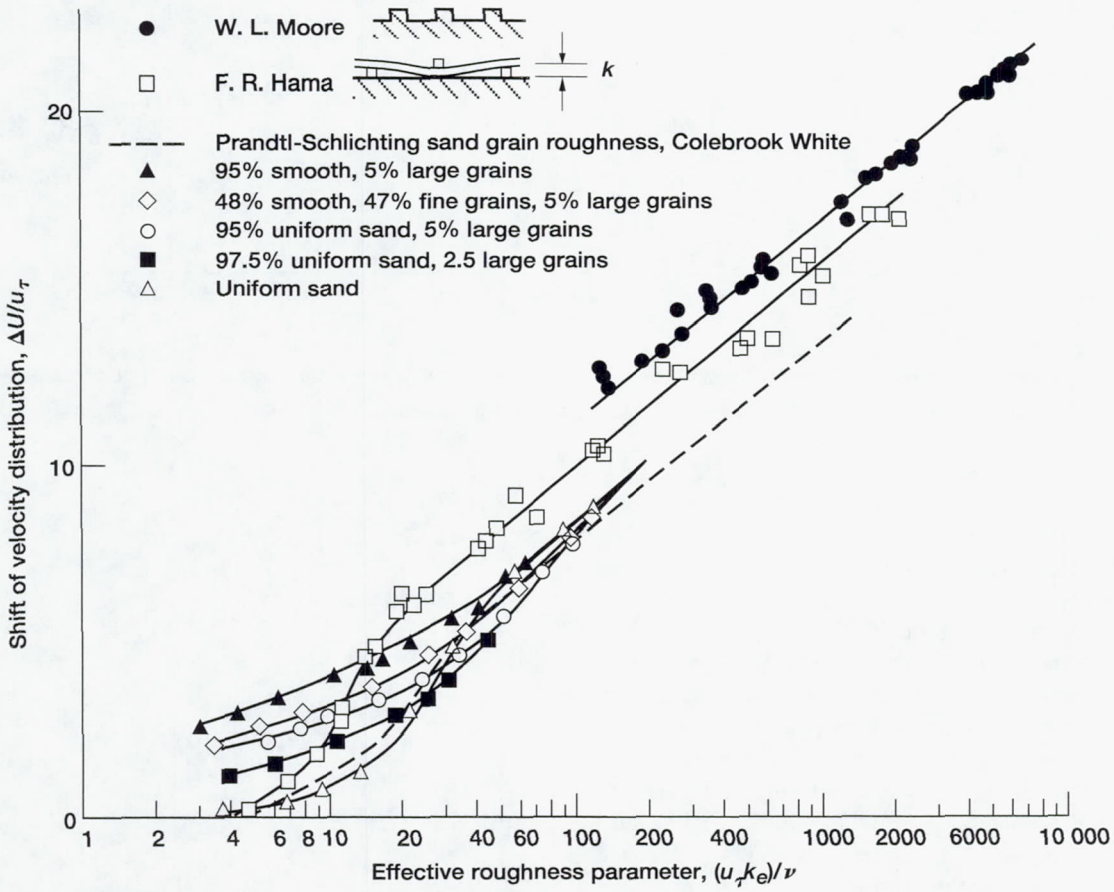

Figure 28.—Effect of wall roughness on the shift $\Delta U/u_\tau$ of the velocity-distribution profile (from ref. 25).

roughness k_e to be 0.31 and 0.61 cm in figures 29 and 30, respectively. Note that 0.31 cm, the magnitude of the effective roughness k_e assumed in figure 29, is coincidently equal to the peak-to-peak displacement of the oscillating vane (0.318 cm) and that the vane trailing edge is located 0.48 cm upstream. Because the application of equation (8) to the data presented in figures 29 and 30 infers a possible explanation for the departure of the data from the wall-wake equation at large values of y^+, the above analyses were applied to the remaining measured velocity profile data displaying this behavior at L of 5.72 and 9.52 cm downstream from the oscillating vane trailing edge. These data are presented in figures 31 and 32, respectively. For the data presented in figures 29 through 32, the effective roughness parameter $(u_\tau k_e)/\nu$ varied from approximately 63 to 111, which is assumed here to indicate that effectively a fully rough-wall condition existed over the ramp surface from the vane trailing edge to at least a point halfway down the ramp. Thus, the buffer layer is being extended toward the surface with no effective viscous layer.

Like figure 28, figure 33 presents the measured data as a function of the shift of the velocity distribution $\Delta U/u_\tau$ and the effective roughness parameter $(u_\tau k_e)/\nu$. In comparison with the data presented in figure 28, which represent a significant range of roughness types, the data obtained here align very closely with the data labeled Prandtl-Schlichting sand grain roughness.

In summary, the measured velocity profile data presented in figures 29 through 32 demonstrate that at increased surface distance from the vane trailing edge, the wall-wake prediction is attained at continually larger values of y^+. Finally, the observation can be made that the oscillating vane is acting to produce an effective roughness, which primarily enlarges the width of the buffer layer and effectively eliminates the viscous sublayer. The viscous sublayer is effectively eliminated because the periodically formed starting vortices and secondary vortices that attach themselves to the ramp surface and move downstream act as obstacles or roughness to the remaining fluid in the near wall region of the boundary layer. This finding suggests an explanation for the anomaly noted in the previous Pressure Recovery section of this report. It was noted that from a point 2 cm downstream of the oscillating vane trailing edge to the ramp exit, increases in the local surface static pressure coefficient were independent of increases in the vane displacement amplitude h above 0.318 cm, whereas below this amplitude the local pressure coefficient varied as a function of both the vane oscillation frequency and

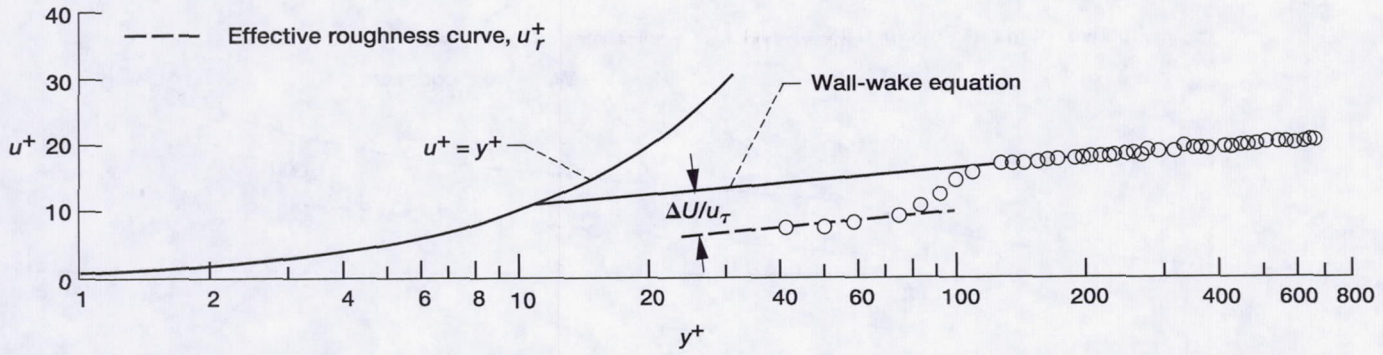

Figure 29.—Velocity profile in inner wall coordinates at L of 0.48 cm downstream from vane trailing edge; inlet velocity, U_1, 6.6 m/sec; excitation frequency, f, 30 Hz; vane peak-to-peak displacement, h, 0.318 cm. Influence of effective roughness on sublayer is shown.

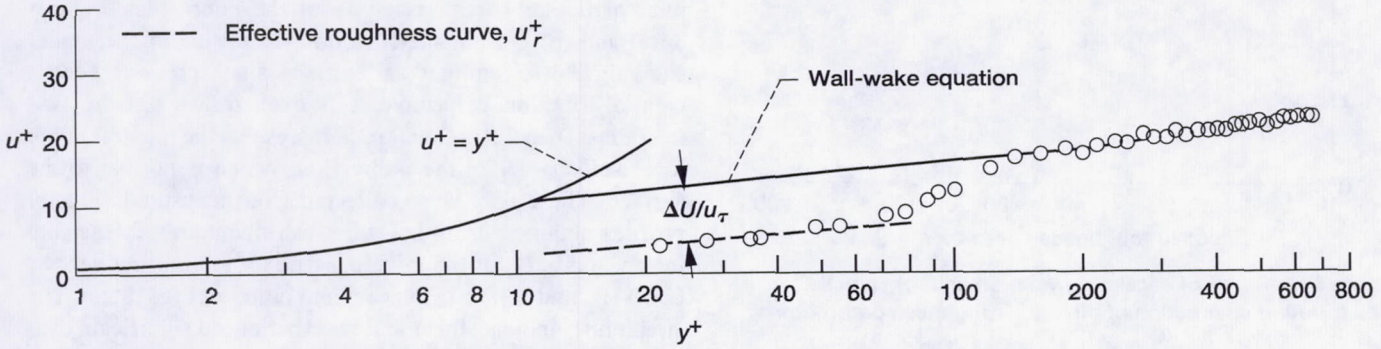

Figure 30.—Velocity profile in inner wall coordinates at L of 1.90 cm downstream from vane trailing edge; inlet velocity, U_1, 6.6 m/sec; excitation frequency, f, 30 Hz; vane peak-to-peak displacement, h, 0.318 cm. Influence of effective roughness on sublayer is shown.

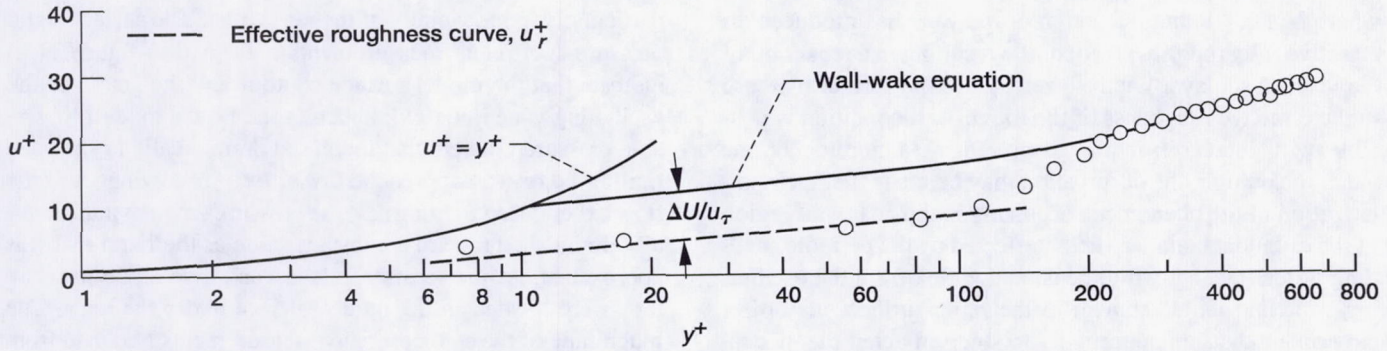

Figure 31.—Velocity profile in inner wall coordinates at L of 5.72 cm downstream from vane trailing edge; inlet velocity, U_1, 6.6 m/sec; excitation frequency, f, 30 Hz; vane peak-to-peak displacement, h, 0.318 cm. Influence of effective roughness on sublayer is shown.

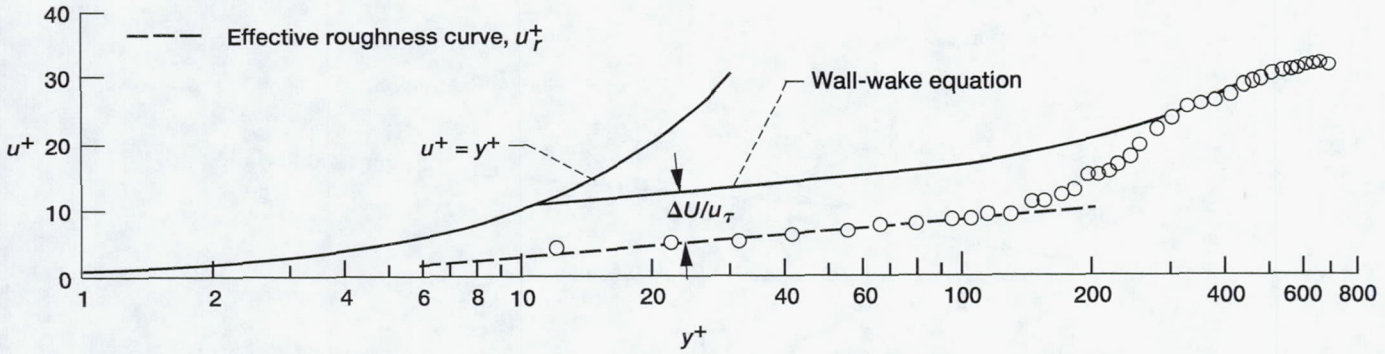

Figure 32.—Velocity profile in inner wall coordinates at L of 9.52 cm downstream from vane trailing edge; inlet velocity, U_1, 6.6 m/sec; excitation frequency, f, 30 Hz; vane peak-to-peak displacement, h, 0.318 cm. Influence of effective roughness on sublayer is shown.

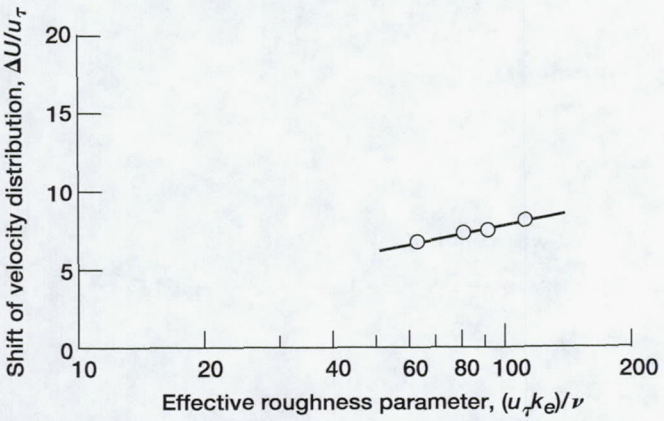

Figure 33.—Effect of oscillating vane on shift of velocity distribution as function of effective roughness parameter.

its displacement amplitude. This limit in the effectiveness of the vane displacement amplitude may be attributed to the effective roughness produced by the vane action as demonstrated in figures 29 through 32. In these figures, an increase in the vane displacement amplitude h to 0.318 cm is shown to enlarge the width of the buffer layer and reduce the thickness of the viscous sublayer. More specifically, in the limiting case where h is 0.318 cm, the action of the vane has produced an effective fully rough-wall condition resulting in a reduction of the viscous sublayer width to zero. Thus, no further increase in the effective roughness of the rough-wall condition is possible with increases in the displacement amplitude of the vane. In addition, the observation may be made that the regularization of the phenomena occurring in the near wall region of the turbulent boundary layer, effected by the periodic shedding of the starting two-dimensional vortex from the oscillating vane and its attachment to the ramp surface, may offer experimentalists an opportunity to study in detail the mechanisms that occur in buffer layers. Such mechanisms are important to the understanding of turbulent boundary layer attachment.

Effect of streamline curvature.—As evident from the discussion of the measured data thus far, the oscillating vane has turned the flow through a sufficiently large angle at the entrance to the ramp to delay detachment there. This implies that the mean flow streamlines must have significant curvature, particularly in the vicinity of the ramp inlet. Figures 34(a) and (b) present sketches drawn to scale of the model showing the streamlines and surface static pressure coefficient distribution, respectively, for excited flow passing over the ramp. The stream function Ψ represents the integral of the local velocity U_L in the y-direction, which is normal to the surface. These data were collected from measured velocity profiles obtained using hot-wire instrumentation for a ramp inlet velocity U_1 of 6.6 m/sec, a vane oscillating frequency f of 30 Hz, and a vane displacement height h of 0.318 cm. The streamlines indicate that the flow experienced significant concave and convex curvature effects. Between a point 2.5 cm upstream of the vane and its leading edge, these data show that the flow decelerated with a corresponding convex bend of the streamlines. Downstream from the vane trailing edge, the flow in the inner and midregions of the boundary layer decelerated whereas the outer region underwent an undulation and experienced an acceleration-deceleration cycle. These data show the large changes in streamline curvature that were necessary to turn the bounded flow through 20° of deflection, particularly in the vicinity of the ramp inlet. The surface static pressure coefficient measurements presented in figure 34(b) indicate that the model surface contour and the action of the oscillating vane initially induced in the flow a modest, favorable pressure gradient that increased dramatically as the vane trailing edge was approached. Abruptly following that, the flow experienced a strong adverse pressure gradient that gradually diminished toward a constant value as the ramp exit was approached. At the location of the vane, two static pressure taps were located in the model surface under the vane. The magnitude of the static pressure measurements obtained from these taps during the vane actuation is questionable; therefore, the curve representing their surface static pressure coefficients is drawn as a dashed line.

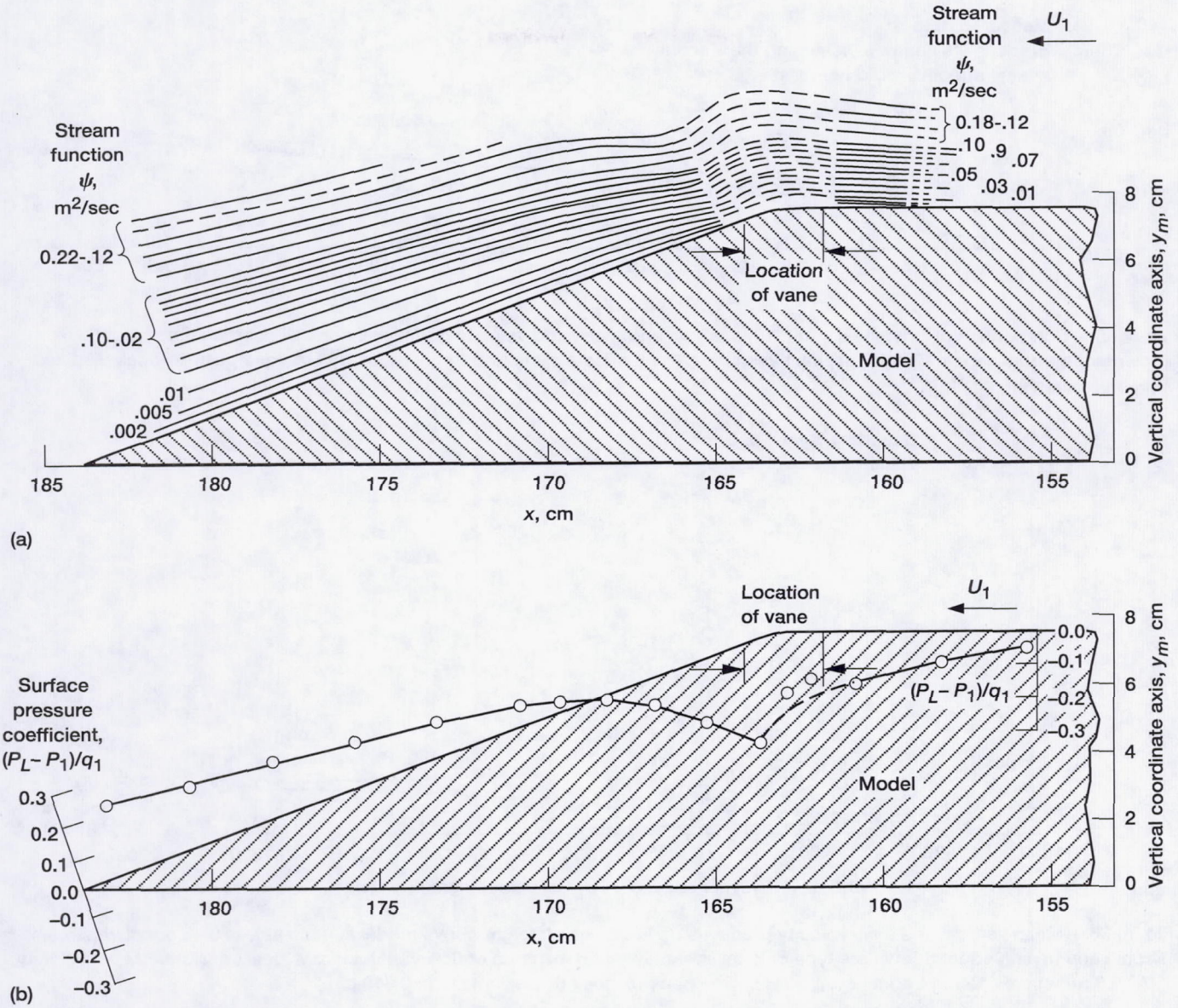

Figure 34.—Stream function contours and surface static pressure coefficient distribution for excited flow passing over 20° rearward-facing ramp; constant ramp inlet velocity, U_1, 6.6 m/sec; excitation frequency, f, 30 Hz; vane peak-to-peak displacement, h, 0.318 cm. (a) Stream function contours. (b) Surface static pressure coefficient distribution.

In an effort to learn more about the effects of the flow streamline curvature on the turbulent structure of the boundary layer in the vicinity of the ramp inlet for the case of excited flow, there follows an application of Bradshaw's (ref. 15) analysis to the measured velocity profile data.

Bradshaw considered the effects of streamline curvature on turbulent flow, indicating that large effects are exerted on shear flow turbulence by the curvature of streamlines in the plane of the mean shear. He discusses a technique involving explicit empirical allowance for higher order parameters of the turbulence structure. By applying the technique to the turbulent boundary layer produced by flow passing over the inlet of a rearward-facing 20° ramp experiencing excitation, we have an opportunity to gain insight into the unique effects produced by excitation on its turbulence structure.

As discussed in appendix A, Bradshaw (ref. 15) considered from a critical standpoint the standard explanation of how flow behaves as it passes over a curved surface; that is, centrifugal forces are balanced by pressure forces. He presents a different way of thinking about this concept by postulating the existence of thin shear layers of high-Reynolds-stress fluid that can, if large enough, force change in the mean flow motion of bounded shear flows. His model then requires that large Reynolds stress gradients be produced to overcome the

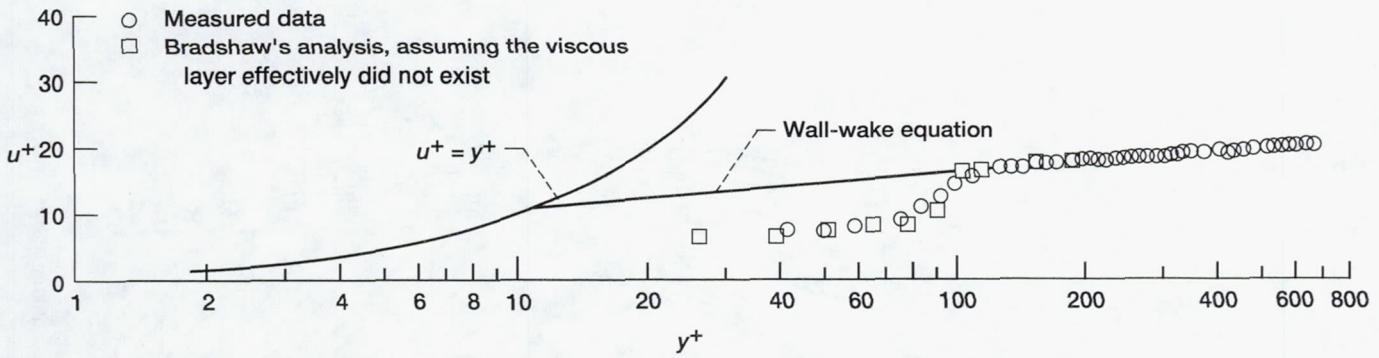

Figure 35.—Comparison of Bradshaw's (ref. 15) analysis and measured velocity profile in inner wall coordinates at L of 0.48 cm downstream from vane trailing edge; inlet velocity, U_1, 6.6 m/sec; excitation frequency, f, 30 Hz; vane peak-to-peak displacement, h, 0.318 cm.

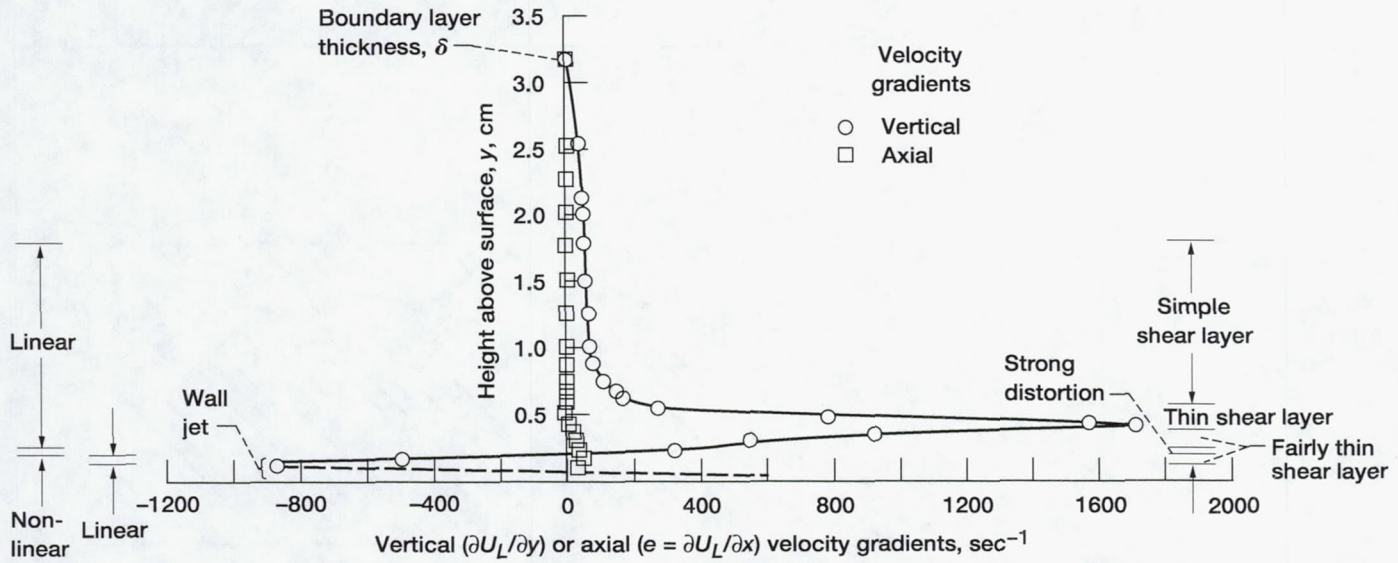

Figure 36.—Mean vertical and axial velocity gradients as functions of height above model surface at L of 0.48 cm downstream from vane trailing edge. Shown are type of local shear layer and measure of flow variation from local equilibrium; inlet velocity, U_1, 6.6 m/sec; excitation frequency, f, 30 Hz; vane peak-to-peak displacement, h, 0.318 cm.

large mean flow strain rates distributed over a curved surface required to maintain attached flow. Thus, he proposes the existence of thin shear layers within boundary layers in which strong turbulence generation can produce changes in the turbulence structure sufficient to change the mean flow velocity profiles. In the experiment reported here, the action of the vane produced attachment of an otherwise detached boundary layer by increasing the production of the turbulent kinetic energy and Reynolds shearing stresses in the inner wall region, as shown in figures 17(b) and 19, respectively.

Figure 35 presents a comparison of Bradshaw's analysis (ref. 15), using equation (A13) from appendix A, and the measured velocity profile data in inner wall coordinates at L of 0.48 cm downstream of the vane trailing edge. The comparison shows good agreement, particularly in the transition region from y^+ of 80 to 110. From appendix A, equation (A13) is

$$\frac{U_L}{u_\tau} = \frac{1}{k}\ln\frac{u_\tau y}{\nu} + \frac{\alpha e y_0}{u_\tau} - \frac{\alpha e y}{u_\tau} + C$$

where α is a factor of order 10 (eq. (A8)), e is a small extra rate of strain, and $y_0 = \nu/u_\tau$, and C represents a measure of the change in the dimensionless velocity across the viscous sublayer. The calculations were made assuming that the value of the constant C in equation (A13) was zero. Thus it was assumed that the viscous sublayer effectively did not exist. Figure 36 presents the mean vertical $\partial U_L/\partial y$ and mean axial $e = \partial U_L/\partial x$ velocity gradients calculated from smoothed velocity profile data at L of 0.48 cm downstream from the vane trailing edge and from crossplots of mean axial velocity profiles measured along the surface of the model, respectively. In the table of appendix A, these two velocity gradients are used by Bradshaw to classify the local shear layer of the boundary

layer into thin layers that are known experimentally to exhibit varying degrees of turbulence generation and that, in turn, can produce changes in the turbulence structure sufficient to change the mean flow velocity profile. The type of local shear layer shown was determined by using the order-of-magnitude criteria presented in the table of appendix A. In addition, the types of local shear layers and a measure of the flow variation from local equilibrium, expressed as a function of its linearity, are presented on the right- and left-hand sides, respectively, of figure 36. The labels "linear" and "nonlinear" are based on an evaluation of the linear correction factor F, which is discussed in appendix A and is a measure of the flow variation from local equilibrium. The term linear as used in figure 36 means that the value of the F-factor $1 + [\alpha e/(\partial U/\partial y)]$ (in eq. (A8)) lies between 0.5 and 1.5, which represent the largest departures from unity that can be tolerated, according to Bradshaw (ref. 15), and still keep the small assumed extra rate of strain e within 5 percent of the local mean flow rate of strain $\partial U_1/\partial y$. Thus, these data indicate that the analysis should be valid from y's of 0.13 to 0.19 cm and from 0.254 to 1.78 cm. Note that the layers labeled as "fairly thin shear layer" run from y's of 0.13 to 0.19 cm and from 0.245 to 0.38 cm. These layers are located in the same region where the detached vortex is located just after it is released from the oscillating vane as the vane starts to retract from its maximum displacement height of 0.318 cm. This is significant, as noted in the table of appendix A, because within such layers the Reynolds stress gradients are predicted by the analysis to be significant. Thus, the local generation of turbulence is large and can bring about a change in the turbulence structure of the shear layer. This then is the mechanism that causes a change in the mean flow motion. At L of 1.9 cm downstream from the vane and at a dimensionless height y/δ above the surface of 0.09 (corresponding to y of 0.28 cm above the surface), figures 17(b) and 19 indicate that the normal shear stress and the Reynolds shear stress gradients, respectively, are large. Hence, the oscillating vane is creating significant local generation of turbulence, which causes a change in the turbulence structure of the shear layer and a consequent change in the mean flow motion.

Effect of wall jet.—The mean velocity profile measured at L of 0.48 cm downstream from the vane for the excited case and presented in figure 14 indicates that a wall jet is located in the near wall region below a height of 0.05δ. An important aspect of this wall jet is indicated in figure 36 by the curves representing the mean flow velocity gradients near the wall. From y's of 0.13 to 0.19 cm above the surface, a fairly thin shear layer is noted to exist. A dashed curve drawn below a height y of 0.127 cm represents a hypothetical variation of the vertical mean flow velocity gradient in the near wall region of the boundary layer. This curve is hypothetical because it was not possible to determine the velocity gradients below 0.127 cm. However, with reference to figure 14, it is evident that for a y/δ below 0.02, the vertical mean flow velocity gradient must change sign as the mean velocity approaches zero at the model surface. This indicates that the sign of the velocity gradient near the surface must be positive, which implies that other fairly thin shear layers exist very close to the surface. The existence of such layers highlights the significance of a wall jet as part of the mechanism that contributes to a change in the mean flow motion, and in this specific case, the delay in detachment of an excited boundary layer. In addition, the existence of these layers in the very near wall region of the boundary layer helps to explain the observation made at the end of the Pressure Recovery section: it was essential for the vane to close completely down on the model surface to produce the maximum static pressure recovery.

In summary, it is proposed that the wall jet and the fully rough-wall condition of the mean flow velocity profiles along the upper half of the ramp surface are manifestations of the oscillating vane periodic formation of the spanwise two-dimensional starting vortices that attached themselves to the ramp surface. These vortices thereby acted as the principal mechanism that produced the delay in detachment of the turbulent boundary layer as a function of the vane oscillation frequency and a limited range of its displacement amplitude.

Results Downstream From Vane and in Logarithmic-Law Region and Outer Layer of Boundary Layer

In this section the discussion of the flow field will consider the phenomena occurring downstream of the vane and above the ramp surface in the log-law region and the outer layer of the boundary layer. As previously discussed, the phenomena occurring in the vicinity of the vane are very complex and have been only revealed through the combined use of hot wires and smoke-wire flow visualization techniques. The use of these two techniques is essential because they compliment each other. That is, hot wires are ideal for determining the statistical properties of turbulent flow; however, they are much less satisfactory for revealing the existence of organized flow structures that may vary widely in size and orientation. This, however, is just the information that can be obtained from flow visualization studies. Thus, these two techniques will continue to be used in the study of events occurring downstream from the vane and extending to the exit from the 20° ramp.

Strongly interactive events and three dimensionality.—Figure 37 presents a sequence of motion picture frames of smoke streaklines representing the evolution of what are believed to be counter-rotating spanwise vortices produced during one operating cycle of the oscillating vane. The smoke wire is located at L of 1.90 cm downstream of the vane and laterally 11.43 cm from the vertical plane passing through the centerline of the wind tunnel. The spanwise location off the model centerline was chosen to eliminate the remote possibility of capturing erroneous effects caused by the three, small, final flexible links in the vane drive train (as discussed in the

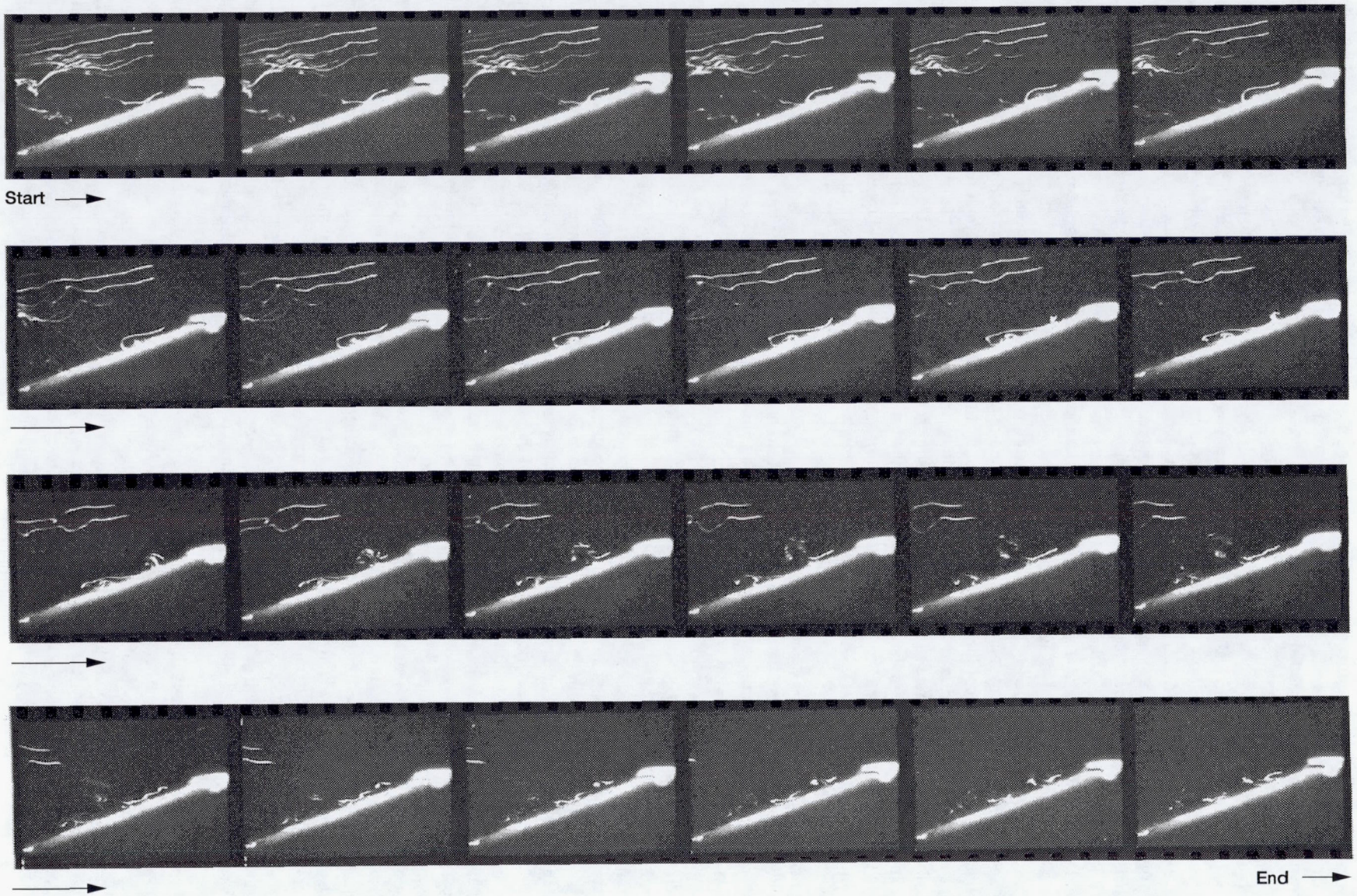

Figure 37.—Smoke-wire motion picture sequence of dynamic interaction between two spanwise vortices produced by oscillating vane operating at 25 Hz. Flow is moving from right to left; each frame represents a 0.0025-sec time step; inlet velocity, U_1, 2.6 m/sec; vane peak-to-peak displacement, h, 0.318 cm; smoke wire at L of 1.90 cm downstream from vane trailing edge.

Apparatus and Instrumentation section). Measured from the smoke wire the streamwise extent of the view in each frame includes approximately 12 cm of the ramp surface. The sequence begins with the vane approaching its maximum displacement height, continues through the retraction portion of its cycle where its trailing edge closes completely down on the ramp surface, and finally reaches its maximum displacement height again. Note that a spanwise starting vortex becomes visible along the surface and remains attached to the wall layer as it is convected downstream. Midway through the cycle, a lifting line vortex is released from the vane as it starts to retract. The lifting line vortex is spacially located above the surface, remains detached, appears to dynamically interact with the starting vortex while being convected downstream, and rises up into the boundary layer during a period of 5/400 sec. As this occurs, the smoke identifying this event is diluted. The axial location at which it starts to rise is between 3 and 4 cm downstream from the vane; at this point in the cycle, the downstream vortex, which is attached to the wall layer, is located approximately 6 cm from the vane. Figure 38 presents a series of enlarged photographs of frames from figure 37, beginning with the fourth frame in the second row from the start. These photographs show in greater detail the development with time of the two primary vortices. Notice that in figure 38(b) an induced secondary vortex develops on the downstream side of the originally formed starting vortex, which remains attached to the wall layer as it is being convected downstream. The other primary vortex, the lifting line vortex, is detached from the wall layer. As it rises, its trajectory tilts toward the downstream direction. The streakline image looks somewhat like a hairpin with legs extending into the wall layer.

For the cases in which the vane trailing edge did not close down completely on the surface (see fig. 8), the motion picture data obtained in this study, but not presented, reveal that the starting vortex did not attach to the surface of the ramp. Consequently, the two spanwise vortices interacted dynamically above the surface while being convected downstream and produced significantly lower levels of static pressure recovery, as noted in figure 8.

Figures 39(a) and (b) present essentially the same sequence and view of the vortex evolutionary events as those in figure 37 but include streaklines showing the evolution of the upper flow field. In these sequences, the smoke wire is located at L of 0.318 and 1.90 cm, respectively, downstream from the vane trailing edge, which in the case of figure 39(a) is closer to the vane than it was in figure 37. In both figures, the smoke wire is located 11.43 cm from a vertical plane passing through the centerline of the wind tunnel. Measured from the smoke wire, the view in each frame of figures 39(a) and (b) extends over a streamwise length of approximately 5 and 9 cm, respectively. These figures are presented because figure 39(a) provides a telephoto view of the vortical interaction and 39(b) presents a broader view showing more of the downstream evolution of the interaction with the outer inviscid flow. In figure 39(a), the sequence begins with the vane (over exposed) rising off the surface and proceeding to its full displacement height. The starting vortex develops on the wall layer and remains attached as it is convected along the surface. Beginning with the second row, the lifting line vortex (upstream vortex) is released from the vane as it starts to retract. Note that the streaklines well above the vortex show a distinct and almost immediate distention and kinking in response to this vortex as it rises and spacially grows while being convected downstream. During this process, the downstream starting vortex, attached to the wall layer, develops a secondary vortex and has thickened. Note that the streaklines above and around the two vortices evolve in time (as shown in the third and fourth rows) and develop hairpin shapes having large slopes, even negative slopes, on their downstream sides. The sequence presented in figure 39(b) begins with the vane (overexposed) retracting toward the surface and the starting vortex just arriving at the smoke wire, which is located farther downstream than in figure 39(a). Beginning with the second row, the lifting line vortex has arrived at the smoke wire. Note the evolution of the streaklines above and between these two vortices as the vane proceeds through one complete cycle as shown in the third and fourth rows. A well-differentiated, V-shaped envelope of streaklines (pitched downstream) develops within which small hairpin shapes appear. The sides of these structures have large gradients from which it can be inferred that locally large vertical flows are present.

The unsteady boundary layers induced by the motion of two-dimensional rectilinear vortex pairs and three-dimensional vortex loops in an otherwise stagnant fluid above a plane wall were studied in reference 26. Reference 26 also discussed the development of the instantaneous streamwise velocity profiles expected from flow fields containing such structures and indicates that these structures produce a region of retarded flow, which thickens rapidly. As upstream fluid arrives near these structures, it is forced to flow over and around the rapidly thickening zone of retarded flow. Thus, the instantaneous streamwise velocity profiles in these regions would be expected to develop into one similar to that sketched in figure 40(a), taken from reference 26. Figure 40(b) represents the instantaneous streamwise vorticity profile associated with the velocity profile. In this profile, a condition of zero shear is approached at some location above the wall. It may be inferred that as a point of zero shear develops in such a profile, it must be accompanied by a point of inflection in a velocity profile in which the streamwise velocity is everywhere positive. Streamwise instantaneous velocity profiles of the type shown in figure 40(a) have been observed by Blackwelder and Swearingen (ref. 27) in turbulent boundary layer flows. Reference 26 indicates that Blackwelder (ref. 28) and Bippes (ref. 29) have frequently observed such velocity profiles immediately before a thickening viscous flow near a wall becomes strongly interactive with the outer inviscid flow (i.e.,

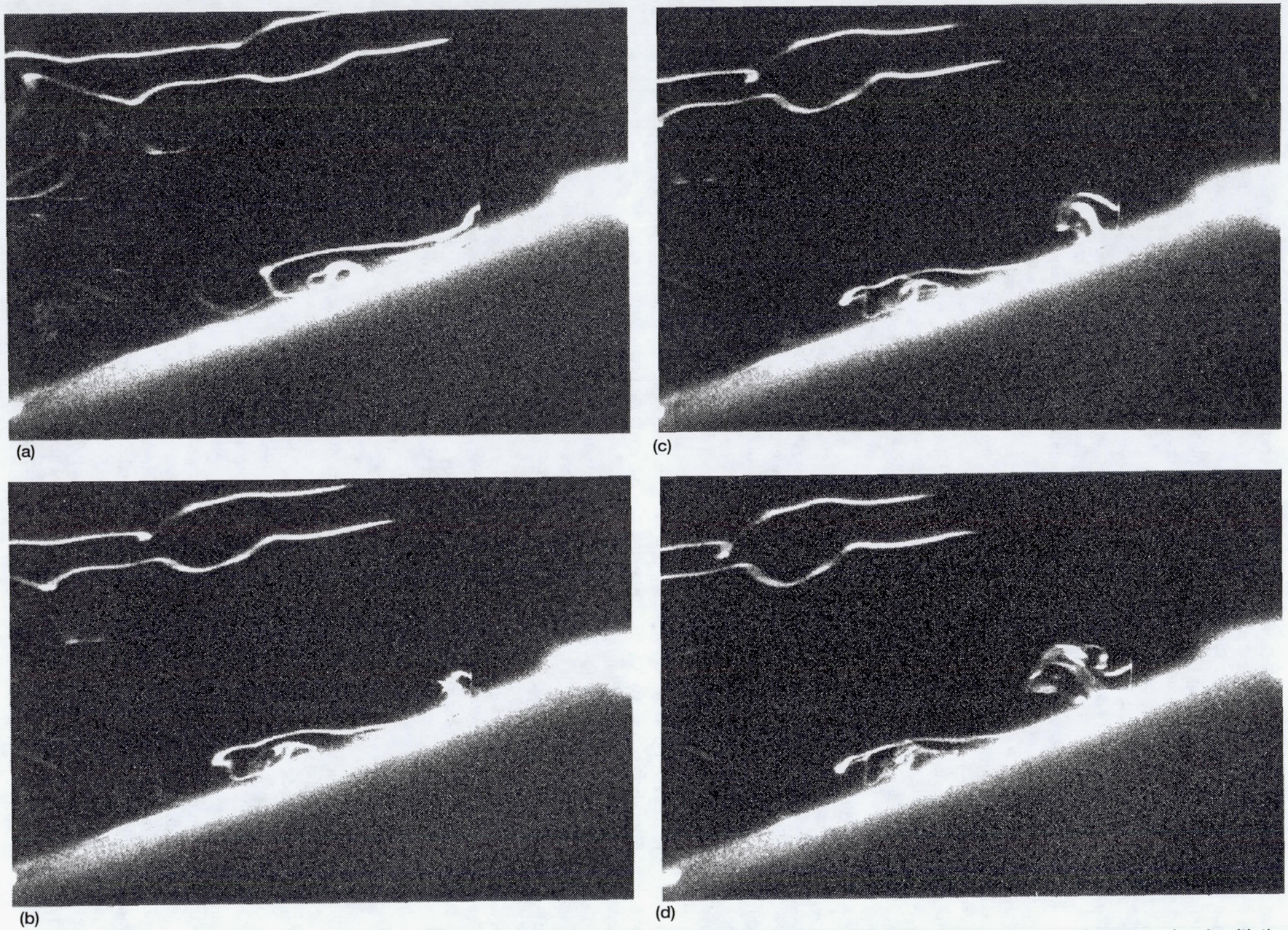

Figure 38.—Enlarged views of motion picture frames presented in figure 37. Sequence starts with the fourth frame in the second row from the start and ends with the sixth frame in the third row. Sequence shows the dynamic interaction between the two spanwise vortices and the mean mean flow produced by the oscillating vane. (a to b) Induced secondary vortex starts to develop from originally formed starting vortex attached to wall layer. (b to h) Detached lifting line vortex rises into outer boundary layer.

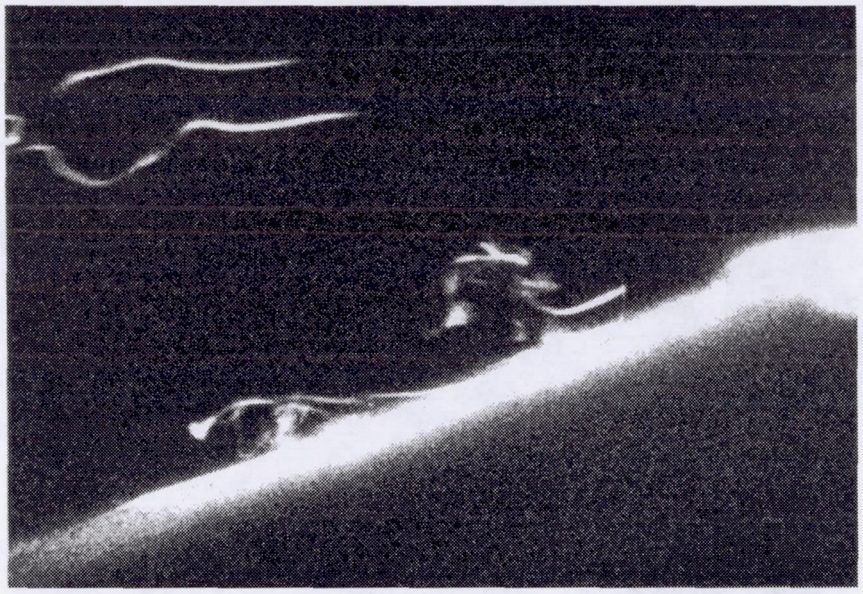

(e)

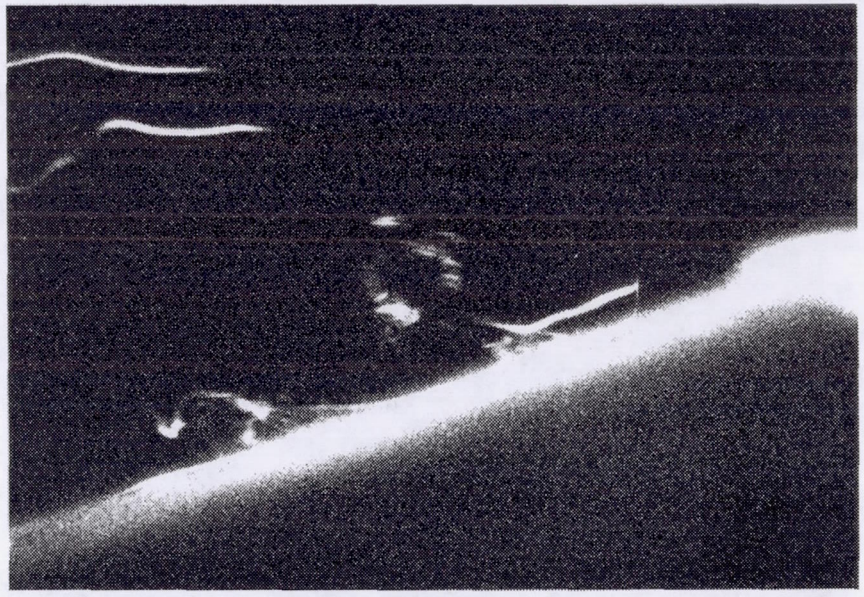

(g)

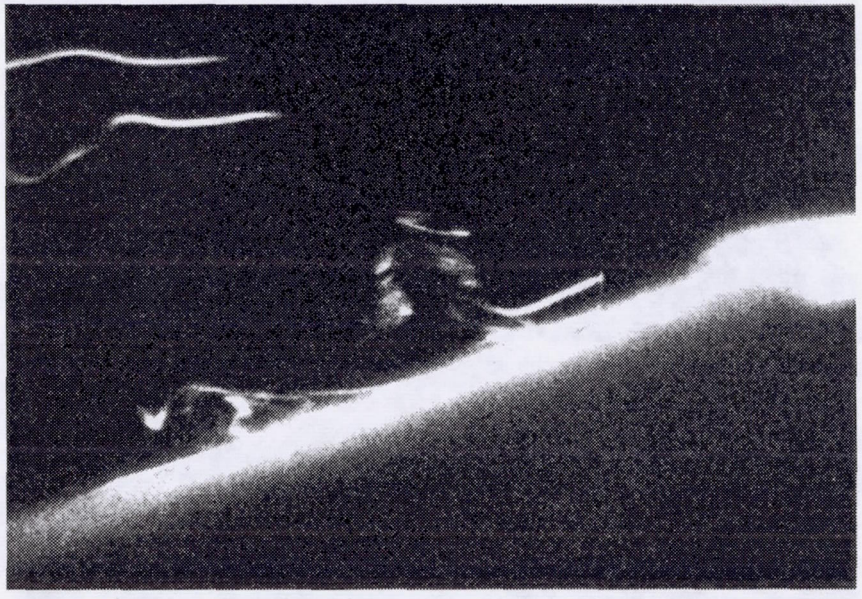

(f)

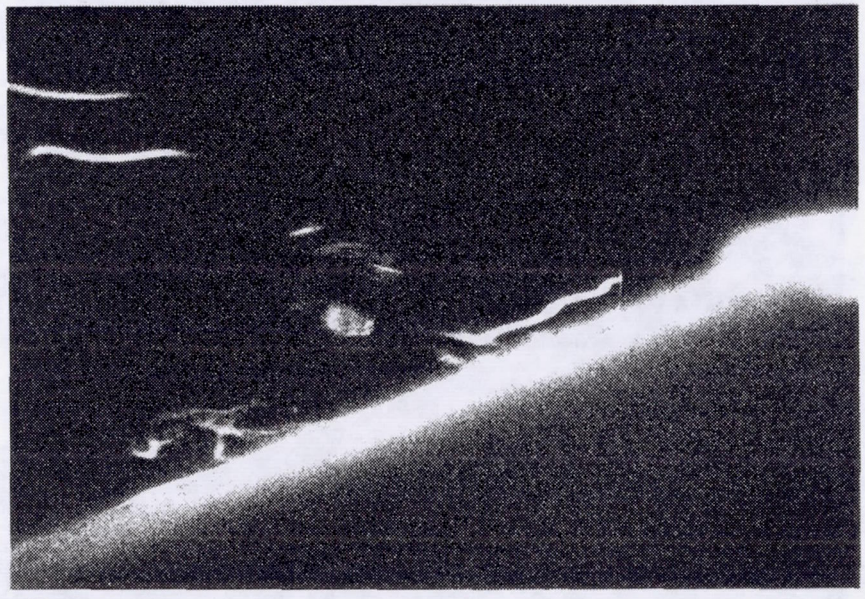

(h)

Figure 38.—Concluded. (e to h) Detached lifting line vortex rises into outer boundary layer.

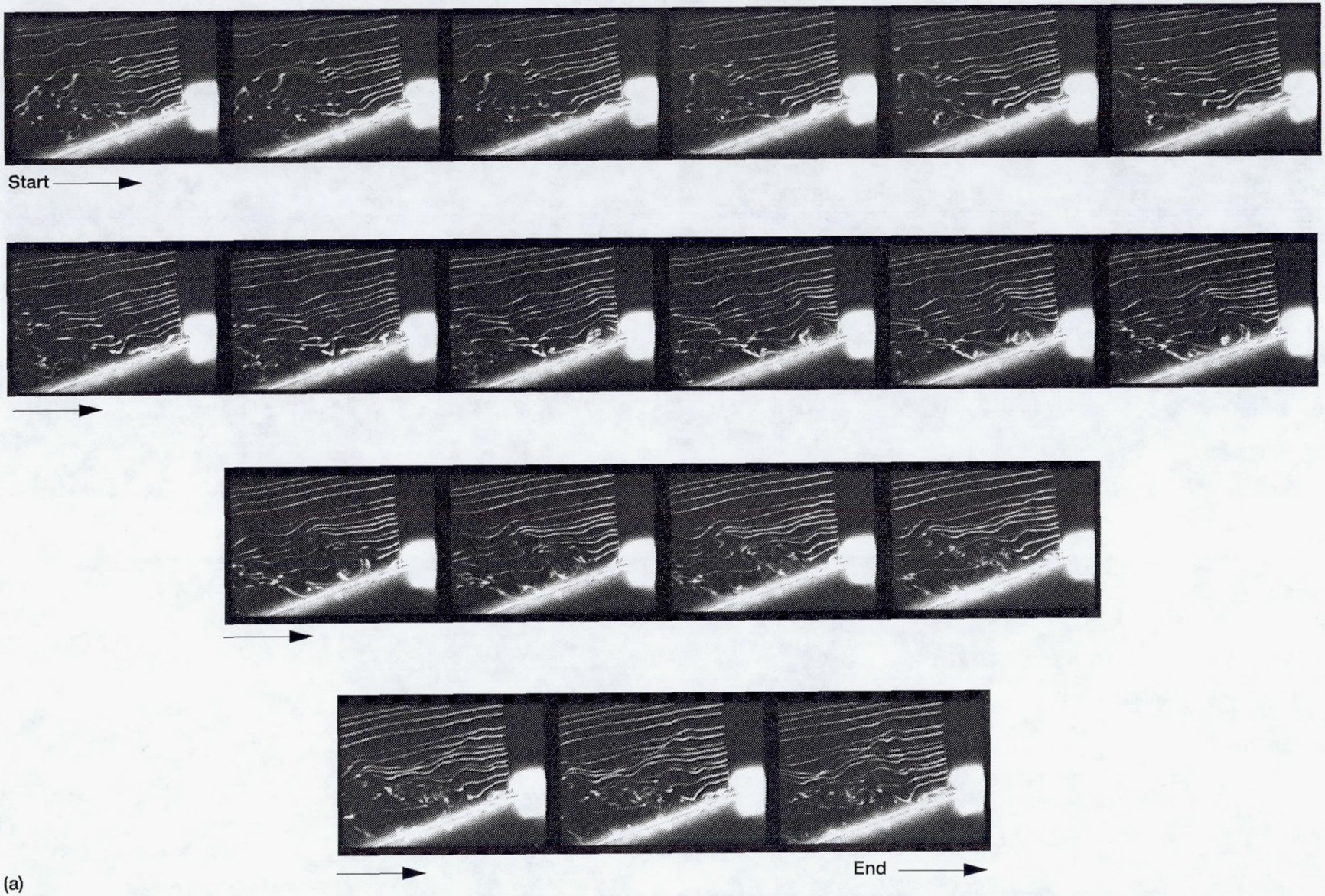

Figure 39.—Smoke-wire telephoto motion picture sequence of dynamic interaction between two spanwise vortices produced by oscillating vane operating at 25 Hz. Evolution of steaklines in upper flow field is shown. Flow is moving from right to left; each frame represents a 0.0025-sec time step; inlet velocity, U_1, 2.6 m/sec; vane peak-to-peak displacement, h, 0.318 cm. (a) Smoke wire located at L of 0.318 cm downstream from vane trailing edge. (b) Smoke wire located at L of 1.90 cm down stream from vane trailing edge.

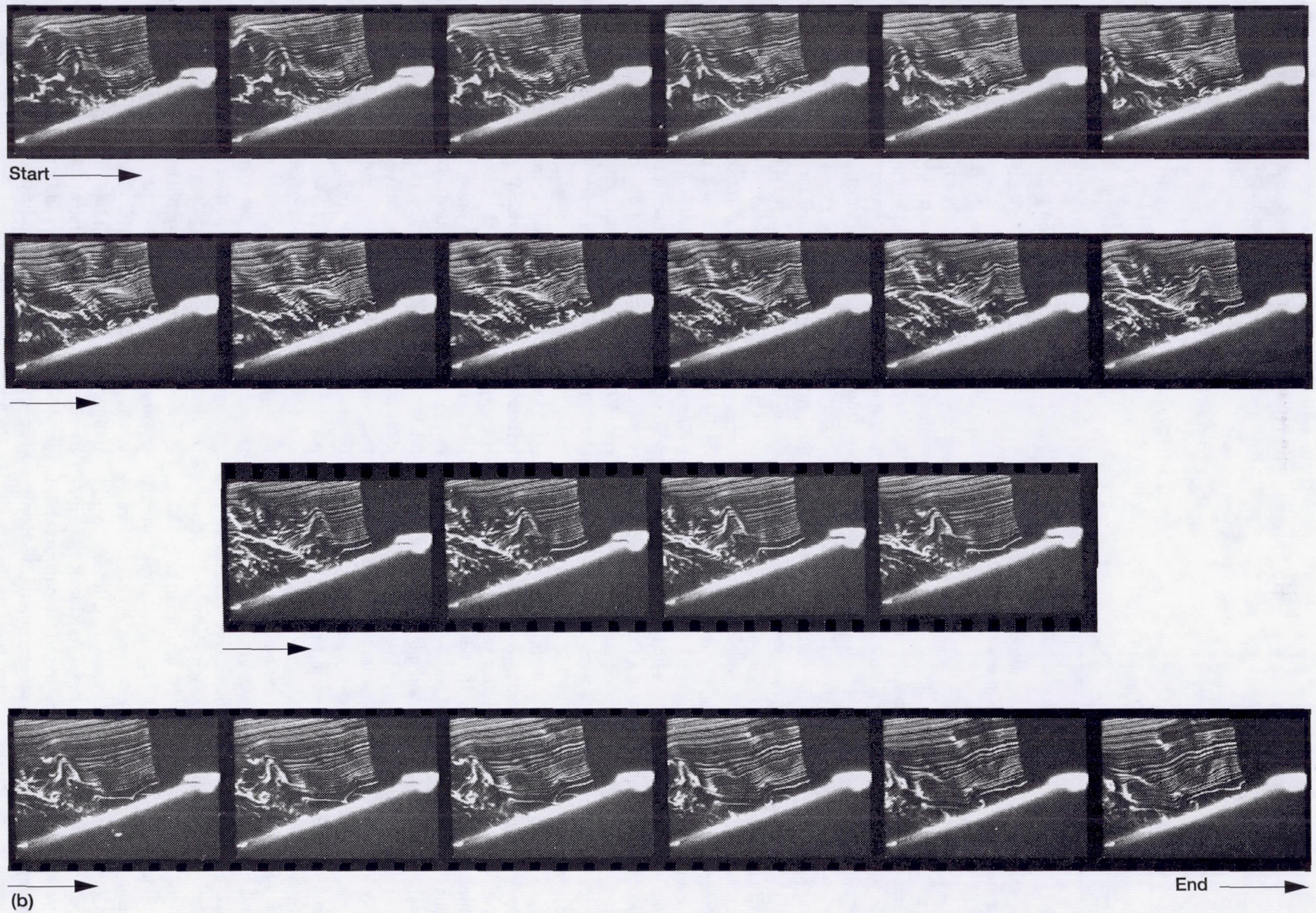

Figure 39.—Concluded. (b) Smoke wire located at L of 1.90 cm downstream from vane trailing edge.

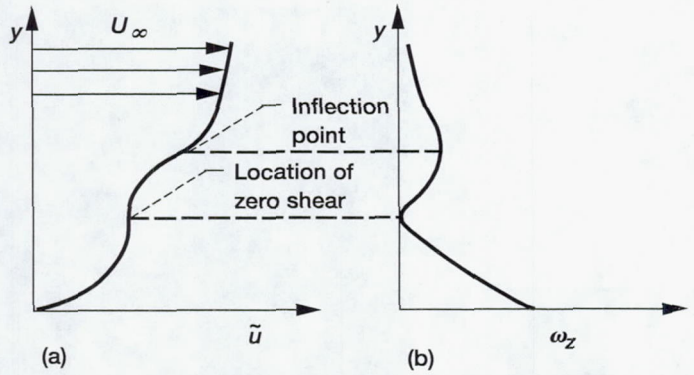

Figure 40.—Instantaneous streamwise velocity and vorticity profiles immediately preceding an interaction (ref. 26).

an ejection). It is pointed out here that the sequence of flow field events presented in the flow visualization figures 37 through 39 represent similar unstable, strongly interactive phenomena occurring between the vortical structures produced by the oscillating vane and the outer inviscid flow, although no instantaneous data were measured in the present study to varify it.

Figure 41 presents seven separate portrait photographs showing more clearly the details of the unstable, strongly interactive events in the boundary layer. The photographs were not from a motion picture sequence; they were taken as a random function of time and arranged in a sequence of events, using motion picture flow visualization data as a guide to provide a sense of the evolution of a typical eruptive event. The smoke wire is positioned at L of 1.90 cm downstream from the vane trailing edge and 10.70 cm laterally from a vertical plane passing through the centerline of the wind tunnel. Figure 41(a) represents a noninteractive, or initial quiescent, condition. Figure 41(b) appears to be similar to figure 38(e) in that a finger-shaped structure is rising or erupting into the outer region of the boundary layer. Figures 41(c) through (f) present a sequence showing the growth and convection of a T-shaped vortical structure that appears to be anchored to the inner wall layer and evolves into a mushroom and/or a sigma-shaped structure. The structure in figure 41(g) is believed to be a variation of that appearing in figures 41(c) through (f). This variation may be attributed to the unique time-dependent development of the two-dimensional spanwise vortical structures into three-dimensional vortical structures.

Reference 30 presents a visualization study of the flow behavior in the near wall region ($y^+ < 40$) of a turbulent boundary layer. Simultaneous top and end view photographs were obtained using hydrogen bubble wires and a dual-camera, high-speed video system. These data showed both the strong outward ejection and discrete streamwise rotation of fluid in the inner wall region. The study presented streamwise end views revealing a particularly clear sequence of the development of symmetric mushroom patterns from the near wall upwelling and revealed a counter-rotating pattern. Other imagery revealed the presence of both co-rotating and counter-rotating streamwise structures in proximity to each other.

In the present study, a consideration of the exact transport equation for the x-component of the mean vorticity,

$$U\frac{\partial \Omega_x}{\partial x} + V\frac{\partial \Omega_x}{\partial y} + W\frac{\partial \Omega_x}{\partial z} = \Omega_x\frac{\partial U}{\partial x} + \Omega_y\frac{\partial U}{\partial y} + \Omega_z\frac{\partial U}{\partial z} +$$

$$\left(\frac{\partial^2}{\partial y^2} - \frac{\partial^2}{\partial z^2}\right)\left(-\overline{vw}\right) + \frac{\partial\left(v^2 - w^2\right)}{\partial y \partial z} + \nu\nabla^2\Omega_x \qquad (11)$$

helps in the assertion that streamwise vorticity is being generated by the above-described dynamic events occurring in the vicinity of the oscillating vane trailing edge. The photographic data presented in figures 37 through 39 and 41 indicate that both spanwise z and vertical y components of a vortex exist in the flow field. In addition, mean velocity profile data presented in figures 14 and 17(a) indicate that significant mean flow shear $\partial U/\partial y$ exists. Thus, the second term on the right side of equation (11), $\Omega_y(\partial U/\partial y)$, is significant and represents an exchange of vorticity between components because the velocity gradient $\partial U/\partial y$ tilts or rotates a vortex that is initially in the y-direction so that it acquires a component in the x-direction. The first term, $\Omega_x(\partial U/\partial x)$, represents a stretching or compression of axial vortices if present.

Based on a consideration of the observations made in reference 30, the photographic data from the present study, and the above mathematical argument, the two spanwise vortices generated by the action of an oscillating vane dynamically interacted with each other in a unique way and, ultimately, strongly interacted with the outer inviscid flow. During this unstable, strongly interactive event, the ejection of vortical fluid resulted in the transfer of low-momentum fluid into the high-momentum region of the boundary layer. Such an interaction produced three dimensionality in the outer flow field and significantly increased its streamwise vorticity. In addition, this strongly interactive event produced a periodic disturbance that became intrinsic to the fluid. Thus, the original periodic two-dimensional disturbances produced by the vortices introduced into the inner region of the boundary layer by the action of the oscillating vane were changed by an unstable, strongly interactive event with the outer inviscid region to a controlled, periodic disturbance signal intrinsic to the fluid flow.

Developing three-dimensional region and turbulence generation.—Figure 42 is a portrait photograph taken with the smoke wire located at L of 10.2 cm downstream from the vane trailing edge and laterally 11.43 cm from the vertical plane passing through the centerline of the wind tunnel. The photograph shows several ribbons and single streaklines of smoke. The ribbons appear to indicate that the flow field has streamwise vortical components. Note that these rotating struc-

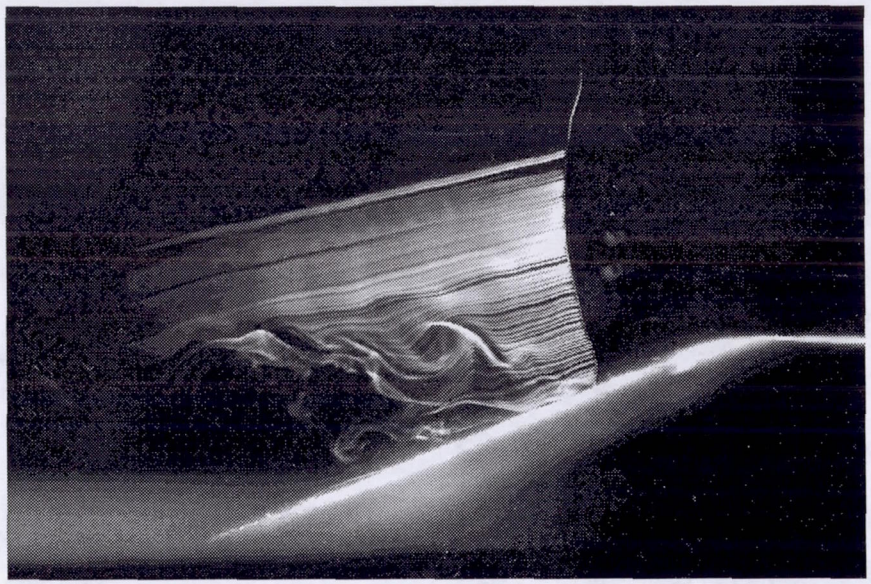

(a)

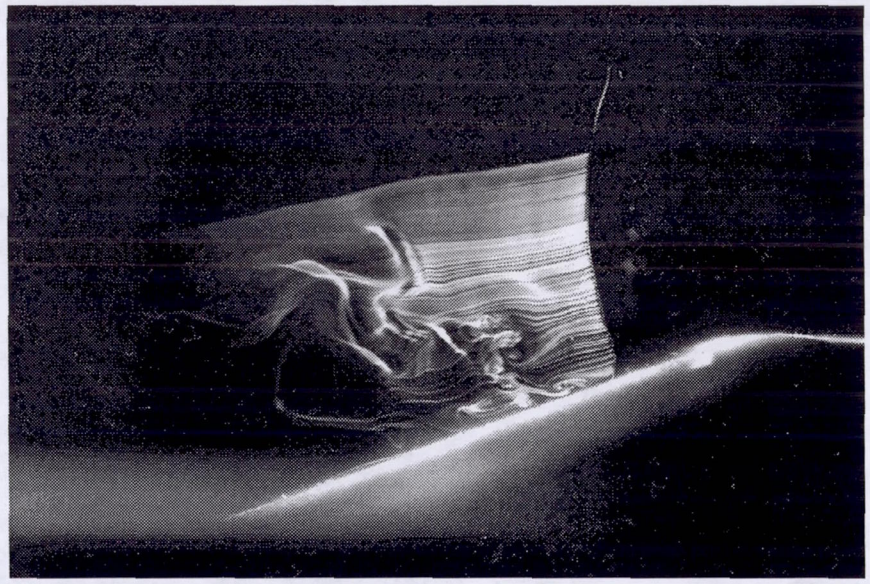

(c)

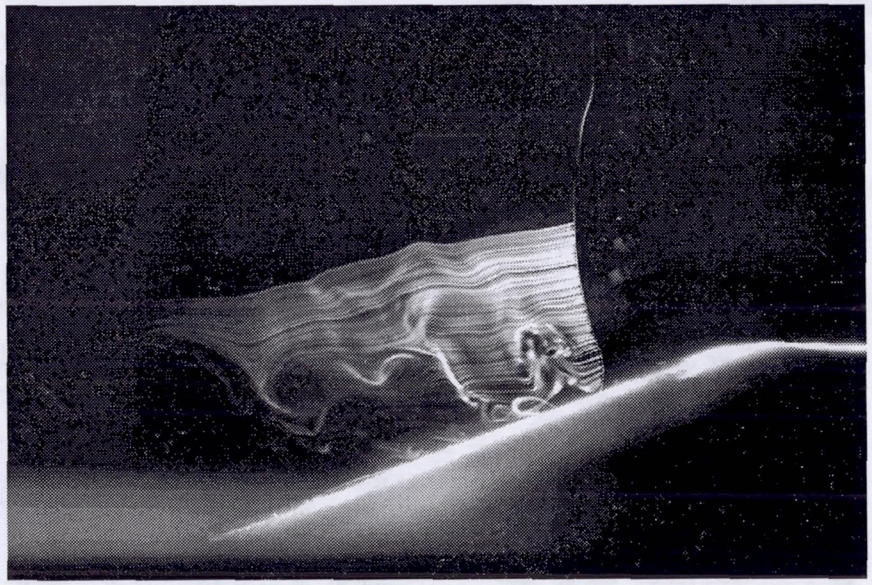

(b)

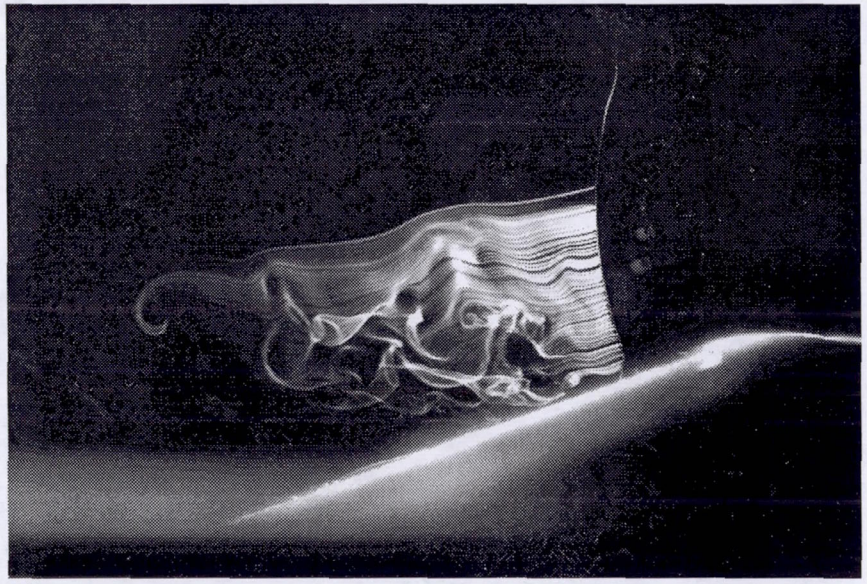

(d)

Figure 41.—Smoke-wire portrait photographs showing several views of unstable, strongly interactive events. Flow is moving from right to left; vane operation frequency, f, 25 Hz; inlet velocity, U_1, 2.6 m/sec; vane peak-to-peak displacement, h, 0.318 cm; smoke-wire located at L of 1.90 cm downstream from vane trailing edge. (a) Noninteractive (initial quiescent) condition. (b) Finger-shaped structure is erupting into outer region of boundary layer. (c to f) Growth and convection of T-shaped vortical structure shown. (g) Structure believed to be a variation of structures shown in parts (c) to (f).

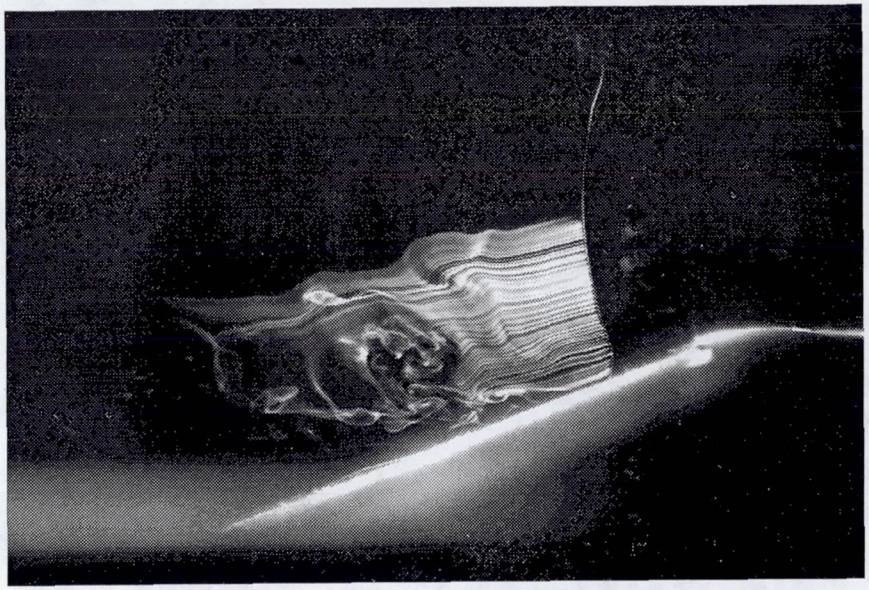

(e)

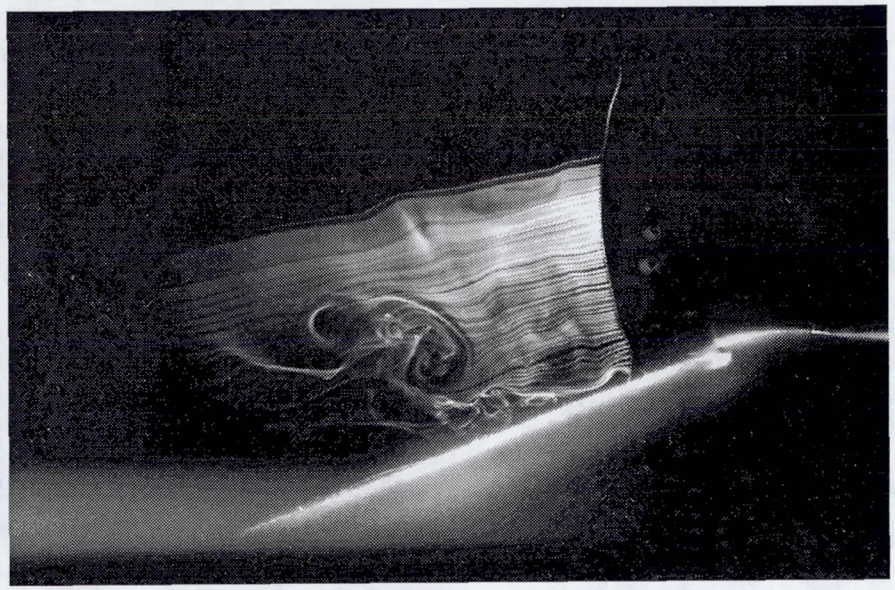

(f)

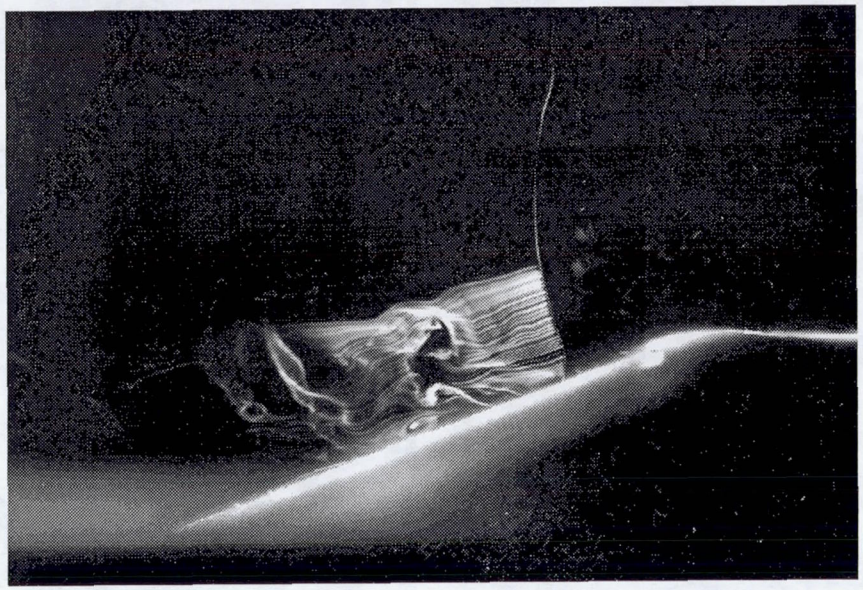

(g)

Figure 41.—Concluded. (e to f) Growth and convection of T-shaped vortical structure. (g) Structure believed to be a variation of structures shown in parts (c) to (f).

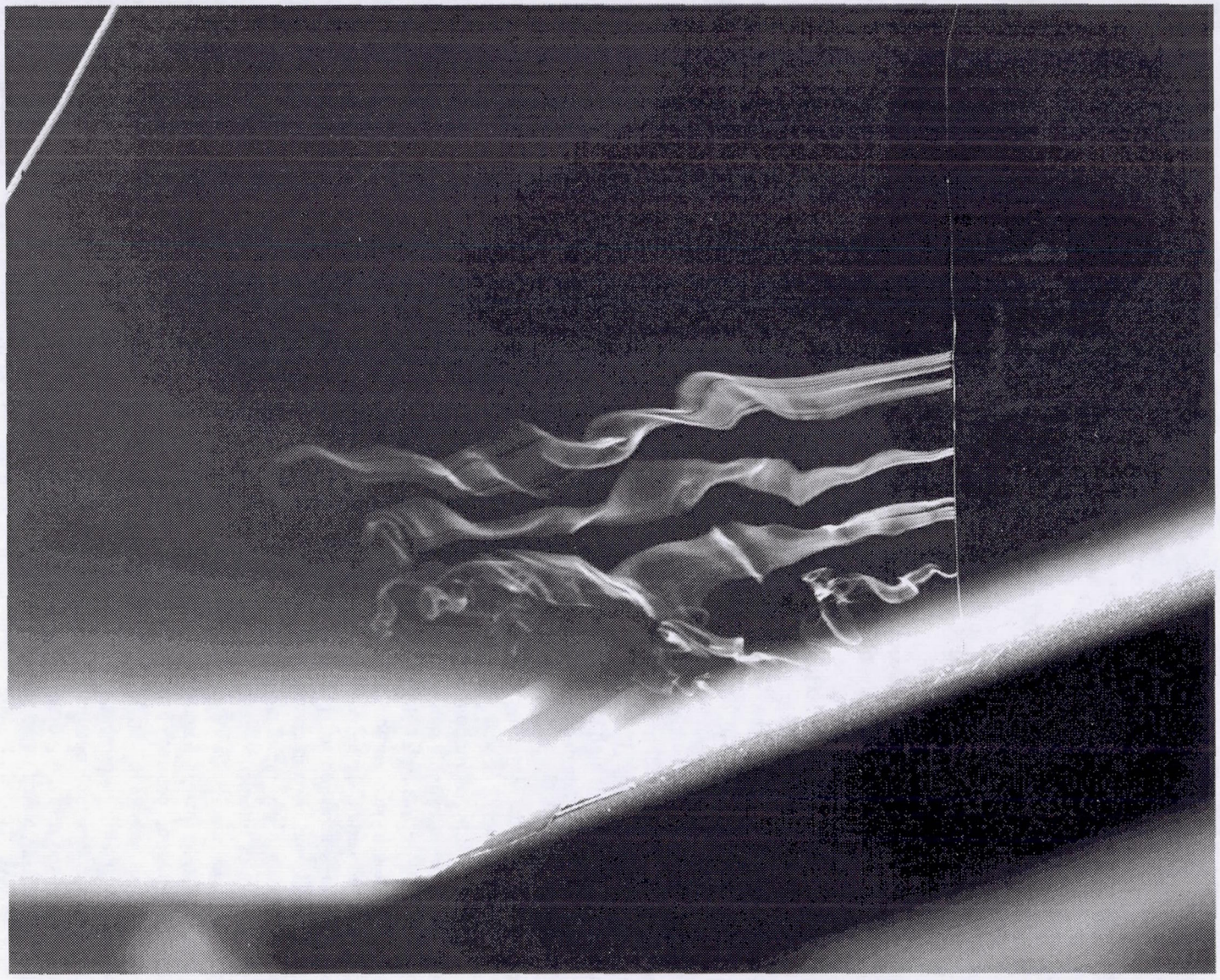

Figure 42.—Smoke-wire visualization showing several ribbons and single streaklines of smoke. Flow is moving from right to left; vane operation frequency, f, 25 Hz; inlet velocity, U_1, 2.6 m/sec; vane peak-to-peak displacement, h, 0.318 cm; smoke wire is located at L of 10.2 cm downstream from vane trailing edge.

tures are large and exist up to 5 cm above the surface in the upper region of the boundary layer. Additional sequences of motion pictures were obtained, but were not presented here, at nominally 10 and 15 cm downstream of the vane trailing edge. These showed what appeared to be a slow rotation about an arbitrarily located x-axis in the inner and/or outer region of the boundary layer.

Figures 43(a) and (b) present typical smoke-wire photographs with the smoke wire located at L of 15.24 cm downstream from the vane trailing edge and laterally 11.43 cm from the vertical plane passing through the wind tunnel centerline. Figure 43(a) shows a V-shaped envelope similar to that shown in the motion picture sequence of figure 39(b) in which the smoke wire was located at L of 1.90 cm downstream from the vane trailing edge. Note that the envelope contains large, loop-shaped structures of smoke that look like twisted, closed vortices. The included angle between the sides of the V is nominally 16°, which is curiously close to the natural expansion angle of two-dimensional and axisymmetric flows; the angle between the wall and the bisector of the V is approximately 50°. Figure 43(b) shows a group of omega-shaped vortices or vortex loops staggered axially and vertically in a V-shaped formation above the ramp surface.

A study by Head and Bandyopadhyay (ref. 31) presents flow visualization data of a zero-pressure-gradient turbulent boundary layer in the Reynolds number range $500 < Re_\theta < 17\,500$. These data have shown large Reynolds number effects on boundary layer structure. At high Reynolds numbers, the layer appeared to consist of elongated hairpin vortices or vortex pairs originating in the wall region and extending through a large part of the boundary layer thickness or beyond it. Large-scale features exhibited a slow overturning motion and appeared to consist mainly of random arrays of such hairpin vortices. In the lower Reynolds number range $900 < Re_\theta < 4000$, which is closer to that of the present study, reference 31 found that the hairpin vortices were less elongated and appeared as horseshoe-shaped vortices or vortex loops. Large-scale features appeared to consist of isolated vortex loops or of several such loops interacting strongly and appeared to rotate at a relatively rapid rate. Reference 31 discussed the mechanism of turbulence generation and predicted the formation of horseshoe-shaped vortices. If a flow is strictly two dimensional, reference 31 pointed out that vortex stretching and vortex rotation, required in the formation of horseshoe-shaped vortices, cannot occur. If, however, any degree of three dimensionality is present, the situation is otherwise, and the vorticity equation contains additional terms that implicitly represent the result of vortex stretching and rotation or tilting, which account for the intensification of vorticity that must precede and accompany the production of turbulence.

As demonstrated by the flow visualization data presented in figures 42 and 43, the streamwise vorticity downstream of the vane was increased by the strong interaction between the two spanwise vortices that ejected low-momentum vortical fluid into the outer high-momentum inviscid flow field. In this location, the vortical fluid was tilted and stretched downstream by the mean flow vertical and streamwise strain rates to produce a three-dimensional flow field containing large-scale vorticity. This large-scale vorticity would be expected to be transferred to smaller length scales by the mechanism discussed by Bradshaw (ref. 20). He points out that in fully developed turbulence, the key mechanism acting to maintain random fluctuation of the vorticity and velocity is the interaction of tangled vortex lines. In a discussion of the kinetic energy of the fluctuating motion, he indicates that vortex stretching increases the rotational kinetic energy of a vortex line and that the kinetic energy comes from the velocity field that does the stretching. Thus, the kinetic energy passes from the mean flow containing a mean strain rate down through vortex motions of smaller and smaller length scales until it is converted (by the bursting phenomenon in the vicinity of the wall) to turbulence and finally thermal internal energy through work done against viscous stress. Bradshaw indicates that if there is no mean strain field to do work on the fluctuating motion, the fluctuating motion gradually decays. Finally, he notes, this process of energy transfer to smaller scales is referred to as the "energy cascade," and is independent of viscosity except in the final stages. This description of the energy cascade is important because it provides a mechanism by which the periodic intrinsic axial vorticity resulting from the strong interaction events and ejection of the lifting line vortex into the outer inviscid flow field of the boundary layer is transferred down through vortex motions of smaller and smaller length scales until it is converted by the bursting phenomena in the vicinity of the wall to turbulence.

Figures 44 and 45 present dimensionless velocity and turbulent kinetic energy profiles at locations downstream from the oscillating vane trailing edge, at L of 5.72 and 9.52 cm, respectively. Velocity profiles in inner coordinates at these locations were presented previously in figures 31 and 32. In the lower 20 percent ($y/\delta = 0.2$) of the velocity profile presented in figures 44(a) and 45(a), note the unusual offset in its shape. This region of the boundary layer was fit by equation (8), which represents the rough-wall approximation, and is shown in figures 31 and 32. Figures 46(a) and (b) present velocity profile data at L of 17.1 cm downstream from the vane trailing edge in dimensionless and inner coordinates, respectively. This location is approximately 3.8 cm from the exit of the ramp and is the last location on the ramp at which data were obtained. Figure 46(b) indicates that the wall-wake equation approximates the entire mean velocity profile, which suggests that the turbulent kinetic energy production rate is in equilibrium with the inviscid kinetic energy dissipation rate at this location. Figures 17(b), 44(b), 45(b), and 46(c) present dimensionless turbulent kinetic energy profiles at distances downstream of the vane trailing edge L of 1.9, 5.72, 9.52, and 17.1 cm, respectively. In distinct regions of the flow

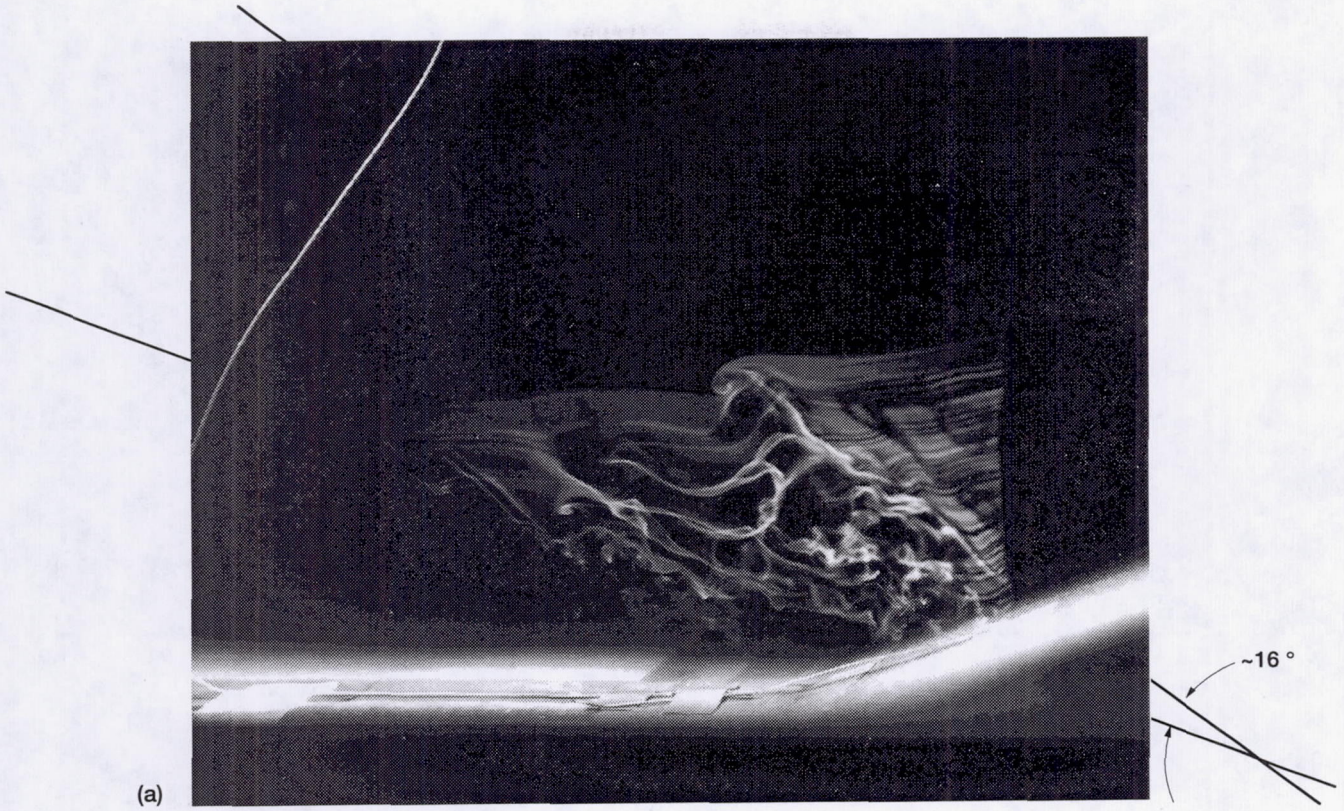

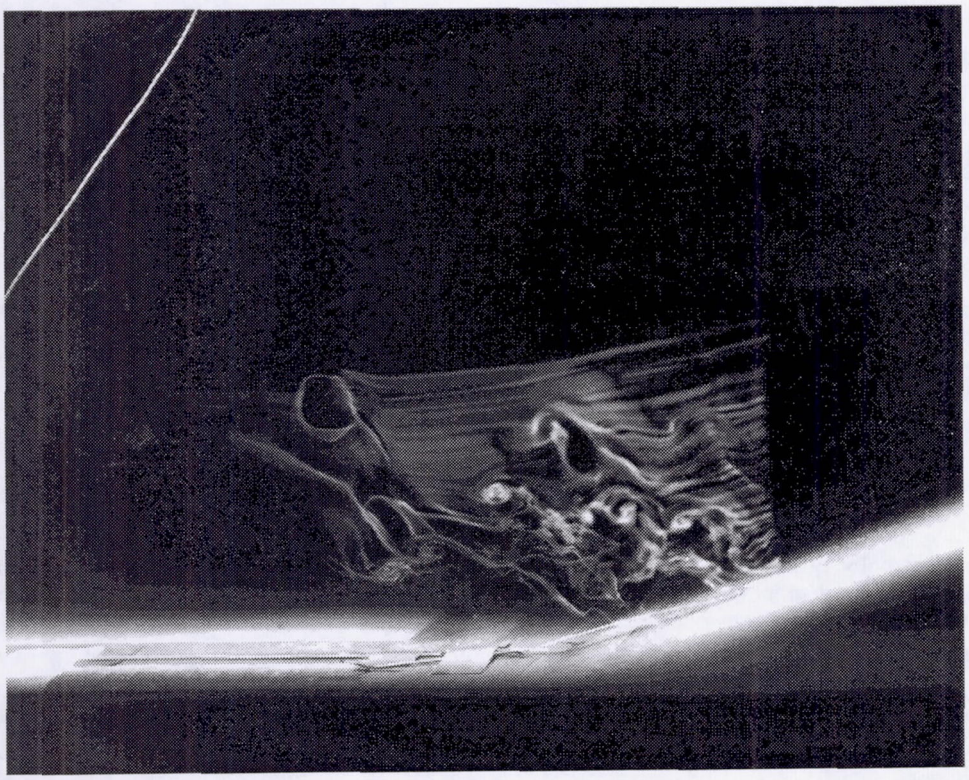

Figure 43.—Smoke-wire portrait photographs. Vane oscillation frequency, f, 25 Hz; inlet velocity, U_1, 2.6 m/sec; vane peak-to-peak displacement, h, 0.318 cm; smoke wire located at L of 15.24 cm downstream from vane trailing edge. (a) V-shaped envelope of structure. (b) Omega-shaped vortices or vortex loops.

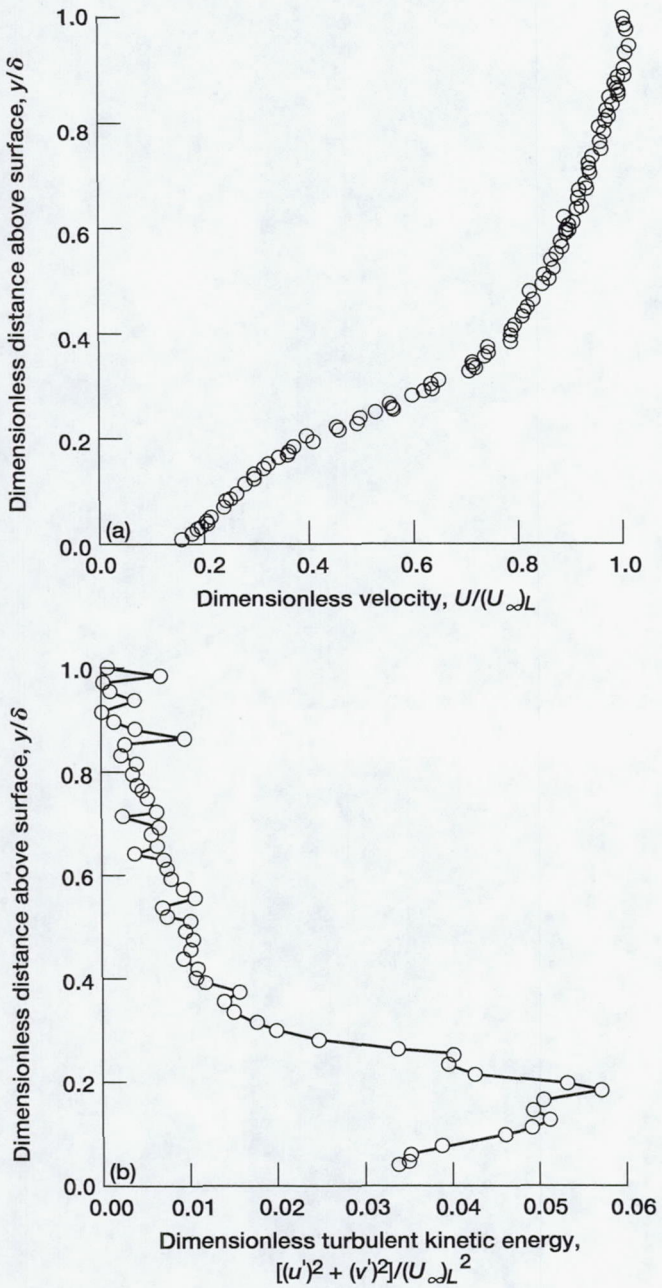

Figure 44.—Dimensionless velocity and turbulent kinetic energy profiles at L of 5.72 cm downstream from vane trailing edge; inlet velocity, U_1, 6.6 m/sec; excitation frequency, f, 30 Hz; vane peak-to-peak displacement, h, 0.318 cm; free-stream velocity at boundary layer edge, $(U_\infty)_L$, 6.25 m/sec; boundary layer thickness, δ, 4.77 cm. (a) Dimensionless velocity. (b) Dimensionless turbulent kinetic energy.

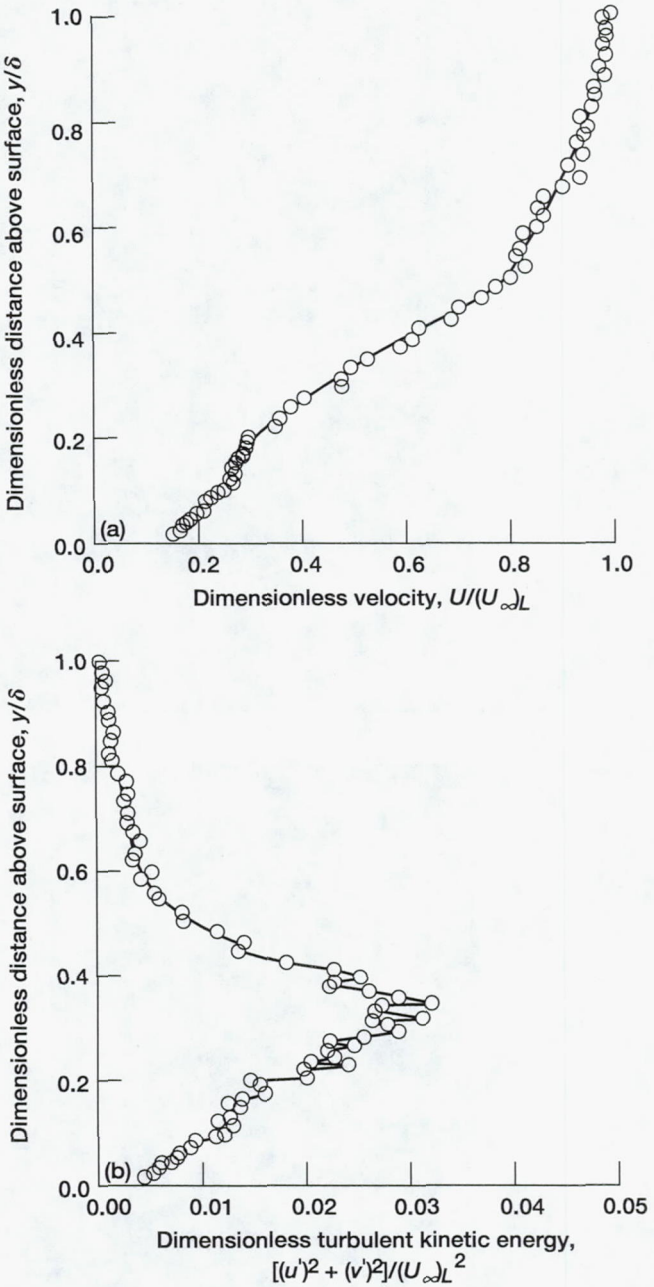

Figure 45.—Dimensionless velocity and turbulent kinetic energy profiles at L of 9.52 cm downstream from vane trailing edge; inlet velocity, U_1, 6.6 m/sec; excitation frequency, f, 30 Hz; vane peak-to-peak displacement, h, 0.318 cm; free-stream velocity at boundary layer edge, $(U_\infty)_L$, 6.24 m/sec; boundary layer thickness, δ, 5.33 cm. (a) Dimensionless velocity. (b) Dimensionless turbulent kinetic energy.

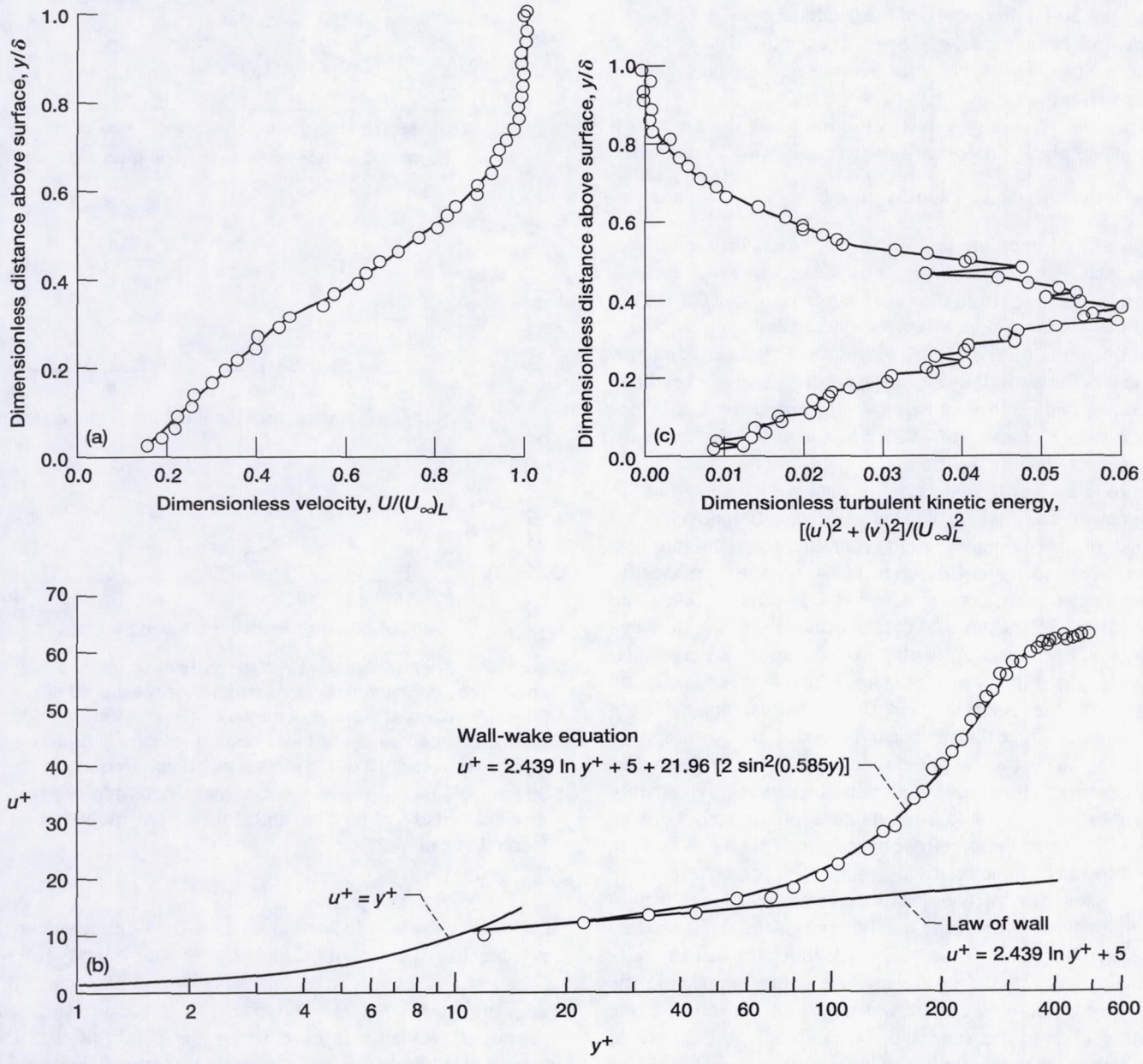

Figure 46.—Dimensionless velocity and turbulent kinetic energy profiles at L of 17.1 cm downstream from vane trailing edge; inlet velocity, U_1, 6.6 m/sec; excitation frequency, f, 30 Hz; vane peak-to-peak displacement, h, 0.318 cm. (a) Dimensionless velocity; free-stream velocity at boundary layer edge, $(U_\infty)_L$, 5.80 m/sec; boundary layer thickness, δ, 8.16 cm. (b) Velocity profile in inner wall coordinates. (c) Dimensionless turbulent kinetic energy profile; free-stream velocity at boundary layer edge, $(U_\infty)_L$, 5.80 m/sec; boundary layer thickness, δ, 8.16 cm.

field, these data indicate a high degree of erratic behavior similar to that discussed previously with reference to figures 17(b) and 20(c). This behavior is produced by periodic, but varying in amplitude, velocity fluctuations superimposed on an otherwise broadband spectrum. These fluctuations include the strong 30-Hz-frequency of the oscillating vane.

Spectral function data.—Spectral function data obtained using two single-wire, hot-wire anemometers are presented in figures 47 and 48.

Figure 47 presents the axial variation along the ramp surface of the phase difference ϕ between the two anemometer signals, the turbulence intensity $\left[u'/\left(U_\infty\right)_L\right]_{f=30\ \mathrm{Hz}}$, and coherence COH, measured at 30 Hz. The phase difference and coherence were measured with a fixed hot-wire probe located at an axial distance from the vane trailing edge L of 0.79 cm, a height above the surface y_P corresponding to 40 percent of the local free-stream velocity $(U_\infty)_L$, and a z of 10.2 cm. A mobile probe was moved axially along the ramp surface at a height of y_P corresponding to nominally 40 percent of the local free-stream velocity and a z of –1.27 cm. The turbulence intensity was measured using the mobile probe. From the vane trailing edge to at least an L of 10 cm, the data were obtained in the buffer layer. The gradient of the phase angle difference changed at an L of approximately 7 cm separating the ramp into two general regions having different phase speeds. The specific cause for this is not known; however, it is believed due to the distinctly different types of events occurring in the flow upstream and downstream of this axial location. For example, upstream the primary vortices (fig. 38(d)) evolved and interacted with the outer inviscid flow; downstream the flow transitioned to three dimensionality. Based on the power spectra at 30 Hz, the magnitude of the turbulence intensity showed an increase as the flow left the vicinity of the vane, fell sharply by almost 87 percent to a minimum approximately halfway down the ramp, and then rose at the exit. This behavior is in sharp contrast to the relatively small 25-percent variation in the turbulence intensity based on the rms value of the fluctuating velocity over the same axial length of the ramp surface. The axial variation of the coherence indicates that the relationship between the upstream disturbance signal and the effect measured downstream was nonlinear. However, in the vicinity of both the vane and the ramp exit, the degree of nonlinearity was relatively small. This may be indicative of the time-dependent shear layer phenomena (ref. 27) responsible for the high degree of static pressure recovery discussed earlier in the Pressure Recovery section .

Figure 48 presents the spanwise variation of spectral function data obtained at three streamwise axial locations. Figures 48(a) through (c) present the spanwise variation of the phase angle difference between the two anemometer signals, the turbulence intensity, and the coherence measured at 30 Hz and at axial locations L from the oscillating vane trailing edge of 0.48, 4.44, and 8.26 cm, respectively. For all three traverses,

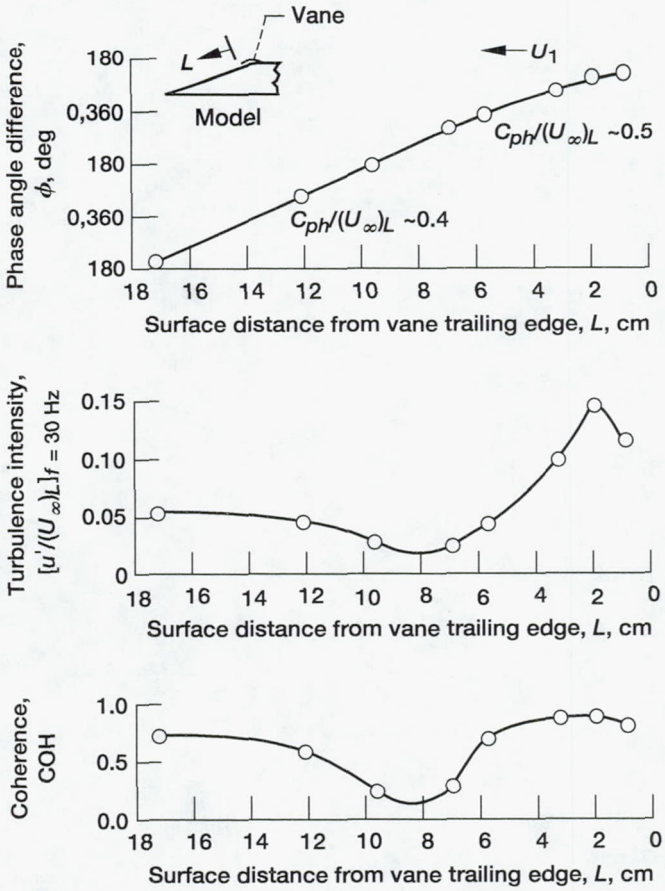

Figure 47.—Spectral function variation of phase angle difference, turbulence intensity, and coherence measured at 30 Hz versus axial surface distance from vane trailing edge measured at 40 percent of free-stream velocity in boundary layer; inlet velocity, U_1, 6.6 m/sec; excitation frequency, f, 30 Hz; vane peak-to-peak displacement, h, 0.318 cm. Fixed wire located at L of 0.79 cm and z of 10.2 cm; mobile wire located at z of –1.27 cm.

the fixed probe was located at an L of 0.48 cm, a y_P corresponding to 40 percent of the local free-stream velocity $(U_\infty)_L$, and a z of –1.27 cm. The mobile probe was moved above the ramp surface at a height of nominally 40 percent of the local free-stream velocity. In each figure the points of data are connected by dashed lines to indicate that insufficient measurements were made to reveal an accurate variation of the parameters. Thus, the variation of the data indicate only coarse trends as a function of the spanwise dimension z. At an axial location of 0.48 cm (fig. 48(a)), the two probes were located in the same spanwise plane. Note that the phase difference between the two anemometer signals varied within nominally ±25°, and the turbulence intensity showed a periodic variation with distinct minimums at z's of ±10 and ±30 cm. The smoke wire used to obtain the photographs presented in figure 41 was located coincidently at the same spanwise location

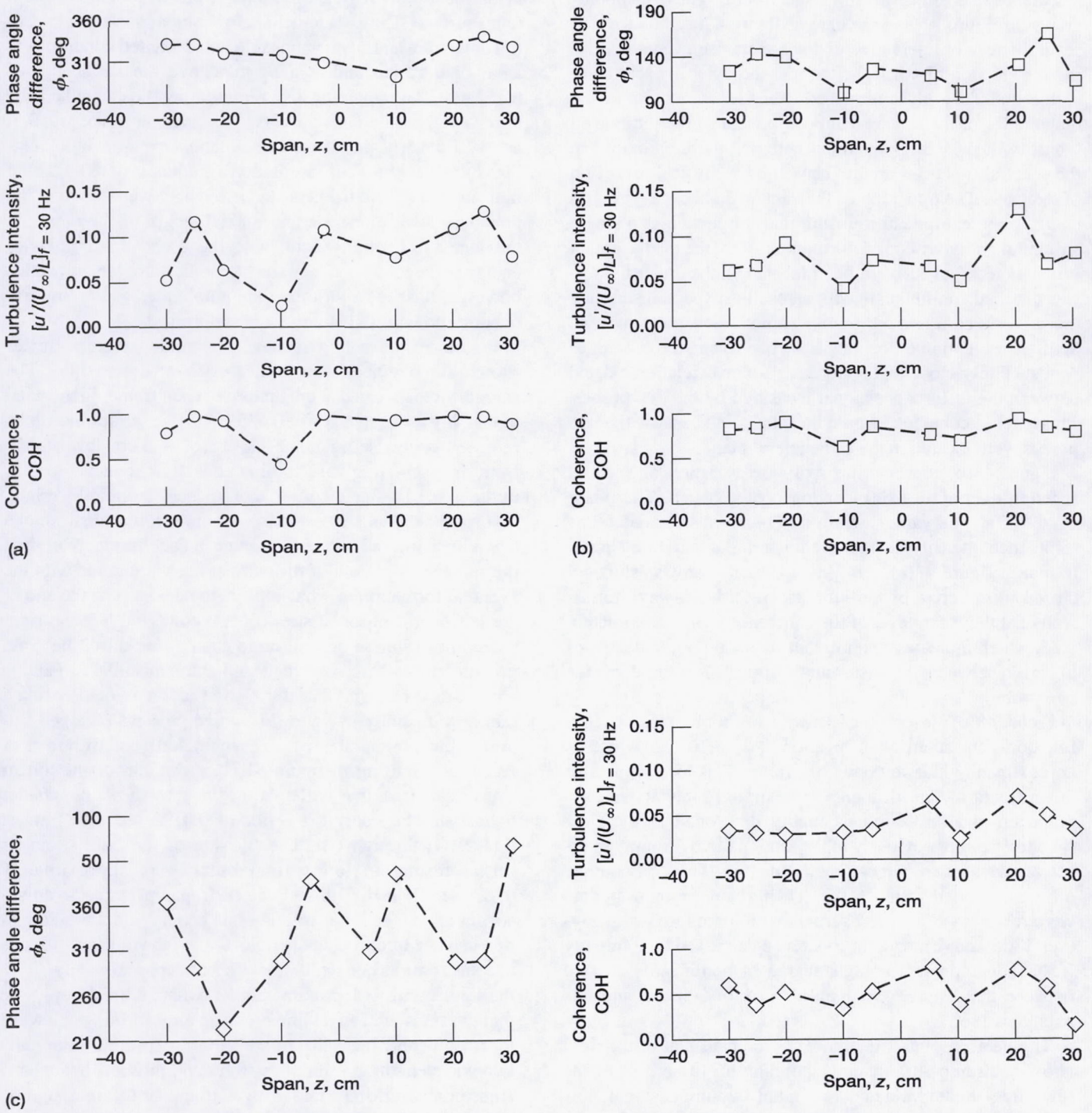

Figure 48.—Spectral function variation of phase angle difference, turbulence intensity, and coherence for three streamwise axial locations. Measurements made at 40 percent of local free-stream velocity in boundary layer; inlet velocity, U_1, 6.6 m/sec; excitation frequency, f, 30 Hz; vane peak-to-peak displacement, h, 0.318 cm. Fixed wire located at L of 0.48 cm and z of –1.27 cm. (a) Mobile wire located at L of 0.48 cm; local free-stream velocity, $(U_\infty)_L$, 6.45 m/sec. (b) Mobile wire located at L of 4.44 cm; local free-stream velocity, $(U_\infty)_L$, 6.74 m/sec. (c) Mobile wire located at L of 8.26 cm; local free-stream velocity, $(U_\infty)_L$, 6.25 m/sec.

(z of –10.79 cm) as one of the measured minimum-valued turbulence intensities shown in figure 48(a). Thus, the photographs in figure 41 and the data of figure 48(a) indicate that several strongly interactive distinct spanwise events involving the ejection of vortical fluid into the outer inviscid layer of the boundary layer produced spanwise variations in the magnitudes of the downstream component of the turbulence intensity. It must be pointed out here that these variations in the spectral functions are not caused by a physical distortion of the vane. The operation of the vane was checked regularly using strobe equipment to insure that it operated as a single structural entity without deformation. Also, the displacement fluctuations of an accelerometer located on the driver linkage was checked continuously with an oscilloscope to insure that the driver was operating with a smooth sinusoidal motion. With the exception of the data at a z of –10 cm, the coherence was generally close to 1, indicating a linear relation existed between the disturbance signal measured by the two probes. This level of coherence would be anticipated because the two probes were located in the same lateral plane.

Figure 48(b) presents the spanwise variation of spectral function data at an axial location L of 4.44 cm. The phase angle difference varied within ±35° and was periodic. The turbulence intensity data showed a periodic variation similar to that in figure 48(a). Also, an apparent spanwise shift occurred in the crest of the left- and right-hand wave forms. Note that the mean level of the coherence was approximately 0.85, which indicates a significant reduction in the degree of linearity between the disturbance signals measured by the two probes.

Figure 48(c) presents the spanwise variation of the spectral function data at an axial location L of 8.26 cm, which is approximately halfway down the ramp. This location is also downstream of the location where strongly interactive phenomenon and three dimensionality developed in the flow field (discussed previously in the section titled Strongly interactive events and three dimensionality). The phase angle difference varied within ±105°. The turbulence intensity data were relatively flat in comparison with that presented in figures 48(a) and (b), and the coherence decreased to nominally 0.50, indicating that a high degree of nonlinearity existed between the disturbance signal at an L of 0.48 cm and this axial location.

The data presented in figure 48 indicate that at a height above the ramp surface corresponding to 40 percent of the local free-stream velocity, the initial two-dimensional flow field was significantly affected by the evolution of a set of distributed, distinct, spanwise flow structures. As these structures evolved to a point nominally halfway down the ramp, increases in the variation of the spanwise phase angle difference occurred with an increase in the number of spanwise cycles. The increased number of cycles indicates that the flow field developed three dimensionality and that the initial structures were developing into axially oriented vortical structures.

Figure 49 presents power spectral measurements obtained in the near wall region at several axial locations along the ramp surface. These data include for comparison power spectral data representing the nonexcited and excited conditions at an L of 0.48 cm and at a height above the surface y_P of 0.152 cm. The remaining data representing the excited condition were measured at a y_P of 0.152 cm and at L's of 1.9, 9.5, and 17.1 cm. The data show a dominant narrow-band fluctuating signal at the vane oscillation frequency of 30 Hz and indicate that this signal persisted in the near wall region of the boundary layer along the entire axial length of the ramp. At the location L of 0.48 cm, note the broad distribution of energy in the low-frequency and harmonic narrow bandwidths; however, further downstream the amplitudes of the low-frequency and harmonic tones were suppressed.

Figure 50 presents a sequence of motion picture frames showing an overhead view of the smoke-wire streaklines. The smoke wire is located at the bottom of each frame. In the wind tunnel, it was located at y of 0.635 cm above the surface of the ramp in a spanwise z, y-plane and at L of 14.6 cm downstream from the oscillating vane trailing edge. The sequence begins in the upper left-hand corner and proceeds from left to right. Figure 50 shows the evolution of three prominent smoke streaklines located left of the center in each frame. Note first the spanwise back and forth sway of each streakline with the eventual formation of what appears to be a helix at the end of the left-hand sinusoidal streakline; second, the left and right streaklines sway in opposition to each other; third, the rapid growth in the helix before it and the sinusoidal streakline appear to break up. The third observation is demonstrated more prominently in figure 51, which presents enlarged figures of the motion picture frames in the forth and fifth rows of figure 50. Starting in figure 51(f), at the end of the longer sinusoidal streakline is the explosive growth of the smaller helical structure during a period of 0.0125 sec (five frames, figs. 51(f) through (j)). The lifetime of the helix from its initial formation to its final breakup is approximately 0.025 sec. Viewing this structure from upstream to downstream reveals that it is rotating in a counter clockwise direction and is approximately parallel to the ramp surface. Its axis of rotation turns counter clockwise from approximately 70° to the smoke wire to approximately 60° where it breaks up. Note that the sinusoidal streakline broke up after forming one wave length whereas the helix broke up after forming nominally two wavelengths. In summary, figure 50 presents helical and sinusoidal streaklines that grow and appear to break up into turbulence as the result of instability.

At this point in the discussion of the frequency-dependent phenomena responsible for the increase in the surface static pressure recovery, a review of the events occurring downstream of the vane reveals the following: First, flow visualization revealed the ejection of low-momentum vortical fluid into the outer high-momentum inviscid flow field. This ejection was the result of a strongly interactive phenomenon

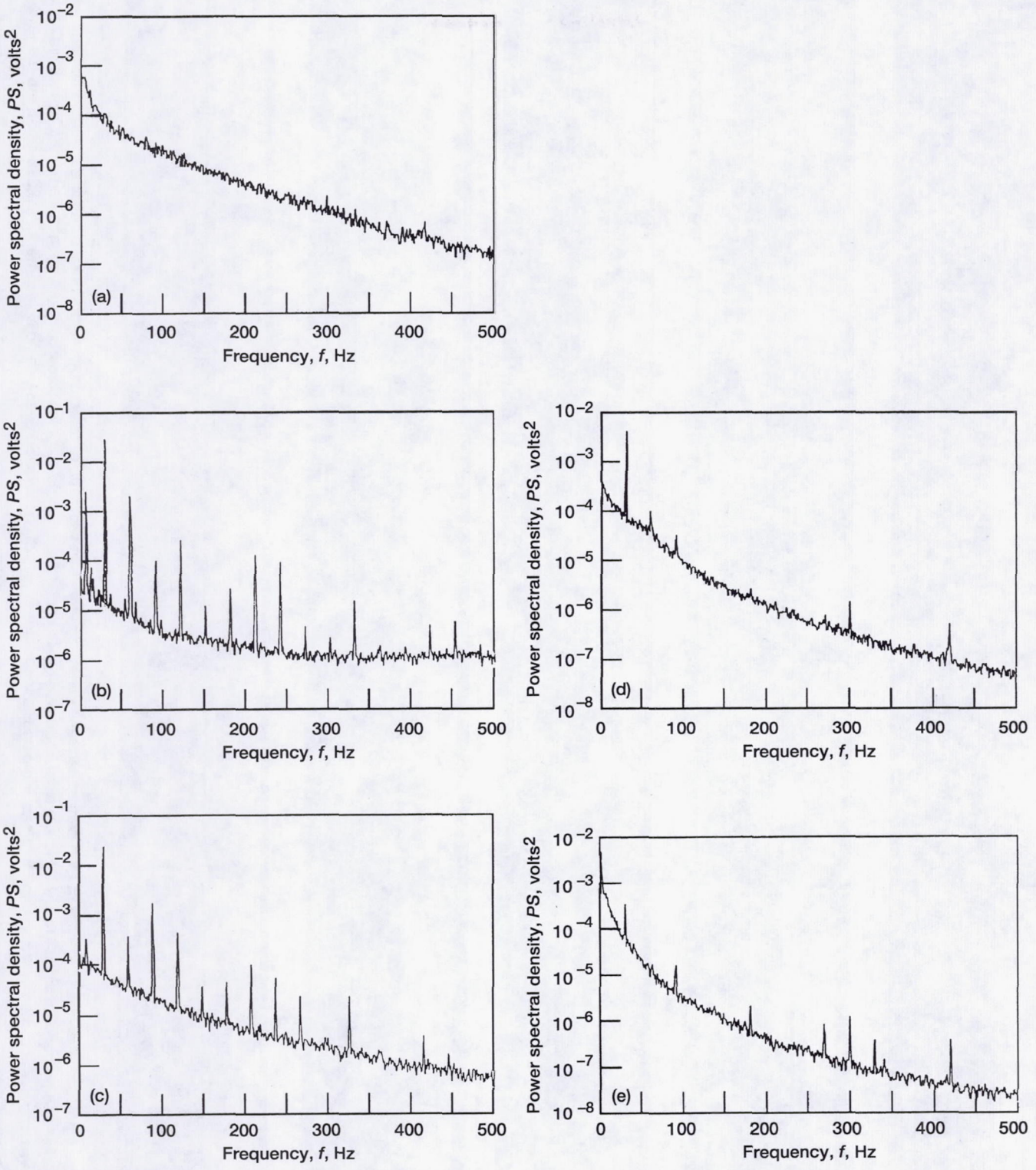

Figure 49.—Power spectra *PS* measured at several locations *L* from vane trailing edge and at y_P of 0.152 cm above ramp surface; inlet velocity, U_1, 6.6 m/sec. For excited cases (b) to (e), excitation frequency, *f*, 30 Hz; vane peak-to-peak displacement, *h*, 0.318 cm. (a) Nonexcited case; *L* = 0.48 cm; *PS* = 0.089×10^{-3} volt^2 at 30 Hz. (b) *L* = 0.48 cm; *PS* = 30.5×10^{-3} volt^2 at 30 Hz. (c) *L* = 1.9 cm; *PS* = 24.9×10^{-3} volt^2 at 30 Hz. (d) *L* = 9.5 cm; *PS* = 4.82×10^{-3} volt^2 at 30 Hz. (e) *L* = 17.1 cm; *PS* = 0.33×10^{-3} volt^2 at 30 Hz.

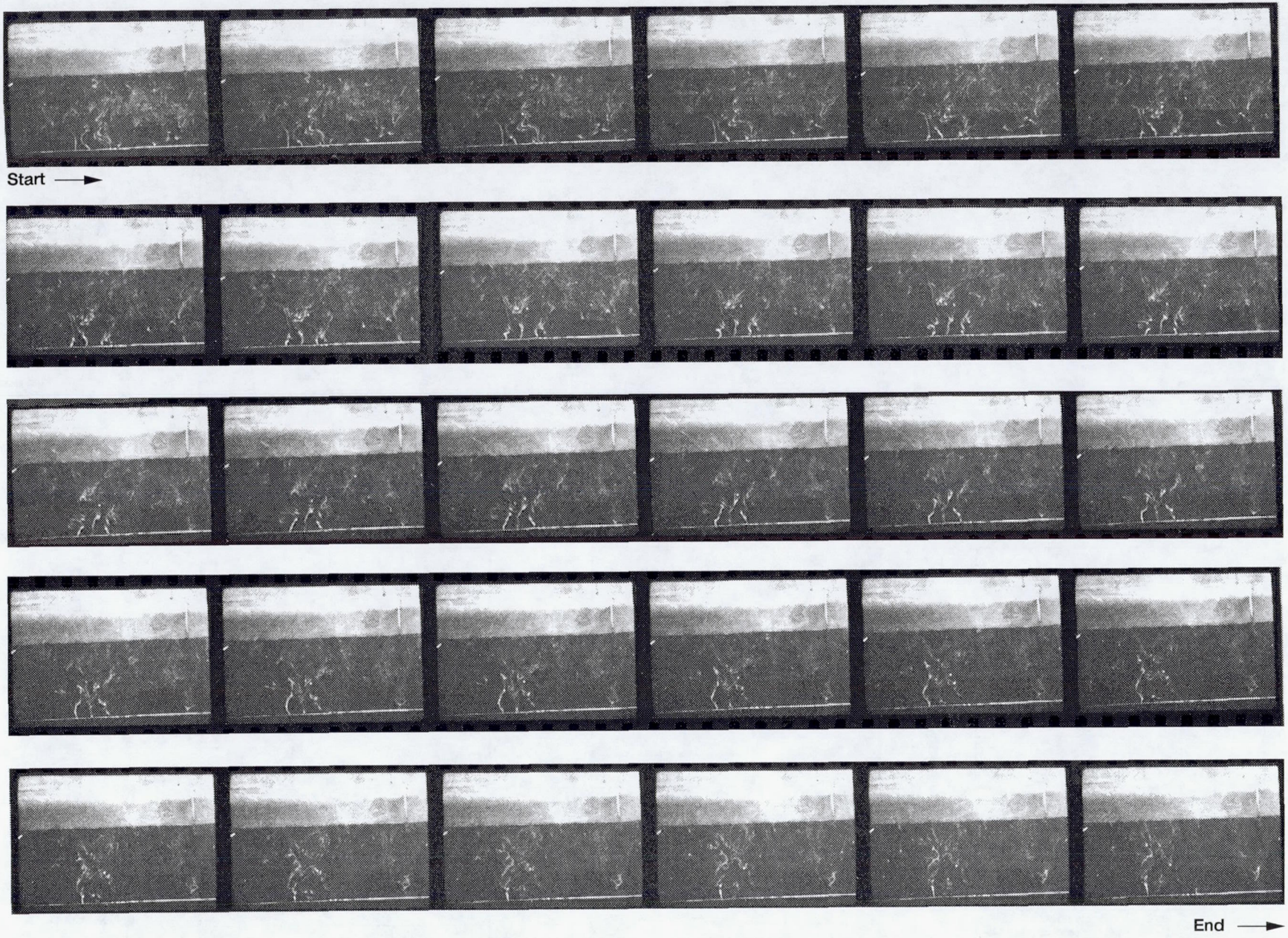

Figure 50.—Spanwise smoke-wire overhead view of motion picture sequence showing evolution with time of three prominent smoke streaklines. Sequence begins in upper left-hand corner and proceeds from left to right. Flow is from bottom to top in each frame. Smoke wire located at bottom of each frame at L of 14.6 cm and y of 0.635 cm above ramp surface; inlet velocity, U_1, 2.6 m/sec; vane oscillation frequency, f, 25 Hz; vane peak-to-peak displacement, h, 0.318 cm. Each frame represents 0.0025-sec time step.

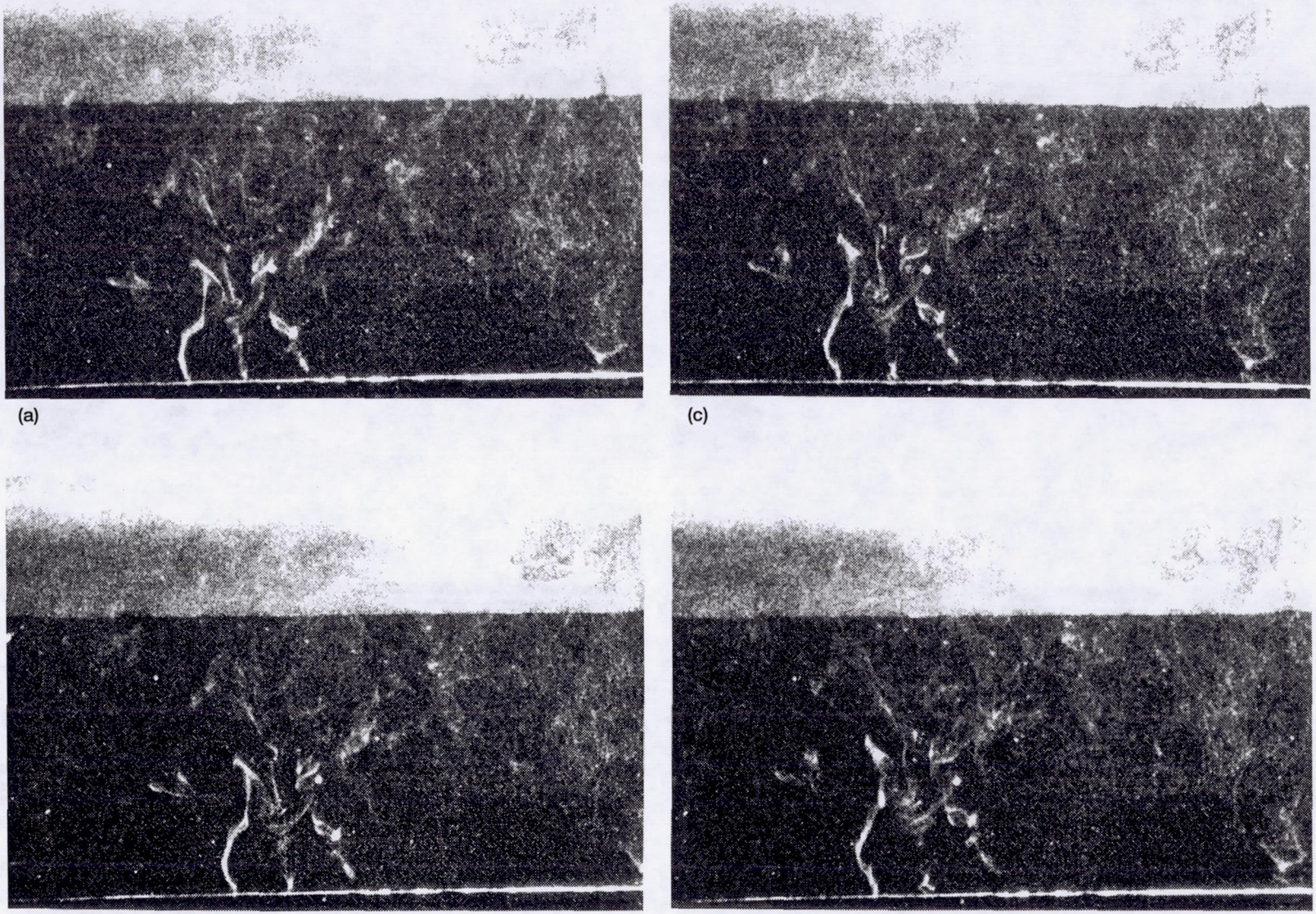

Figure 51.—Selected enlargements of motion picture frames from rows 4 and 5 of figure 50 showing explosive growth and breakup of helical and sinusoidal streaklines. (a to e) Sequence showing formation of sinusoidal streaklines. (f to i) Sequence showing further development of sinusoidal streaklines and explosive growth of helical structure at end of left-hand streakline. (j to l) Breakup of sinusoidal streaklines and helical structure.

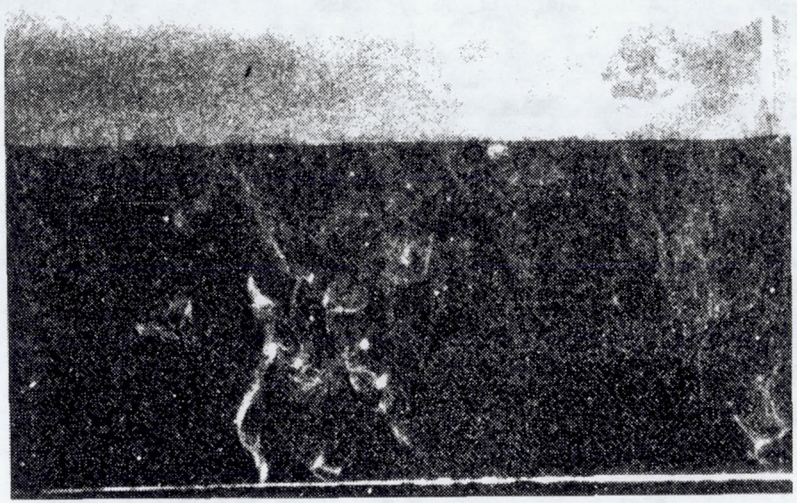

(e)

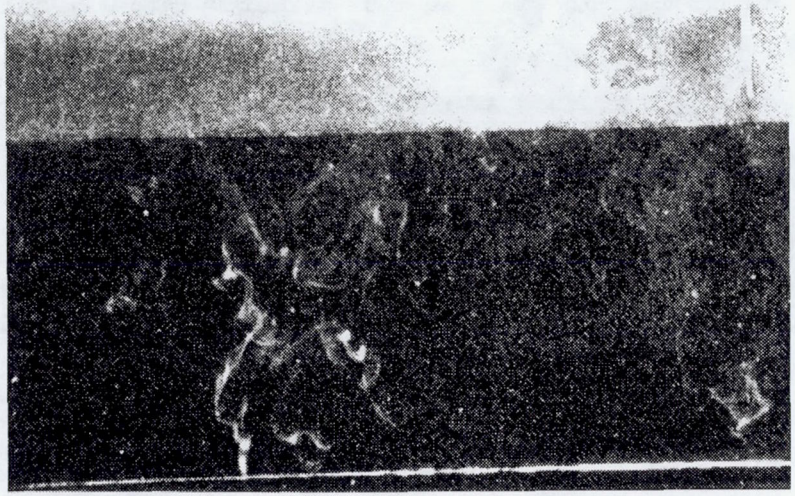

(g)

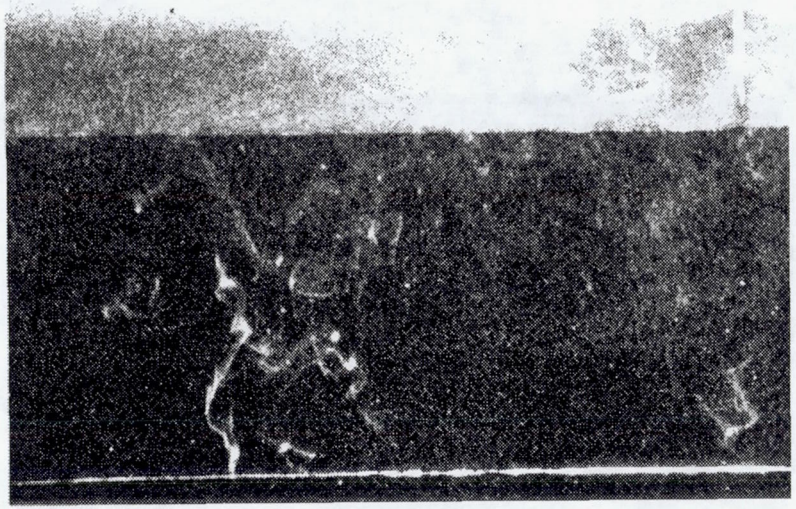

(f)

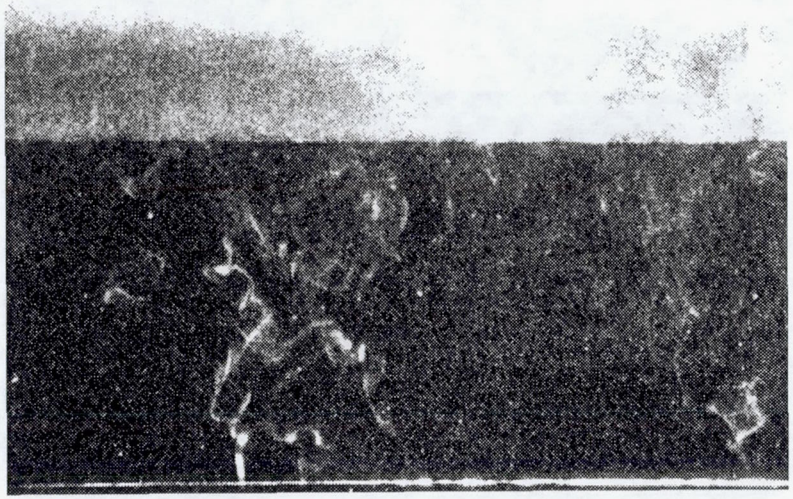

(h)

Figure 51.—Continued. (f to i) Sequence showing further development of sinusoidal streaklines and explosive growth of helical structure at end of left-hand streakline.

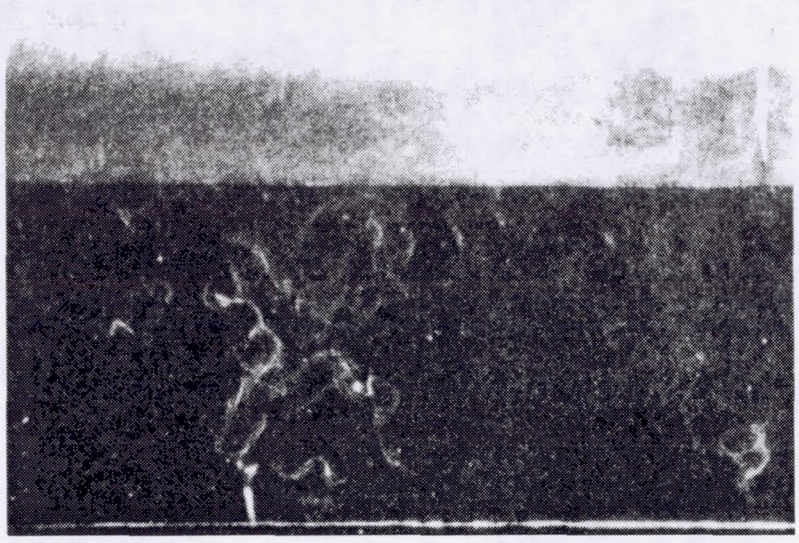

(i)

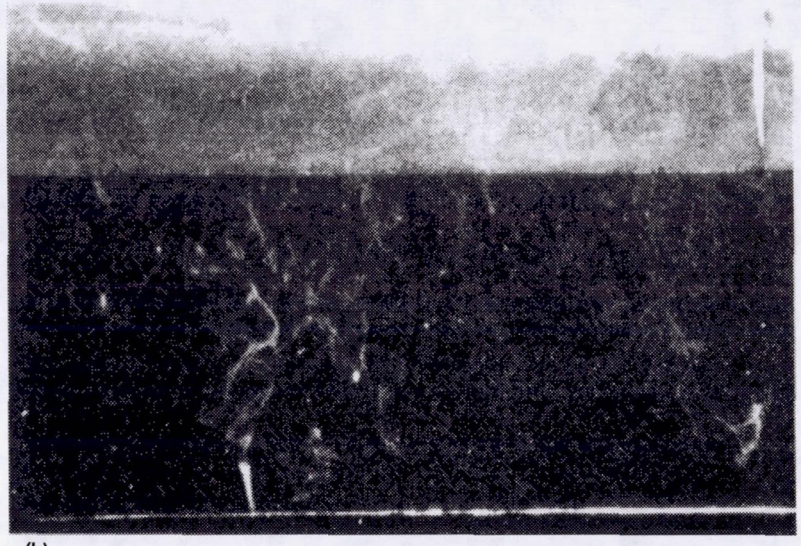

(k)

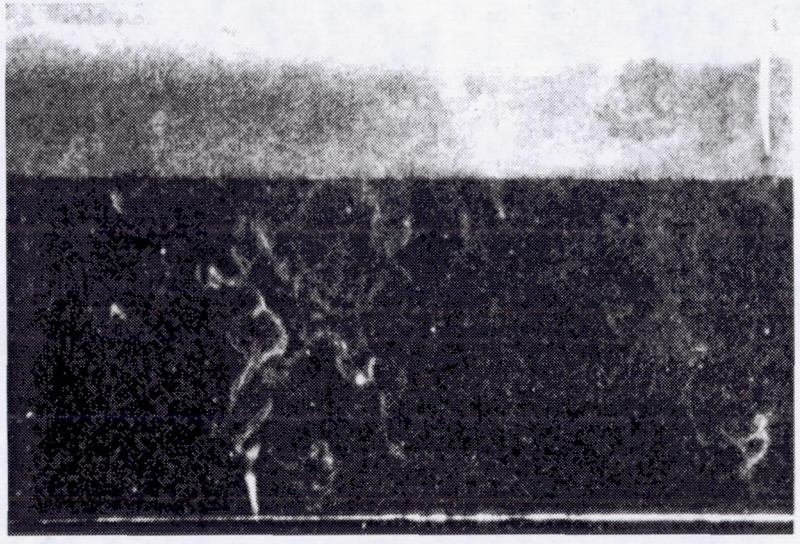

(j)

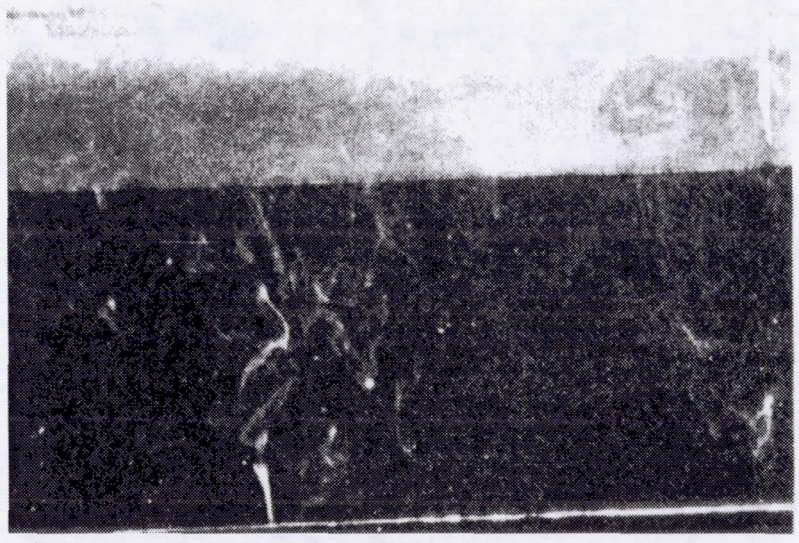

(l)

Figure 51.—Concluded. (j to l) Breakup of sinusoidal streaklines and helical structure.

between the spanwise vortical structures produced by the oscillating vane and the outer inviscid flow field. Second, the ejected spanwise vortical fluid was tilted and stretched downstream by the action of the vertical and axial mean flow strain rates, respectively, producing a three-dimensional flow field with axial vorticity. Figure 34 indicates that significant changes in the curvature and spacing of the flow streamlines occurred in the boundary layer near the vane. Thus, the local flow field experienced axial acceleration, deceleration, and centrifugal forces. These forces, in addition to variations in the surface static pressure coefficient, and the presence of significant vorticity imply that the local flow field could develop periodic streamwise-oriented vortical secondary flow structures. Third, a large, streamwise, helical-shaped ribbon structure was observed halfway down the ramp length in the outer region of the boundary layer where changes in streamline curvature were evident. Fourth, large loop-shaped structures resembling twisted closed vortices in addition to omega-shaped vortices staggered streamwise and vertically in a V-shaped formation were observed near the exit from the ramp. Fifth, spectral function data obtained at an excitation frequency of 30 Hz indicate that the flow field was significantly affected by a set of distributed, distinct, spanwise flow structures originating in the vicinity of the vane trailing edge. Sixth, axial power spectral measurements obtained in the near wall region of the boundary layer ($y^+ \approx 10$) showed a dominant narrow-band fluctuating signal at the vane oscillation frequency of 30 Hz and indicate that this fluctuation persisted in the near wall region along the entire axial length of the ramp. Seventh, figure 50 presents motion picture smoke visualization of sinusoidal and helical streaklines, which became unstable and broke up into turbulence. These streaklines were located in the near wall region of the turbulent boundary layer at a y^+ of 16.7 near the ramp exit.

The seventh event is particularly significant because evidence of turbulence generation in the near wall region is an essential link in the production/dissipation phenomenon that is characteristic of an attached turbulent boundary layer. In reference 27 Blackwelder and Swearingen present a study of the mechanism of turbulence generation produced by the bursting phenomenon. An outline of their investigation is presented in appendix B. The discussion of this reference is included here because it provides an understanding of a mechanism that may qualitatively explain, in the present study, the observed dependence of the surface static pressure recovery downstream of the vane on the vane oscillation frequency.

Proposed downstream flow-field excitation mechanism.— Blackwelder and Swearingen (ref. 27) investigated the generation of turbulence in the near wall region of a wall-bounded turbulent shear flow passing over a plate with a small concave curvature. Fluid flow passing over such a plate is characterized by moderately curved streamlines which are similar to those in figure 34 that characterize the flow field in the present study. Near the wall, the flow field is dominated by a series of events, collectively called the bursting phenomenon, which are responsible for the turbulence production and the drag. Blackwelder and Swearingen create a model of the phenomenon that is based on a review of linear instability theory and Görtler instability (ref. 32). They use these theories even though they describe the initial growth of a small disturbance on a wall for the case of laminar flow leading to transition. This approach is justified on the basis of observations made by many experimental and theoretical studies (ref. 22) that have concluded that there is great similarity in many aspects of the mechanism leading to transition and the continuous generation of turbulence in wall-bounded flows. Thus, reference 27 indicates that a series of events that occur in the wall region of bounded turbulent shear flows dominated by the bursting phenomenon is similar to that described for the Görtler problem; namely, there are counter-rotating streamwise vortices, elongated regions of low-speed fluid (low-speed streaks), and oscillation of these streaks, which rapidly grows to disintegration of the coherent motion. This disintegration is followed by strong mixing that results in the generation of turbulence. However, reference 27 indicates that the role of the streamwise vortices in turbulent flow is less clear than in the Görtler case. Until Blackwelder and Swearingen's investigation, no generally accepted definition of such a vortex was found in the literature. Thus, they define such a vortex as a coherent vortical parcel of fluid such that the instantaneous streamlines in the plane perpendicular to the vortex lines are closed. Blackwelder and Swearingen propose a mechanism for the final step in the series of events that collectively are the bursting phenomenon. The objective of their investigation was to examine the oscillation stage leading to the rapid growth and disintegration of the coherent motion and to propose a mechanism by which it may occur. The details of their experimental investigation and several observations about their test results are presented in appendix B.

Blackwelder and Swearingen performed a turbulent boundary layer experiment in which sequential instantaneous velocity profile data were obtained in the spanwise and streamwise directions. These data revealed that the strongest indication of the presence of streamwise vortices in turbulent boundary layers is the existence of low-speed streamwise streaks of fluid. These streaks imply the presence of inflectional velocity profiles. Their measured data revealed many inflectional velocity profiles in the wall region in the normal and spanwise directions of a turbulent boundary layer. Blackwelder and Swearingen applied Michalke's analysis of spacially growing disturbances in an inviscid shear layer (ref. 8) to the prediction of the amplified oscillation of the fluid streaks. They reasoned that if the inflectional profiles are indeed unstable, one should be able to predict the wavelength of the amplified oscillation. Michalke's results suggest that the wavelength λ for the most amplified wave number $\alpha_r \Delta$ of 0.40 will be 15.7Δ, where Δ represents one-half the vorticity thickness δ_w of the inflectional profile. A close examination of the data by

Blackwelder and Swearingen indicated that Δ varied approximately as (10±5) (ν/u_τ). Thus, the inflectional profiles should produce disturbances with wavelengths between 75 and 225, (ν/u_τ) where $\alpha_r\Delta$ is 0.40 and ν/u_τ is computed at the measurement location. Wavelengths in the same range were observed in reference 27, which indicated others, including Kline et al. (ref. 33), observed them also. Blackwelder and Swearingen concluded that inflectional profiles are a prevalent and ubiquitous feature of the wall region of turbulent flow fields and that the presence of low-speed streaks of fluid is sufficient to guarantee that there are inflectional velocity profiles in the spanwise and normal to the wall directions.

It is interesting to note that the range of Δ corresponds to the following limits of the vorticity thickness $\delta_w = 2\Delta$ in inner coordinates:

$$10 \leq \delta_w^+ \leq 30$$

Coincidently, these limits represent the nominal locations of the buffer layer boundaries (in inner wall boundary layer units) for a simple turbulent boundary layer in which the turbulent kinetic energy production rate is in equilibrium with the dissipation rate.

As mentioned above in the discussion of the measured test results presented herein, the helical and sinusoidal streaklines shown in figures 50 and 51 appear to grow and break up as the result of instability. During these tests, measurements of the instantaneous velocity profiles were not made; therefore, to apply Michalke's analysis, it is necessary to initially assume that the streaklines shown in figures 50 and 51 result from instantaneous inflectional velocity profile secondary instabilities and also mark the resulting low-speed streaks of fluid referred to in reference 27. With regard to the present tests, it must be emphasized that the production rate of the inflectional velocity profile secondary instabilities is not a direct result of the oscillating vane action in the sense that the vane does not produce them directly. Rather, their production rate is a function of the vane sinusoidal oscillation frequency.

The test conditions that produced the streaklines in figures 50 and 51 included an excitation frequency of 25 Hz, a vane displacement height of 0.318 cm, and an inlet velocity to the ramp of 2.6 m/sec. Figure 4 shows that these operating conditions produced a maxima in the curve of the maximum static pressure recovery measured near the exit of the ramp. The frequency of the sinusoidal streakline formation was computed to be 26.7 Hz using the motion picture flow visualization data (presented in fig. 50) that were obtained at a rate of 400 frames/sec. A second estimate of this frequency was 24.3 Hz, calculated by using measurements of the wavelength from figure 50 and the local velocity from measured mean velocity profile data. These values are very close to the 25-Hz operating frequency of the vane. In addition to this agreement, the appearance of the two parallel antisymmetric structures in figure 50 and those of the antisymmetric low-speed streaks of fluid shown in figure 2 of reference 27 are similar. These observations lend justification to the assumption that the streaklines in figures 50 and 51 mark low-speed streaks of fluid resulting from an instantaneous inflectional velocity profile.

From the data presented in figure 4, the frequency of the maximally unstable disturbance is known to be 25 Hz. If, indeed, the 25-Hz sinusoidal streaklines shown in figures 50 and 51 represent a maximum unstable disturbance resulting from a locally inflectional velocity profile, one should be able to approximate its vorticity thickness and compare it with the known range of such vorticity thicknesses roughly estimated by Blackwelder and Swearingen (ref. 27) and others. The most amplified wave number $\alpha_r\Delta$ of the broad range of growing harmonic disturbances may be expressed as

$$\alpha_r\Delta = \frac{4\pi St_\theta}{\left[\dfrac{C_{ph}}{(U_\infty)_L}\right]} \tag{12}$$

The dimensionless phase speed $C_{ph}/(U_\infty)_L$ measured near the exit of the ramp, was 0.40; and since the Strouhal number St_θ, representing the maximum amplification rate, is 0.17, thus, $\alpha_r\Delta$ was calculated to be 0.53. Therefore, the wavelength of the maximum unstable disturbance, in terms of one-half the vorticity thickness Δ, is expressed as $\lambda_x = 11.8\Delta$. The magnitude of $C_{ph}/(U_\infty)_L$ appears to be low, but it must be kept in mind that the flow is being forcibly excited, is passing over a surface that is effectively fully rough, and is simultaneously exposed to a strong, unfavorable pressure gradient. These conditions are highly unusual and are believed here to be responsible for this low level of $C_{ph}/(U_\infty)_L$. Based on the most amplified wave number $\alpha_r\Delta$ of 0.53 and the wavelength measured from figure 50, Δ was computed to be 4.8 (ν/u_τ). This value of Δ is very close to the lower limit of the range of the vorticity thicknesses, (10±5)(ν/u_τ), roughly measured by Blackwelder and Swearingen and other investigators, as pointed out in reference 27. If Δ is equated to 4.8 (ν/u_τ), the assumed inflectional profile in the present experiment would produce a disturbance with a wavelength, in inner coordinates, of $\lambda_x = 57$ (ν/u_τ).

Although the aforementioned results nominally agree with those in reference 27, there are several restrictions which remain to be satisfied in order to apply Michalke's analysis (ref. 8). Michalke's analysis was derived for a steady, two-dimensional, inflectional profile in a parallel unbounded flow. Reference 27 indicates that the following restrictions have been examined and satisfied in their study. The adverse effects of nonparallel flow have been found to be negligible when the local value of the mean flow is used in the stability calculations, which was the case in the present test. The adverse effects due to an unsteady mean flow are negligible if

the time scale of the instability is of the order of ν/u_τ^2. In the present test, the time scale for the sinusoidal instability wave was approximately 4 (ν/u_τ^2). The adverse effects due to the location of the inflectional region of the velocity profile are negligible if it is located at least 1.2Δ from the wall. In the present experiment, no measurements were made that specifically located the inflectional velocity profile in relationship to the model surface. However, because the smoke wire and the unstable structures shown in figures 50 and 51 were 3.5Δ above the model surface, it may be assumed that they were near the location of the inflectional velocity profile. The adverse effects due to three-dimensional flow were studied by Nishioka, Asai, and Ida (ref. 34), who concluded from experiments that the two-dimensional theory is valid in highly three-dimensional fields; however, the amplification rate is reduced but still remains large.

The foregoing discussion considered the data measured downstream of the oscillating vane and in the logarithmic law region and outer layer of the boundary layer presented in figures 34, 37 through 39, and 41 through 51. In addition, a review of reference 27 was included because it provides an understanding of a mechanism that may qualitatively explain the observed dependence of the surface static pressure recovery on the vane oscillation frequency. Based on the arguments presented in reference 27, an application of Michalke's linear analysis (ref. 8) was made and reasonably predicted the vorticity thickness and time scale of the structures observed in the near wall region of the turbulent boundary layer passing over the 20° rearward-facing ramp. It is proposed here that the periodic events (discussed in the section Results Downstream From Vane and in Logarithmic-Law Region and Outer Layer of Boundary Layer) collectively are the mechanism that produced the observed unique dependence of the static pressure recovery on the forcing frequency of the oscillating vane. These events involved the formation of macroscopic streamwise structures that led to the periodic formation of sinusoidal streaklines in the near wall region of the turbulent boundary layer and had the same time scale as that of the oscillating vane.

Concluding Remarks

Seldom does an experiment include the diversity of new phenomena that have been encountered in the present study of an excited turbulent flow passing over a 20° rearward-facing ramp. The phenomena are new, because they do not occur as a natural passive consequence of the gas dynamic flow. Rather, they are forced to occur by the action of an externally, superimposed, active excitation technique. The specific excitation technique incorporated the use of an oscillating vane positioned near the inlet to the ramp. The vane introduced two-dimensional, spanwise, periodic vortical structures directly into the inner wall region of the turbulent boundary layer experiencing transitory detachment. A delay in the detachment of the turbulent boundary layer from the ramp inlet was the primary result produced. Measurements of the surface static pressure coefficient along the ramp surface indicated that two different responses to the vane operation occurred: first, the pressure coefficient varied as a function of the vane oscillation frequency but was independent of increases in the vane displacement amplitude above an amplitude in inner wall boundary layer units y^+ of 70; second, below this limiting amplitude the static pressure coefficient varied as a function of both the vane frequency of oscillation and its displacement amplitude. These two dissimilar responses were investigated by a consideration, first, of the phenomena occurring in the immediate vicinity of the vane and continuing along the ramp surface in the buffer layer and linear sublayer, and, second, the phenomena occurring downstream of the vane and above the ramp surface in the logarithmic-law region and outer layer of the excited boundary layers.

The study of the phenomena that occurred downstream of the vane trailing edge along the ramp surface in the buffer layer and linear sublayer included an analysis of a wall jet located near the vane trailing edge. It was identified as a significant generator of the turbulence necessary to change the turbulence structure of the nonexcited shear layer at the inlet to the ramp from one characteristic of transitory detachment to one for the excited condition of attached flow. A second analysis considered the mean flow velocity profiles along the upper half of the ramp surface. This analysis indicated that the action of the vane produced an effective fully rough-wall condition characterized by a reduction of the viscous sublayer width to zero with a significant change in the turbulence structure of the boundary layer. This latter analysis provided an explanation for the limited effectiveness of the oscillating vane displacement height in controlling the surface static pressure recovery along the ramp surface. That is, for the case in which the vane displacement height was set equal to its effective limiting amplitude, the action of the vane produced an effective fully rough-wall condition characterized by a reduction of the viscous sublayer width to zero; thus, no further increase in the effective roughness of the rough-wall condition was possible with increases in the vane displacement height. Based on these findings, it is proposed here that the wall jet and the fully rough-wall condition along the upper half of the ramp surface are manifestations of the oscillating vane periodic formation of the spanwise two-dimensional starting vortices that attached themselves to the ramp surface. These vortices acted as the principal mechanism that produced the delay in detachment of the turbulent boundary layer as a function of the vane oscillation frequency and a limited range of its trailing edge displacement amplitude.

The study of the phenomena that occurred downstream of the vane and above the ramp surface in the logarithmic-law region and outer layer of the excited boundary layers included smoke-wire flow visualization, which showed that two spanwise counter-rotating vortices were generated by the action of the oscillating vane. One of these was a starting vortex that

attached itself to the ramp surface; the other was a lifting line vortex that remained detached. They dynamically interacted with each other in an unstable, strongly interactive event that ejected the low-momentum fluid of the detached vortex into the high-momentum region of the outer inviscid layer. This fluid formed a set of distributed, distinct, spanwise mushroom or omega-shaped macroscopic structures that were tilted and stretched or compressed downstream by the action of the vertical and axial mean flow strain rates, which produced a three-dimensional flow field with significantly increased streamwise vorticity. This event produced periodic disturbance signals that then became intrinsic to the fluid and altered the in-flowing, two-dimensional flow field. Downstream of these events, smoke-wire flow visualization showed large, streamwise, helical-shaped structures that appeared to be in rotation. Observed near the ramp exit were large, loop-shaped and omega-shaped vortices staggered axially and vertically in V-shaped formations. In the near wall region of the turbulent boundary layer, smoke-wire flow visualization revealed that streamwise-oriented sinusoidal streaklines were present. Motion pictures showed the streaklines transitioning to instability and then breaking up into turbulence. The period of these sinusoidal streaklines was measured and was the same as that of the oscillating vane, which was located at the inlet to the ramp. The breakup of these streaklines into turbulence is particularly significant because evidence of turbulence generation in the near wall region is an essential link in the production /dissipation phenomena characteristic of attached turbulent boundary layers. An analysis of these streaklines reasonably predicted their vorticity thickness and time scale. Thus, the analysis indicated that the streaklines were the result of the rapid growth of inflectional velocity profile secondary instabilities that are a prevalent feature of the wall region of turbulent boundary layers. It is proposed here that the periodic events just described collectively are the mechanism that produced the observed unique dependence of the surface static pressure recovery on the forcing frequency of the oscillating vane. These events involved the formation of macroscopic streamwise structures that led to the periodic formation, in the near wall region of the turbulent boundary layer, of sinusoidal streaklines having the same time scale as that of the oscillating vane.

The operation of the vane showed that it could force sufficient turbulence generation in the near wall region of the boundary layer to produce changes in the turbulence structure. These changes were large enough to alter the mean flow velocity profiles; thus, the magnitude of the changes in the turbulence structure can be arbitrarily controlled. This indicates the degree of boundary layer attachment in the diffuser-type flows can be controlled using such a device.

The turbulent generation phenomena that produced a delay in the detachment of the turbulent boundary layer were revealed through the combined use of hot wires and smoke-wire flow visualization techniques. The combined use of these two techniques is believed here to be essential because of their complimentary nature. That is, the use of the hot wires is ideal for obtaining the statistical data used to quantify turbulent flow; however, they are much less satisfactory for revealing the existence of organized flow structures that vary widely in size and orientation. This, however, is just the information that can be obtained from flow visualizations studies.

The excitation technique used here introduced a periodic perturbing signal directly into the near wall region of the turbulent boundary layer experiencing transitory detachment. The experimental investigation of flows in which such periodic perturbing signals are used requires the acquisition of instantaneous data including flow visualization. An example in the present experiment concerned the application of Michalke's analysis of spatially growing disturbances to the rapid growth of inflectional velocity profile secondary instabilities in the near wall region of a turbulent boundary layer. The need for instantaneous fluid dynamic data acquisition when studying such periodic flow phenomena represents a major change in thinking for the typical experimentalist who generally acquires time-averaged data required for statistically based, Reynolds-averaging analyses. In a mutually complimentary sense, it is noted that this approach is compatible with the instantaneous capture of events using motion picture flow visualization techniques.

The regularization of the phenomena occurring in the near wall region of a turbulent boundary layer effected by an oscillating vane positioned at the inlet to a rearward-facing ramp may offer experimentalists an opportunity to study the mechanisms that occur in buffer layers, which are not well understood at this time.

Summary of Results

A vane oscillating about a fixed point at the inlet to a two-dimensional 20° rearward-facing ramp proved effective in delaying the detachment of a turbulent boundary layer. Unlike passive devices, such as stationary vortex generators, the oscillating vane is an active control device. Control is accomplished by introducing into the inner layer of the boundary layer a sinusoidal two-dimensional perturbing signal, which can be varied in amplitude and frequency. This control potentially makes the vane ideally suited to excite the growth of secondary stability waves that become unstable and thereby produce turbulent mixing and improve boundary layer attachment. During initial tests, the delay of detachment was ascertained by measuring the surface static pressure coefficient distribution over the ramp surface. The results of these measurements indicated that the static pressure coefficient varied as a complex function of the vane oscillation frequency and its displacement amplitude. It was found that the perturbing signal could be controlled to provide a broad range in the static pressure recovery over the surface of the ramp.

Although the delay in detachment of the turbulent boundary layer appeared, at first, to be a direct consequence of the periodic flow structures produced by the vane, this study

revealed that, in fact, the actual mechanism is more complex. Therefore, this summary is divided into three parts: first, a review of the general cause and effect results demonstrated by the variation in the axial distribution of the surface static pressure coefficient; second, a consideration of the results occurring in the vicinity of the vane and in the buffer layer and linear sublayer of the boundary layer; and third, a consideration of the results occurring downstream from the vane and in the logarithmic-law region and outer layer of the boundary layer.

Surface Static Pressure Results

Exploratory measurements of the surface static pressure coefficient and the local flow reversal rates revealed that the oscillating vane turned the flow through a 20° angle at the ramp inlet and brought about a delay in the flow detachment to beyond the ramp exit. The axial distribution of the surface static pressure coefficient indicated that two different responses to the operation of the vane occurred; first, the pressure coefficient was independent of increases in the vane displacement amplitude above the ramp surface greater than approximately 70 inner wall units. This indicated that the action of the vane primarily affected the buffer and viscous sublayers of the boundary layer. Second, below this limiting amplitude, the pressure coefficient varied as a function of both the vane oscillation frequency and displacement amplitude.

A parametric study was performed of the maximum values of the static pressure recovery measured at the ramp exit as a function of the vane oscillation frequency for several ramp inlet velocities at a constant vane displacement amplitude. The excitation frequency corresponding to the maxima of each curve increased in some proportional relationship with an increase in the ramp inlet velocity. This result implies that the fluid dynamics mechanism producing the optimum delay in detachment is Strouhal number dependent.

Results in Vicinity of Vane and in Buffer Layer and Linear Sublayer of Boundary Layer

Hot-wire anemometer mean velocity and turbulent kinetic energy profile data and corona anemometer probability density function data revealed a wall jet and two distinct peaks in the probability density function suggesting that the oscillating vane produced two spanwise vortices per cycle of operation.

Flow visualization data confirmed that the vane effected the production of two spanwise vortices per cycle of operation. The vane acted as an oscillating airfoil with the steady release of counter-rotating spanwise starting and lifting line vortices. The starting vortex attached itself to the surface of the ramp and remained attached as it was convected downstream; the lifting line vortex remained detached above the surface and dynamically interacted with the starting line vortex. The attachment of the starting line vortex to the ramp surface was found to be a necessary condition for the effective operation of the vane and occurred only if the oscillating vane made intimate contact with the surface during the retraction cycle of its operation.

Hot-wire anemometer measurements indicated that significant changes occurred in the curvature and spacing of the flow streamlines near the vane where axial acceleration, deceleration, and centrifugal forces were acting on the fluid. The necessary changes in the turbulence structure of the boundary layer to turn the flow through the 20° angle of curvature required to negotiate the inlet to the ramp were revealed by an analysis of the mean flow velocity profile near the oscillating vane trailing edge. In the inner boundary layer region, this velocity profile revealed the presence of a wall jet. The analysis identified the wall jet as a significant generator of the turbulence necessary to change the turbulence structure of the nonexcited local shear layer from that characteristic of transitory detachment to one for the excited condition of attached flow.

Presentation in inner wall coordinates of the mean flow velocity profiles along the upper half of the ramp axial surface length showed that the shape of the inner wall layer profiles were unusual. The action of the vane significantly increased the width of the buffer layer. This meant that the boundaries of the buffer layer were extended deeply into the viscous sublayer and up into the logarithmic layer. Analysis of these data revealed that the increases in the width of the buffer layer were characteristic of flow passing over a fully rough wall with no effective viscous sublayer.

Results Downstream of Vane and in Logarithmic-Law Region and Outer Layer of Boundary Layer

Downstream from the vane, smoke-wire flow visualization showed that the starting and lifting line vortices generated by the action of the oscillating vane operating at the maximally unstable perturbing frequency dynamically interacted with each other and the outer inviscid flow in a strongly interactive event. During this unstable interactive event, the low-momentum fluid of the lifting line vortex was ejected into the high-momentum region of the outer inviscid layer. This ejected vortical fluid was distorted into a mushroom or omega-shaped macroscopic structure. While this structure was forming, it was tilted and stretched or compressed downstream by the action of the vertical and axial mean flow strain rates, respectively, which produced a three-dimensional flow field with significantly increased streamwise vorticity. This event produced a periodic disturbance signal that then became intrinsic to the fluid. Spectral function data measured in a spanwise plane identified several sites where these unstable, strongly interactive events occurred; thus, a spanwise distributed set of such flow structures was produced. Therefore, the two-dimensional flow field was significantly altered by the evolution of these spanwise, distributed, periodic disturbance struc-

tures. Midway down the ramp in the outer layer of the boundary layer, where changes in streamline curvature existed, smoke-wire flow visualization showed a large, streamwise, helical-shaped ribbon of smoke that appeared to be in rotation. Near the ramp exit, large loop-shaped structures resembling twisted ring vortices were observed in addition to omega-shaped vortices staggered axially and vertically in a V-shaped formation. Axial power spectral measurements obtained in the near wall region of the boundary layer indicated that a dominant narrow-band signal corresponding to the vane oscillation frequency persisted in the near wall region along the entire axial length of the ramp.

Near the ramp exit, motion picture smoke-wire flow visualization showed that axially oriented (streamwise) sinusoidal streaklines were located in the near wall region of the turbulent boundary layer. The sequence of frames showed the streaklines transitioning to instability and then breaking up into turbulence. The measured period of these sinusoidal streaklines was the same as that of the oscillating vane located at the inlet to the ramp. The breakup of these streaklines into turbulence is particularly significant because evidence of turbulence generation in the near wall region is an essential link in the production/dissipation phenomena characteristic of the attached turbulent boundary layer. Blackwelder and Swearingen studied the mechanism of the turbulence generation produced by the bursting phenomenon. They proposed a mechanism for the final step in the series of events that collectively represent the bursting phenomenon. The mechanism includes a consideration of, first, the growth rates of the flow disturbances predicted by Michalke's theory of spatially growing disturbances in an inviscid shear layer and, second, the instantaneous changes in the measured data velocity profiles which revealed that many inflection points existed in the wall region. These inflectional profiles then open the way to an inviscid instability that has very large growth rates. They found that their data and that in the literature supported the conclusion that inflectional profiles are a prevalent and ubiquitous feature of the wall region of turbulent flow fields and that the presence of low-speed streaks of fluid is sufficient to guarantee that there are inflectional velocity profiles in the spanwise direction and normal to the wall. Based on the arguments presented by Blackwelder and Swearingen, Michalke's stability analysis was applied to the sinusoidal streakline discussed above. The results of the analysis reasonably predicted the vorticity thickness and time scale of these structures.

Acknowledgments

The author expresses his sincere appreciation to Brently C. Nowlin and James E. Little for their extraordinary efforts in the design and fabrication of the electronic computerized instrumentation required for the control and operation of the corona anemometer used in this work; J. David Clinton for the extensive and extremely important acquisition of flow visualization motion picture data; and finally, Richard A. Brokopp and Ralph Fallert for their attention and ready hands-on support of this work.

Lewis Research Center
National Aeronautics and Space Administration
Cleveland, Ohio, July 10, 1995

Appendix A

Analysis: Overview of Bradshaw's Technique

As indicated by Peter Bradshaw (ref. 15), large effects are exerted on shear flow turbulence by the curvature of the streamlines in the mean shear plane. He demonstrates these effects by comparing, as a common example, the rate of boundary layer growth on a highly cambered airfoil or turbomachinery blade with the rate of boundary layer growth, in the same pressure gradient, on a flat noncambered surface. The comparison reveals that decreases occur in the rate of boundary layer growth on the convex upper surface and increases occur on the concave lower surface of the highly cambered blade. A brief overview of his technique follows.

Concept of Thin Shear Layers

Bradshaw considers the standard explanation of how flow behaves as it passes over a curved surface, expressed mathematically by

$$\frac{\partial P}{\partial y} = -\frac{\rho U_T^2}{R} \tag{A1}$$

where P is the surface static pressure, ρ is the density, U_T is the tangential velocity, and R is the radius of curvature. That is, centrifugal forces are balanced by pressure forces. He presents a different view of this concept by postulating the existence of thin shear layers of high-Reynolds-stress fluid that can, if large enough, force changes in the mean flow motion of bounded shear flows. This concept is based on the argument that the production rate of turbulent kinetic energy is balanced by its dissipation rate. Applying order of magnitude arguments, augmented by the knowledge of the magnitudes of experimental measurements, he deduces that these layers exist and he quantifies and labels them. A brief presentation of his argument follows.

In reference 15, Bradshaw begins by considering a flow that is subjected to a change in turbulence structure so large that the mean pressure gradient changes the mean flow motion. This prompts the question, How might this occur? He assumes a typical velocity U_e and a length scale S in the general direction of the flow. In general, mean pressure gradients in any direction will be of the order

$$\frac{\rho U_e^2}{S}$$

whereas, according to experiments, Reynolds stresses gradients are at most of the order

$$\frac{0.01\rho U_e^2}{S}$$

Therefore, Reynolds stress gradients will affect the mean motion if they are of the same order as pressure gradients only if Reynolds stresses change significantly over distances of the order $0.01S$.

Bradshaw points out that an examination of the Reynolds stress transport equations shows that the Reynolds stresses are unlikely to change so rapidly with distance along a mean streamline. Thus, he makes the argument that Reynolds stress gradients will significantly affect the mean motion only if they change significantly in a distance of the order $0.01S$, which is more or less normal to the mean streamline. This change requires the existence of thin sheets or slender tubes of high Reynolds stress.

Bradshaw begins a proof of this argument by observing that the only general mechanism by which such layers can maintain themselves is through the extraction of energy from the mean flow by the working of a mean rate of strain against the Reynolds stresses,

$$-\overline{uv}\frac{\partial U}{\partial S}$$

where $-\overline{uv}$ is the Reynolds shear stress. Therefore, the rate of dissipation ($\varepsilon = (U^2)^{3/2}/L_1$) of turbulent kinetic energy per unit volume in a sheet or tube of width $0.01S$ and carrying Reynolds stresses of the order of $0.01U_e^2$ will be of the order $(0.01U_e^2)^{3/2}/0.01S$.

If an approximately equal rate of turbulent kinetic energy production is to be maintained, the rate of strain acting on Reynolds stresses of the order $0.01U_e^2$ must be of the order $10U_e/S$.

Further, he notes that rates of normal (tensile or compressive) strain cannot for long exceed U_e/S without causing velocity changes of greater order than U_e. Thus, a rate of shear strain of order $10U_e/S$ must exist in the sheet or tube, which must therefore be a shear layer with a velocity change of order U_e in a transverse distance of the order of $0.1S$ or a smaller velocity change across an even thinner layer, possibly of the order of $0.01S$. Thus, the original argument is proven; that is, thin sheets or slender tubes of high Reynolds stress exist.

Enhanced Additional Strain Rate Produced by Streamline Curvature

Bradshaw points out that experimental results show that, in turbulent flow, the effects of curvature on the skin friction coefficient are roughly 10 times greater than those predicted for low-speed attached flow, which includes the effects of curvature. He concludes that, evidently, streamline curvature changes the Reynolds stresses of turbulent flow by 10 times as much as it changes viscous stresses. Bradshaw uses linearized formulas, and points out that at present little can be said about higher-order formulas. The particular way that he includes the effects produced by streamline curvature is through inclusion of an enhanced additional strain rate produced by the curvature in addition to the simple shear layer mean flow strain rate $\partial U/\partial y$.

As an example, Bradshaw chooses the case of a thin shear layer in which shear stress is theoretically predicted by eddy viscosity μ formulas of the type

$$\text{Shear stress} = \mu\ (\text{Rate of shear strain})$$

The effect of adding a simple extra rate of strain such as $\partial v/\partial x$ increases the shear stress by the factor

$$1+\frac{\partial v/\partial x}{\partial U/\partial y}$$

Because experimental evidence suggests that the real factor of increase after a prolonged region of streamline curvature is much larger, he modifies the additional strain rate by an order of 10. Thus the modified factor becomes

$$1+10\left(\frac{\partial v/\partial x}{\partial U/\partial y}\right)$$

where $(\partial v/\partial x)/(\partial U/\partial y)$ is assumed to be small.

He indicates also that $\partial v/\partial x$ is only one of a number of extra rates of strain that, when applied to an initially simple shear layer, have produced effects on Reynolds stress that are large compared with the explicit effects of the extra terms that appear in the equations of motion. He notes that it almost seems to be a universal law that if a small extra rate of strain e is added to a simple shear $\partial U/\partial y$, the Reynolds shear stress eventually changes by a factor of the order

$$1\pm 10\frac{e}{\partial U/\partial y}$$

where the number 10 is not to be taken as a universal constant.

Classification of Thin Shear Layers: Turbulence Generation and F-Factor.

Bradshaw notes it is helpful to regard the flows as perturbations of simple shear layers rather than as completely new flows. He defines a simple shear layer as one in which the simple shear $\partial U/\partial y$ is so much larger than any other rate of strain that the direct effect of the extra rates of strain on the turbulence is negligible.

Several other classifications of shear layers including thin shear layer, fairly thin shear layer, and strong distortions are included in Bradshaw's complete characterization and are presented in the following table. He points out that Reynolds stress gradients over thin layers strong enough to effect the mean pressure gradient of a shear layer only occur in what he classifies as a "fairly thin shear layer."

TABLE OF SHEAR LAYER CLASSIFICATIONS

Simple shear layer, $\partial U/\partial y >>^{a} 10e^{b}$	e does not affect turbulence.
Thin shear layer, $\partial U/\partial y >> e$	e does not affect mean flow equations.
Fairly thin shear layer, $\partial U/\partial y > 10e$	Reynolds-stress gradients are significant.
Strong distortion, $\partial U/\partial y < 10e$	Reynolds-stress gradients are locally insignificant.

[a]The sign >> can be read as a factor of inequality of 100.
[b]The term e is any one of the relevant extra strain rates.

Thus he notes that the change in Reynolds stress required to ultimately effect changes in the mean flow motion is what would be predicted by a typical turbulence model if the turbulence generation rate terms had changed by a factor

$$F=1+\alpha\frac{e}{\partial U/\partial y} \qquad \text{(A2)}$$

where α varies from case to case but is always of the order of 10, and e is small. He defines a rate of strain e as being small if $e/(\partial U/\partial y)$ is numerically less than 0.05. If α = 10, F is between 0.5 and 1.5, which are likely to be the largest departures from unity that a linear correction factor like F can be trusted.

Law Of Wall and Its Application To Flat Surface: Simple Shear Layer

The law of the wall as it is normally presented for flow over a flat surface ($Re \to \infty$) is expressed as

$$u^{+}=\frac{1}{k}\ln y^{+}+5 \qquad \text{(A3)}$$

It applies strictly to the case of a simple shear layer in which the local equilibrium approximation is assumed to apply to the turbulent kinetic energy equation in the inner layer, but outside of the viscous sublayer.

The derivation of equation (A3) is based on the assumption that the turbulent kinetic energy production rate equals the inviscid kinetic energy dissipation rate, abbreviated as

$$\text{Production} = -\overline{uv}\left(\frac{\partial U}{\partial y}\right) = \text{Dissipation} = \varepsilon = \frac{\left(-\overline{uv}\right)^{3/2}}{L_1} \tag{A4}$$

where L_1 is the dissipation length parameter and is normally taken as equal to ky; $-\overline{uv}$ may be approximated by the friction velocity squared u_τ^2 for a constant stress layer. Substituting for L_1 in equation (A4) and simplifying results in

$$\frac{\partial U}{\partial y} = \frac{\left(-\overline{uv}\right)^{1/2}}{ky} \tag{A5}$$

Because $-\overline{uv}$ may be approximated by setting $-\overline{uv} = u_\tau^2$ for a constant stress layer, equation (A5) becomes

$$\frac{\partial U}{\partial y} = \frac{u_\tau}{ky} \tag{A6}$$

Letting $y = (y^+\nu)/k$, $U = u^+u_\tau$, and integrating equation (A6) results in equation (A3). Thus equation (A3) strictly applies to the case of flow passing over a flat surface and would not be expected to predict boundary layer velocity profiles for cases in which the surface has a significant degree of curvature, as in the present case of the 20° rearward facing ramp. Specifically, the entrance to the ramp from a flat surface consists of a cylindrical transition section having a radius of curvature of 3.8 cm followed by a 20° (from horizontal) flat surface ramp that leads to a second cylindrical transition section, which directs the flow to the wind tunnel floor.

To consider the case in which the local-equilibrium approximation may not be assumed to apply, Bradshaw presents the following argument.

Application of F-Factor

Bradshaw considers a typical turbulence model for the case of a simple shear layer subjected to a small extra rate of strain. From the turbulent kinetic energy equation,

Production rate = Dissipation rate

or

$$-\overline{uv}\frac{\partial U}{\partial y}\left[1 + a\left(\frac{e}{\dfrac{\partial U}{\partial y}}\right)\right] = -\overline{uv}\frac{\partial U}{\partial y}f^* \equiv \frac{\left(-\overline{uv}\right)^{3/2}}{L_1} \tag{A7}$$

where $f^* = 1 + a[e/(\partial U/\partial y)]$, L_1 is the dissipation length parameter (mixing length), and a is of the order of 1.0.

However, experimental measurements of the effects of extra strain rate imply

$$-\overline{uv}\frac{\partial U}{\partial y}F = \frac{\left(-\overline{uv}\right)^{3/2}}{L_0} \tag{A8}$$

where $F = 1 + \alpha[e/(\partial U/\partial y)]$ and α is of the order of 10.0. Therefore, the ratio of these two equations is

$$\frac{L_1}{L_0} = \frac{F}{f^*} \tag{A9}$$

Because α is an order of magnitude larger than a, equation (A9) may be simplified to

$$\frac{L_1}{L_0} \approx F = 1 + \alpha\left(\frac{e}{\dfrac{\partial U}{\partial y}}\right) \tag{A10}$$

Bradshaw indicates that since a decision has been made to apply the F-factor to the dissipation length parameter, which implies a nonequilibrium region, rather than to the mixing length L_1, it is no longer necessary to make the local-equilibrium approximation. Therefore, the F-factor can be applied to L_0 or to any other length scale appearing in a transport equation calculation method. Thus, the F-factor may be thought of as a measure of the state-of-the-flow variation from local-equilibrium.

Substituting for F in equation (A8) results in

$$-\overline{uv}\frac{\partial U}{\partial y}\left(1 + \frac{\alpha e}{\dfrac{\partial U}{\partial y}}\right) = \frac{\left(-\overline{uv}\right)^{3/2}}{L_0} \tag{A11}$$

where, in the inner layer of a simple shear layer but outside the viscous sublayer, $L_0 = ky$ and $k = 0.41$. Simplifying,

$$\frac{\partial U}{\partial y} + \alpha e = \frac{\left(-\overline{uv}\right)^{1/2}}{ky} \tag{A12}$$

If we assume a constant-stress layer with $-\overline{uv} = u_\tau^2$ and e is independent of y, integrating and simplifying yield

$$\frac{U}{u_\tau} = \frac{1}{k} \ln \frac{u_\tau y}{\nu} + \frac{\alpha e y_0}{u_\tau} - \frac{\alpha e y}{u_\tau} + C \qquad \text{(A13)}$$

where $y_0 = \nu/u_\tau$, and C represents a measure of the change in velocity across the viscous sublayer. Or if it is assumed that e is a function of y, then

$$\frac{U}{u_\tau} = \frac{1}{k} \ln \frac{u_\tau y}{\nu} - \frac{\alpha}{u_\tau} \int_{y_0}^{y} e\,dy + C \qquad \text{(A14)}$$

where $y_0 = \nu/u_\tau$.

When applying equations (A13) or (A14) to a specific case for evaluation, it is necessary to identify a specific strain rate to be substituted for the quantity e. Bradshaw (ref. 15) defines an extra strain rate e as any rate-of-strain component other than a simple shear $\partial U/\partial y$. He describes and justifies several types of extra rates of strain, among which are

(a)	thin curved shear layer	$e = \partial V/\partial x$
(b)	a longitudinal extension	$e = \partial U/\partial x$
	or	
	a normal divergence	$e = \partial V/\partial y$

Appendix B

Brief Discussion of Blackwelder and Swearingen's Study of Oscillation Stage of Bursting Phenomenon

Blackwelder and Swearingen (ref. 27) examined the oscillation stage of the bursting phenomenon for the purpose of suggesting a mechanism by which it occurs. Their proposal considers first the growth rates of the flow disturbances predicted by several stability theories including Michalke's spatially growing disturbances in an inviscid free shear layer (ref. 8), Görtler's secondary instability of a laminar boundary layer (ref. 32), and the linear instability, which predicts the amplification rate of the so-called Tollmien-Schlichting waves. Second, Blackwelder and Swearingen consider the instantaneous changes in the velocity profiles of measured data. These changes revealed that many inflection points existed in the wall region. The existence of these points implies the presence of inviscid instabilities that have very large growth rates. The growth rate of the flow disturbances predicted by both boundary layer flow theories (i.e., Görtler's and the linear instability) revealed that they are at least an order of magnitude less than that predicted by the free shear layer, inflectional profile, instability theory of Michalke.

Reference 27 points out that Görtler's linear theory only describes the initial growth of a small disturbance on a concave wall; it cannot predict the later growth stages and breakdown of the perturbation. Reference 27 continues the discussion by referring to a Bippes' (ref. 29) visualization study of the vortices on a curved plate. This study indicated that after a limited region of linear growth, the flow field developed a strong oscillatory motion before breaking down into turbulence. Because like observations have been made in the wall region of turbulent flow, Swearingen and Blackwelder (ref. 35) performed an experiment similar to that of Bippes to study this phenomenon and to measure the velocity components in more detail. A boundary layer was developed on a concave wall having a large radius of curvature. Rakes of hot wires were aligned to measure instantaneously the spanwise and axial velocity profiles.

Swearingen and Blackwelder made several observations from their experimental results that are important for a greater understanding of these types of flows. The first indicates that the initial Görtler instability produces counter-rotating streamwise vortices with two vortices per spanwise wavelength. They noted that the strength of these coherent vortices is quite small. This observation is based on the assumption of a mean parallel flow $U(y)$ with a disturbance field such that the total velocity is given by

$$\tilde{u} = U + u' \tag{B1}$$

$$\tilde{v} = \frac{v'}{Re} \tag{B2}$$

$$\tilde{w} = \frac{w'}{Re} \tag{B3}$$

Substituting these velocity components in the formation of their corresponding vorticity components indicated that the streamwise vorticity ω_x was smaller than both ω_y and ω_z by Re^{-1}. Therefore, although the flow field is generally described as a laminar boundary layer with embedded growing streamwise vortices, it contains only small amounts of streamwise vorticity. As a consequence, the phase of the coherent structures is a much more important indicator of their presence than is the amplitude of their velocity or vorticity. This result indicates that the detection of coherent structures should not be based on amplitude alone. The reason the ω_x vortices are so effective in controlling the behavior of the flow is that they exist in a region of strong mean shear $\partial U/\partial y$; therefore, a very small ω_x rotation can produce large disturbances across the span. A second observation concerns a unique aspect of the Görtler instability: it creates inflectional velocity profiles in a flow field in which there were none before the disturbance began to grow. These inflectional profiles then open the way to an inviscid instability, which has growth rates an order of magnitude greater than the Görtler instability or the Tollmien-Schlichting waves. Their third observation was that the theoretical wavelength of the amplified oscillation associated with these inflectional velocity profiles was predicted by Michalke's stability theory.

After examining the flow in the Görtler case, Blackwelder and Swearingen consider the wall region of a bounded turbulent shear flow. They note that such a flow is dominated by the bursting process and is composed of a series of events similar to those described for the Görtler problem; namely, there are streamwise vortices, elongated regions of low-speed fluid (low-speed streaks), liftup and oscillation of these streaks, and a rapid disintegration of the coherent motion followed by strong mixing. They note, however, that the role of the streamwise vortices in the turbulent flow is not as clear as it is in the Görtler case. In fact, no generally accepted definition of such vortices is found in the literature. Reference 27 then proceeds to define such a vortex as one consisting of a coherent vortical parcel of fluid such that the instantaneous streamlines in the plane perpendicular to the vortex lines are closed. This

definition emphasizes the coherent aspects of the motion that are associated with its phase and not necessarily with its amplitude. Thus, the definition includes the weak Görtler streamwise vortices, vortex rings, trailing wingtip vortices, etc. but not the mean vortex lines in a two-dimensional shear flow.

Reference 27 indicates that evidence of such vortices in the wall region has been assumed by many authors; however, very little quantitative data exist to support their existence. Most of the data available are visual results such as those of Kline et al. (ref. 33) and Smith and Swartz (ref. 36). The conditionally averaged data of Blackwelder and Eckelmann (ref. 37) and Kim (ref. 38) also support the idea that streamwise vortices exist in the wall region. To investigate these turbulent boundary layer phenomena in more detail, an experiment was performed in which sequential instantaneous velocity profile data were obtained in the spanwise and axial directions. These data revealed the instantaneous changes in the velocity profiles that showed there were many inflection points in both the spanwise and axial velocity profiles in the wall region.

Although these results implied that the oscillation stage of the phenomenon might be explained by Michalke's analysis of spatially growing disturbances in an inviscid shear layer, reference 27 indicates that in addition to the inflectional character of the velocity profiles, several other conditions must be satisfied before Michalke's analysis can be applied. First, the flow should be steady; that is, the changes in time in the mean flow, indicated by the lifetime of the low-speed streaks, must have a much longer time scale than that of the instability. Experiments have indicated that the average lifetime of the low-speed streaks should be from 480 (ν/u_τ^2) to 2580 (ν/u_τ^2). The time scale of the instability is of the order ν/u_τ^2. Second, the site of the instability should be far removed from a solid boundary to insure its inviscid character. Huerre (ref. 39) showed that the characteristics of instability are hardly altered by the presence of a wall, as long as the inflectional region is removed at least 1.2Δ from the wall. The third condition that must be satisfied to apply the stability criteria concerns the dimensionality of the flow field. Reference 27 indicates that no theory is presently available to explain how the three dimensionality of a flow field affects the instability, but the experimental results of Nishioka, Asai, and Iida (ref. 34) suggest that the two-dimensional theory is valid in highly three-dimensional flow fields; however, the amplification rate was reduced below that of the strictly two-dimensional case by about 40 percent. This reduction may be due to the spreading of energy into the third dimension, which is not accounted for in the two-dimensional theory. Even with this reduction, the amplification rate is still very large. More recently, Reed and Haynes (ref. 40) indicated that inviscid stability criteria were successfully used in fully three-dimensional flows along with e^N methods to accurately predict the location of transition. Reference 27 indicates that the first two conditions were satisfied in their experiment and the third was conditionally satisfied, based on the experimental results of reference 34.

Blackwelder and Swearingen (ref. 27) applied Michalke's stability theory to predict the wavelength of the amplified oscillation. They reasoned that if the inflectional profiles were indeed unstable, then one should be able to predict the wavelength of the amplified oscillation. Michalke's results suggest that the wavelength λ, for the most amplified unstable disturbance having a wave number $\alpha_r\Delta$ of 0.40, will be 15.7Δ. Close examination of their data indicates that Δ is roughly $(10\pm5)(\nu/u_\tau)$. Thus, the inflectional profiles should produce disturbances with wavelengths between 75 and $225(\nu/u_\tau)$, where $\alpha_r\Delta$ is 0.40. Reference 27 indicates that data in the literature, including that of reference 33, support this conclusion. Also, they note that one reason there are few data of this type is that the oscillations are occurring within a random background; thus, they are difficult to distinguish from the uncorrelated fluctuations. In addition, because the background provides the initial disturbance for the instability and the energy of the disturbance can grow by a factor of 1000 while traveling one wavelength downstream, an identifiable perturbation can probably only be observed for one wavelength or at most two wavelengths before it is distorted beyond the point of recognition.

In analyzing the bursting phenomenon, Blackwelder and Swearingen (ref. 27) view the production of turbulence as an instantaneous event related to a particular mechanism (i.e., the unstable inflectional velocity profile). Thus, their approach is devoid of Reynolds averaging and provides a different description of the turbulence production process. They point out that in comparison with the Reynolds-averaged equation, where the average turbulent kinetic energy is only fed into the u-fluctuations and then is redistributed by the pressure into the other components, the instantaneous formulation permits the turbulent kinetic energy to be fed directly into the u-, v-, and w-fluctuations. In addition, they indicate that the difference between the two approaches is that the averaged equations do not allow for instantaneous variations in the base flow (i.e., the mean averaged flow) whereas the instantaneous description does. In a mutually complimentary sense, the approach taken by Blackwelder and Swearingen is compatible with the instantaneous capture of events using motion picture flow visualization techniques.

The conclusions of reference 27 are (1) the primary result is that the inflectional velocity profiles are a prevalent feature of the wall region of turbulent flow fields and exist or are present everywhere at the same time; (2) the presence of low-speed streaks in the wall region is one of the clearest indications of the existence of wall eddy structures; (3) the presence of low-speed streaks is a sufficient condition to guarantee that inflectional velocity profiles will be in the spanwise direction because $U(z)$ must vary from high to low values about a zero mean; (4) the instantaneous data also show that there are numerous inflection points in the direction normal to the wall; (5) the locii of infection points are important because they present a mechanism by which turbulence is produced.

References

1. Sovran, G; and Klomp, E.D.: Experimentally Determined Optimum Geometries for Rectilinear Diffusers With Rectangular, Conical or Annular Cross-section. Proceedings of the Symposium on Fluid Mechanics of Internal Flow, Gino Sovran, ed., Elsevier Publishing Co., 1967, pp. 270–319.
2. Johnston, J.P.: Internal Flows. Turbulence, Topics in Applied Physics, vol. 12, P. Bradshaw, ed., Springer-Verlag, 1978, pp. 109–169.
3. Turan, O.F.: The Turbulence Structure in an Eight-degree Conical Diffuser. Instabilities and Turbulence in Engineering Flows. Fluid Mechanics and Its Applications Series, vol. 16, D.E. Ashpis, T.B. Gatski, and R. Hirsh, eds., Kluwer Academic Publishers, 1993, pp. 265–279.
4. Simpson, R.L.; Chew, Y,T.; and Shivaprasad, B.G.: Measurements of a Separating Turbulent Boundary Layer. SQUID–SMU–4–PU, NTIS AD–A095252, Purdue Univ., 1980.
5. Neuburger, D.; and Wygnanski, I.: The Use of a Vibrating Ribbon To Delay Separation on Two-Dimensional Airfoils: Some Preliminary Observations. Proceedings of Workshop II on Unsteady Separated Flow, FJSRL-TR-88–0004, NTIS AD–A202021, 1987.
6. Katz, Y.; Nishri, B.; and Wygnanski, I: The Delay of Turbulent Boundary Layer Separation By Oscillatory Active Control. Phys. Fluids A., vol. 1, no. 2, Feb. 1989, pp. 179–181.
7. McKinzie, D.J., Jr.: Turbulent Boundary Layer Separation Over a Rearward Facing Ramp and Its Control Through Mechanical Excitation. AIAA Paper 91-0253, NASA TM–103702, 1991.
8. Michalke, A.: On Spatially Growing Disturbances in an Inviscid Shear Layer. J. Fluid Mech., vol. 23, Nov. 1965, pp. 521–544.
9. Zaman, K.B.M.Q.; McKinzie, D.J., Jr.; and Rumsey, C.L.: A Natural Low-Frequency Oscillation of the Flow Over an Airfoil Near Stalling Conditions. J. Fluid Mech., vol. 202, May 1989, pp. 403–442.
10. Durbin, P.A.; and McKinzie, D.J., Jr.: Corona Anemometry for Qualitative Measurement of Reversing Surface Flow With Application to Separation Control by External Excitation. Proceedings of the Forum on Unsteady Flow Separation. K.N. Ghia, ed., ASME, 1987, pp. 15–18.
11. Durbin, P.A.; McKinzie, D.J., Jr.; and Durbin, E.J.: An Anemometer for Highly Turbulent or Recirculating Flows. Exp. Fluids, vol.5, no. 3, 1987, pp. 184–188.
12. Chien, J.C.: Numerical Analysis of Turbulent Separated Subsonic Diffuser Flow. Proceedings of the Symposium on Turbulent Shear Flows, vol.1, Pennsylvania State Univ., 1977, pp. 18.19–18.25.
13. Raman, G.; Rice, E.J.; Mankbadi, R.R.: Saturation and the Limit of Jet Mixing Enhancement by Single Frequency Plane Wave Excitation: Experiment and Theory. NASA TM–100882, 1988.
14. Mankbadi, R.R.; Raman, G.; Rice, E.J.: Effects of Core Turbulence on Jet Excitability. AIAA Paper 89–0966, NASA TM–101405, 1989.
15. Bradshaw, P.: Effects of Streamline Curvature on Turbulent Flow. AGARD-AG–169, Aug. 1973.
16. Oster, D.; and Wygnanski, I.: The Forced Mixing Layer Between Parallel Streams. J. Fluid Mech., vol. 123, Oct. 1982, pp. 91–130.
17. Ho, C-M.; and Huang, L-S.: Subharmonics and Vortex Merging in Mixing Layers. J. Fluid Mech., vol. 119, June 1982, pp. 443–473.
18. Kuethe, A.M.; and Schetzer, J.D.: Foundations of Aerodynamics. John Wiley & Sons, Inc., New York, 1959.
19. Zierke, W.C.; and Deutsch, S.: The Measurement of Boundary Layers on a Compressor Blade in Cascade. Volume I: Experimental Technique, Analysis, and Results. NASA CR–185118, 1989.
20. Bradshaw, P., ed.: Turbulence, Topics in Applied Physics, vol. 12; Second corrected and updated ed. Springer-Velag, New York, 1978.
21. Coles, D.: The Law of the Wake in the Turbulent Boundary Layer. J. Fluid Mech., vol. 1, pt. 2, July 1956, pp. 191–226.
22. Hinze, J.O.: Turbulence. Second ed. McGraw-Hill Book Co., New York, 1975.
23. Rotta, J.: Das in Wandnähegültige Geschwindigkeitsgesetz Turbulenter Strömungen. Ingr. Arch., vol. 18, 1950, pp. 277–280.
24. Hama, F.R.: Boundary Layer Characteristics for Smooth and Rough Surfaces. Trans. Soc. Naval Arch. Mar. Engrs., vol. 62, pp. 333–358.
25. Clauser, F.H.: The Turbulent Boundary Layer. Advances in Applied Mechanics, vol. IV, Academic Press, New York, 1956, pp. 1–51.
26. Ersoy, S.: The Viscous Flow Induced Near a Wall by Counter-Rotating Vortex Pairs and Vortex Loops. Ph.d. Dissertation. Lehigh Univ. University Microfilms International, 1985.
27. Blackwelder, R.F.; and Swearingen, J.D.: The Role of Inflectional Velocity Profiles in Wall Bounded Flows. Near-Wall Turbulence, Proceedings of Zorak Zaric Memorial Conference, May 1988, S.J. Kline and N.H. Afran, eds.,Hemisphere Publishing Corp., New York, pp. 268–288.
28. Blackwelder, R.F.: Analogies Between Transitional and Turbulent Boundary Layers. Phys. Fluids, vol. 26, Oct. 1983, pp. 2807–2815.
29. Bippes, H.: Experimentelle Untersuchung des laminar-turbulenten Umschlags an einer parallel angestroemten konkaven Wand (Experimental Study of the Laminar-Turbulent Transition on a Concave Wall in a Parallel Flow). Heidelberg. Akad. Wiss. Math. Naturwiss. K1 Sitzungsber, no. 3, 1972, pp. 103–180.
30. Smith, C.R.; and Schwartz, S.P.: Observation of Streamwise Rotation in the Near-Wall Region of a Turbulent Boundary Layer. Phys. Fluids, vol. 26, no. 3, Mar. 1983, pp. 641–652.
31. Head, M.R.; and Bandyopadhyay, P.: New Aspects of Turbulent Boundary-Layer Structure. J. Fluid Mech., vol. 107, June 1981, pp. 297–338.
32. Görtler, H.: Uber Eine Dreidimensignale Instabilität Laminarer Grenschichten an Konkaven Wänden. Nachr, Ges. Wiss. Goettingen Math. Phys. Klasse, Neue Folge I, 21,1940, I, 2, pp. 1–26.
33. Kline, S.J., et al.: The Structure of Turbulent Boundary Layers. J. Fluid Mech., vol. 30, pt. 4, Dec. 1967, pp. 741–773.
34. Nishioka, M.; Asai, M.; and Iida, S.: An Experimental Investigation of the Secondary Instability—In Plane Poiseuille Flow. Proceedings of the Symposium on Laminar-Turbulent Transition, Springer-Verlag, 1980, pp. 37–46.
35. Swearingen, J.D.; and Blackwelder, R.F.: The Growth and Breakdown of Streamwise Vortices in the Presence of a Wall. J. Fluid Mech., vol. 182, Sept. 1987, pp. 255–290.
36. Smith. C.R.; and Schwartz, S.P.: Observation of Streamwise Rotation in the Near-Wall Region of a Turbulent Boundary Layer. Phys. Fluids, vol.26, Mar. 1983, pp. 641–652.
37. Blackwelder, R.F.; and Eckelmann, H.: Streamwise Vortices Associated With the Bursting Phenomenon. J. Fluid Mech., vol. 94, Oct. 1979, pp. 577–594.
38. Kim, J.: On the Structure of Wall-Bounded Turbulent Flows. Phys. Fluids, vol. 26, Aug. 1983, pp. 2088–2097.
39. Huerre, P.: Finite Amplitude Evolution of Mixing Layers in the Presence of Solid Boundaries. J. Mec. Theor. et Appl. Suppl., Numero Special, 1983, pp. 121–145.
40. Reed, H.L.; and Haynes, T.S.: Observations in Using Linear Stability Theory for 3-D Supersonic Boundary Layers. Instabilities and Turbulence in Engineering Flows. Fluid Mechanics and Its Applications Series, vol. 16, D.E. Ashpis, T.B. Gatski, and F. Hirsch, eds., Kluwer Academic Publishers, 1993, pp. 235–243.

REPORT DOCUMENTATION PAGE

Form Approved
OMB No. 0704-0188

1. AGENCY USE ONLY (*Leave blank*)	2. REPORT DATE	3. REPORT TYPE AND DATES COVERED
	March 1996	Technical Paper

4. TITLE AND SUBTITLE

Delay of Turbulent Boundary Layer Detachment by Mechanical Excitation: Application to Rearward-Facing Ramp

5. FUNDING NUMBERS

WU–505–62–52

6. AUTHOR(S)

Daniel J. McKinzie, Jr.

7. PERFORMING ORGANIZATION NAME(S) AND ADDRESS(ES)

National Aeronautics and Space Administration
Lewis Research Center
Cleveland, Ohio 44135–3191

8. PERFORMING ORGANIZATION REPORT NUMBER

E–9519

9. SPONSORING/MONITORING AGENCY NAME(S) AND ADDRESS(ES)

National Aeronautics and Space Administration
Washington, D.C. 20546–0001

10. SPONSORING/MONITORING AGENCY REPORT NUMBER

NASA TP–3541

11. SUPPLEMENTARY NOTES

Responsible person, John M. Abbott, organization code 2660, (216) 433–3607.

12a. DISTRIBUTION/AVAILABILITY STATEMENT

Unclassified - Unlimited
Subject Categories 1 and 34

This publication is available from the NASA Center for Aerospace Information, (301) 621–0390.

12b. DISTRIBUTION CODE

13. ABSTRACT ***(Maximum 200 words)***

A vane oscillating about a fixed point at the inlet to a two-dimensional 20° rearward-facing ramp proved effective in delaying the detachment of a turbulent boundary layer. Flow-field, surface static pressure, and smoke-wire flow visualization measurements were made. Surface pressure coefficient distributions revealed that two different effects occurred with axial distance along the ramp surface. The surface pressure coefficient varied as a complex function of the vane oscillation frequency and its trailing edge displacement amplitude; that is, it varied as a function of the vane oscillation frequency throughout the entire range of frequencies covered during the test, but it varied over only a limited range of the trailing edge displacement amplitudes covered.The complexity of these findings prompted a detailed investigation, the results of which revealed a combination of phenomena that explain qualitatively how the mechanically generated, periodic, sinusoidal perturbing signal produced by the oscillating vane reacts with the fluid flow to delay the detachment of a turbulent boundary layer experiencing transitory detachment.

14. SUBJECT TERMS	15. NUMBER OF PAGES
Rearward-facing ramp; Separation; Detachment; Diffuser	74
	16. PRICE CODE: A04

17. SECURITY CLASSIFICATION OF REPORT	18. SECURITY CLASSIFICATION OF THIS PAGE	19. SECURITY CLASSIFICATION OF ABSTRACT	20. LIMITATION OF ABSTRACT
Unclassified	Unclassified	Unclassified	